

CONTROLLED PRECIPITATION OF RADIATION BELT
ELECTRONS BY WHISTLER-MODE WAVES

A DISSERTATION
SUBMITTED TO THE DEPARTMENT OF APPLIED PHYSICS
AND THE COMMITTEE ON GRADUATE STUDIES
OF STANFORD UNIVERSITY
IN PARTIAL FULFILLMENT OF THE REQUIREMENTS
FOR THE DEGREE OF
DOCTOR OF PHILOSOPHY

Prajwal Kulkarni

March 2009

© Copyright by Prajwal Kulkarni 2009
All Rights Reserved

I certify that I have read this dissertation and that, in my opinion, it is fully adequate in scope and quality as a dissertation for the degree of Doctor of Philosophy.

(Umran S. Inan) Principal Adviser

I certify that I have read this dissertation and that, in my opinion, it is fully adequate in scope and quality as a dissertation for the degree of Doctor of Philosophy.

(Timothy F. Bell)

I certify that I have read this dissertation and that, in my opinion, it is fully adequate in scope and quality as a dissertation for the degree of Doctor of Philosophy.

(Alexander L. Fetter)

Approved for the University Committee on Graduate Studies.

This thesis is dedicated to my mother.

Abstract

This dissertation presents results and analysis regarding the use of anthropogenic ground-based and space-based Very Low Frequency (VLF) transmitters to precipitate energetic electrons in the inner radiation belt. While existing ground-based VLF transmitters already precipitate energetic electrons, they do so inadvertently. In this work, we consider sources designed specifically for the purpose of precipitating >100 keV electrons. This concept is termed controlled precipitation. We focus on this energy range because these electrons are most damaging from a so-called space weather perspective.

We initially consider the distribution of whistler-mode wave energy from space-based sources distributed in L -shell and geomagnetic latitude. We also incorporate the effects of VLF antenna radiation immersed in a magnetoplasma. Our results demonstrate that a space-based source, by varying the frequency of the injected waves, can target L -shells both higher and lower than the source site, with wave frequencies below (above) the local lower hybrid resonance frequency moving to higher (lower) L -shells. We show that only three sources placed at various locations in the inner magnetosphere are required to project wave power over the range $1.4 \leq L \leq 2.7$, which comprises the bulk of the inner radiation belt. We also calculate the energetic electron precipitation that would be induced by waves injected by such sources. The waves injected by space-based sources propagate with highly oblique wave normal angles close to the local resonance cone. In contrast with previous analysis, we show that these waves do induce substantial >1 MeV electron precipitation. Compared to a single-pass interaction, highly oblique magnetospherically reflecting whistler-mode waves precipitate up to 16 times more 100 keV to 5 MeV electrons. Waves injected

at initial wave normal angles closer to the magnetic field, e.g., 45° , in fact precipitate fewer >1 MeV electrons than waves injected close to the resonance cone.

We also investigate the tradeoffs among source location, operating frequency and radiated power for ground-based VLF sources designed to precipitate energetic electrons in the inner radiation belts. We determine energetic electron precipitation signatures induced by five existing ground-based VLF sources as well as five different hypothetical transmitters distributed broadly in geomagnetic latitude with a wide range of operating frequencies. We show that source location affects induced precipitation more strongly than operating frequency or radiated power. Sources located at 35° to 45° induce the most >100 keV precipitation for the 10 to 40 kHz waves typical of ground-based VLF sources, while locations below $\lambda \simeq 15^\circ$ or above $\lambda \simeq 55^\circ$ are least effective at precipitating energetic electrons. In all cases, induced precipitation increases as the operating frequency decreases, with 10 kHz waves from a source at $\lambda \simeq 35^\circ$ the most effective at precipitating >100 keV electrons. Precipitation signatures produced by five existing ground-based VLF transmitters are also simulated: the NAA, NLK, NAU, NPM, and NWC VLF transmitters. Among these, the NWC transmitter located at a geomagnetic latitude of 31.7° in western Australia induces the strongest >100 keV electron precipitation signature, followed by the NPM, NAU, NAA and NLK transmitters.

Acknowledgements

There are many people who helped make this work possible. First and foremost I thank my advisor, Professor Umran S. Inan, for his unflinching support throughout my graduate career. It has been very comforting to know that Umran always looks out for his students' welfare. Mostly because he consistently accommodated all of my interests, both research and extracurricular, graduate school has been the most rewarding years of my life. Furthermore, his compassion at key moments in my first few years was invaluable. In my first year at Stanford, I met with a very serious injury that could have derailed my Ph.D. Umran's understanding cannot be overstated, and I am eternally grateful.

I also thank my secondary advisor, Dr. Timothy F. Bell. Tim has always patiently and carefully explained all research questions I had. His breadth of knowledge, mathematical prowess and intuition continue to amaze me.

Professor Alexander Fetter deserves appreciation for serving as my advisor in the Department of Applied Physics as well as being the third reader of this dissertation. I am also very grateful to Professors Mark Cappelli and Steve Harris for agreeing to be on my dissertation defense committee at such short notice. I also would like to thank STARLab faculty who have helped me over the years. I have benefited from many fruitful conversations with Professor D. L. Carpenter and Dr. M. Walt.

I am very fortunate to have been a member of both the VLF Group and the Department of Applied Physics, both among the friendliest and most efficient at Stanford. Without a doubt, the tireless, wonderful administrators deserve much credit: Paula Perron and Claire Nicholas in the Department of Applied Physics, and Shaolan Min and Helen Niu in the VLF Group.

I will truly cherish my time in the VLF Research Group. While all members both past and present deserve thanks, a few must be highlighted. Jacob Bortnik's endless patience throughout my career has been inspiring. If I ever have to be a mentor, I know that I look up to Jacob as a role model. Morris Cohen, Andrew Gibby, and Marek Gołkowski were always there to help me understand plasma physics as well as geopolitics. I will miss those discussions. Dan Golden has been an invaluable friend and labmate.

I also thank all my friends: the incoming Applied Physics and Physics class of 2003, the Stanford University Triathlon Team, folks from Studio 5 and 6, my fellow idealists in the Science Bus, and everyone else I became close to over the past six years. You all know who you are and how much you mean to me.

Lastly, I would like to recognize the three most important people in my life. More than he will ever realize, my father has influenced my thinking and helped make me who I am today. My brother loves me unconditionally and always inspires me to improve. Most importantly, more than anyone else, I would like to thank my mother. She is the first best friend I ever had.

Contents

Abstract	vi
Acknowledgements	viii
1 Introduction	1
1.1 Scientific Background	2
1.1.1 The Magnetosphere	2
1.1.2 The Van Allen Radiation Belts	3
1.1.3 Anthropogenic VLF Sources	8
1.2 Review of Past Work	9
1.3 Thesis Organization	14
1.4 Scientific Contributions	15
2 Theoretical Background	16
2.1 Numerical Raytracing	17
2.2 Landau Damping	21
2.3 Wave-Particle Interaction	23
2.4 Antenna Radiation and Ionospheric Absorption	26
3 Energy Distribution	29
3.1 Introduction	29
3.2 Magnetospheric Cavity Enhancement Factor	30
3.3 Simulation Results	32
3.4 <i>L</i> -shell Settling and Wave Lifetimes	35

3.4.1	Injections at the Geomagnetic Equator	36
3.4.2	Off-Equatorial Injections	43
3.4.3	Comparison and Analysis	45
3.5	Effects of Antenna Radiation Efficiency	49
4	Space-Based Sources	53
4.1	Introduction	53
4.2	Simulation Procedure	54
4.3	Relevant Physics	56
4.3.1	MR Whistler-Mode Waves	56
4.3.2	Wave-particle Interaction	58
4.4	Simulation Results and Analysis	60
5	Ground-Based Sources	74
5.1	Introduction	74
5.2	Model Description and Simulation Procedure	75
5.3	Simulation Results and Analysis	80
5.3.1	Existing VLF Transmitters	86
5.3.2	Sensitivity to Assumptions	88
6	Summary	92
6.1	Summary	92
6.2	Suggestions for Future Work	94
6.2.1	Ionospheric Absorption	95
6.2.2	Warm Plasma Effects	96
A	Wave-Normal Angle Restriction	98

List of Tables

3.1	Local Lower Hybrid Resonance Frequency	50
4.1	Cavity Gain Factor	61
4.2	Cavity Gain Factor versus ψ	70
5.1	Existing Ground-Based VLF Transmitters	76

List of Figures

1.1	The Earth's Magnetosphere	4
1.2	The Inner Magnetosphere	5
1.3	The Van Allen Radiation Belts	6
1.4	The Slot Region	7
1.5	Trapped Electron Motion	8
1.6	Anthropogenic VLF Sources	10
2.1	Sample Raypaths	18
2.2	Equatorial Electron Density	20
2.3	One-Dimensional Maxwellian	21
2.4	Raypath and Landau Damping	22
3.1	Cavity Enhancement Factor	33
3.2	Positive Wave Normal Angles	34
3.3	L -shell Settling	36
3.4	Injection from $L=2$, $\lambda=0^\circ$	38
3.5	Cavity Enhancement Factor versus ψ	39
3.6	Frequencies Below and Above the f_{LHR}	40
3.7	Integrated Cavity Enhancement Factor	41
3.8	Cavity Enhancement Factor at $L=1.5$	42
3.9	Off-equatorial Injections	44
3.10	Cavity Enhancement Factor at $L=2$	45
3.11	Magnetospheric Illumination	48
3.12	Effect of Antenna Radiation	52

4.1	ψ versus ψ_{res}	57
4.2	Electron Resonant Energy	58
4.3	Differential Number Flux: AE8 Distribution	63
4.4	Differential Number Flux: Constant Distribution	65
4.5	Illumination Spectra: $L=1.5$	66
4.6	Illumination Spectra: $L=2.0$	67
4.7	Illumination Spectra: $L=2.5$	67
4.8	Raypath, Damping and Latitude vs. Group Time	68
4.9	Illumination Spectra versus ψ	69
4.10	Rays Injected Outside the Meridional Plane	71
4.11	Rays Injected Outside the Meridional Plane	72
5.1	Raypaths and Resonant Energy	79
5.2	Raypaths for 20 kHz and 40 kHz Waves	81
5.3	Power Flux and Wave Normal Angle Distribution	82
5.4	Hypothetical Sources: 100 keV Flux	84
5.5	Hypothetical Sources: 1 MeV Flux	84
5.6	Hypothetical Sources: Flux vs. Radiated Power	86
5.7	Flux Induced by Existing Ground-Based VLF Sources	89
5.8	Sensitivity to Model Assumptions	91

Chapter 1

Introduction

In May 1998, operators lost communication with the Galaxy 4 satellite, and forty-five million customers in North America were without pager service, including medical professionals and emergency workers [Baker, 2000]. Baker [2000] has argued that enhanced fluxes of energetic electrons may have exacerbated this situation, and contributed to compromised operation on the Intelsat K, Anik E-1 and Telstar 401 spacecraft. It may be possible to address this problem by using anthropogenic sources of Very Low Frequency (VLF) whistler-mode waves to inject VLF energy into the inner magnetosphere which can scatter energetic electrons in pitch-angle and precipitate them out of their trapped orbits. This dissertation aims to quantitatively investigate the effect on energetic electrons in the Van Allen Radiation Belts of waves injected by both ground-based and space-based VLF sources. Controlled precipitation refers to the notion that human-made VLF sources can be used to modify the pitch-angles and populations of radiation belt electrons.

To investigate this concept, we utilize numerical raytracing to determine raypaths of waves that would be injected from both ground and space-based VLF sources. This calculation is coupled with an estimate of the attenuation of the waves along the raypaths, and a calculation of the pitch-angle scattering for resonant energetic electrons. We simulate a broad range of underlying parameters and analyze the results to highlight the crucial parameters and tradeoffs. Specifically for ground-based

VLF sources, we are interested in the relative importance of source location, operating frequency and radiated power in inducing energetic electron precipitation. For space-based VLF sources, it is necessary to determine how many sources are needed to project whistler-mode wave energy through selected regions of the inner magnetosphere. The distribution of whistler-mode wave energy is impacted by realistic models of VLF wave radiation for dipole antennas in a magnetoplasma, which we also include in our analysis. We calculate the resultant electron precipitation and examine in great detail the sensitivity of the induced precipitation on the orientation of the wave \mathbf{k} -vector. This chapter presents the relevant background and discusses the contributions of our work.

1.1 Scientific Background

The major processes described in this work, including VLF wave propagation and spreading in the inhomogeneous inner magnetosphere, Landau damping, and cyclotron resonance wave-particle interactions, take place in the near-Earth space environment. We now examine the physics of this region, focusing on the magnetosphere and the Van Allen radiation belts, and describe how anthropogenic sources can induce the loss of energetic electrons from the radiation belts.

1.1.1 The Magnetosphere

The plasma ejected outward from the Sun's atmosphere is known as the solar wind. A portion of the solar wind travels toward the Earth and interacts with the Earth's magnetic field, producing the general shape of the magnetosphere shown in Figure 1.1 [Walt, 1994, p. 2]. On the day side, the solar wind compresses the Earth's magnetic field at ~ 10 Earth radii (R_E) and results in a bow shock wave ($1R_E \simeq 6370$ km). On the night side, the dipole field-solar wind interaction results in a long tail that stretches to $\sim 60R_E$. Within the magnetosphere, wave and particle physics are largely governed by the Earth's magnetic field, giving the region its name. This work focuses on the section of the magnetosphere where the Earth's magnetic field can be

accurately modeled as a dipole with the dipole axis tilted and offset with respect to the Earth's rotation axis. This region, known as the inner magnetosphere, extends up to $\sim 6-7R_E$. Figure 1.2 shows the magnetosphere closer to the Earth, where the region shaded in dark gray represents the dipole magnetic field of the inner magnetosphere.

The inner magnetospheric plasma is fully ionized and of sufficiently low density that the medium can be considered collisionless. The bulk of the magnetospheric plasma is composed of particles that have a plasma temperature of ≤ 1 eV, and densities of $10 - 10^4$ el-cm $^{-3}$ [Carpenter, 1963]. The density of this so-called 'cold plasma' drops approximately two orders of magnitude at a boundary termed the 'plasmopause' [Carpenter, 1963]. Depending on geomagnetic activity, the plasmopause can be located anywhere from $3-7R_E$. Though the location of the plasmopause can influence the propagation of waves and the distribution of wave energy, the VLF whistler-mode waves injected by anthropogenic sources generally remain confined to magnetospheric regions at a radial distance of less than $3R_E$.

Accordingly, the major conclusions presented here are largely unaffected when we change the input parameters to reflect active, rather than quiet, geomagnetic conditions (see Chapter 5). Though there are almost many satellites located in the outer radiation belts, the energetic electron lifetimes are generally shorter in that region because geomagnetic storms often distort the Earth's magnetic field at those locations. When this occurs, particles may become untrapped due to their adiabatic invariant being violated (see Chapter 2). We now discuss the enhanced fluxes of energetic electrons that comprise the Van Allen radiation belts.

1.1.2 The Van Allen Radiation Belts

In addition to the cold plasma, there are two broad regions of energetic electrons trapped in the Earth's geomagnetic field, known as the Van Allen radiation belts, or more simply the radiation belts. These electrons are of very low density ($\ll 1$ el-cm $^{-3}$), and have energies from ~ 1 keV–5 MeV. Figure 1.3 shows a schematic picture of the Van Allen belts. Note that there is an inner radiation belt, from $\sim 1-2R_E$, and an outer radiation belt, from $\sim 3-5R_E$. In between these two belts is a region of depleted

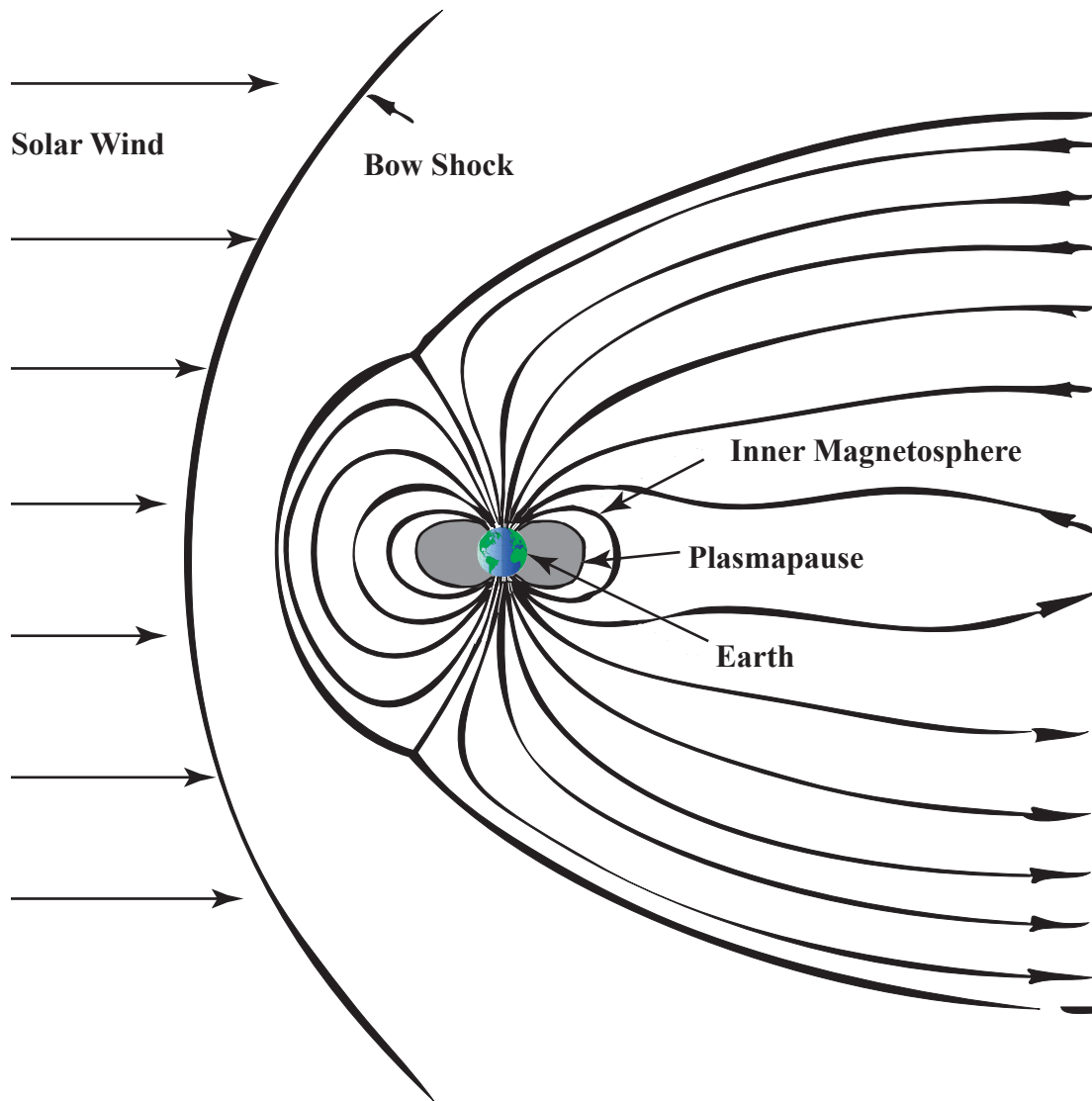


Figure 1.1: A general picture of the magnetosphere. Adapted from [Inan, 1977].

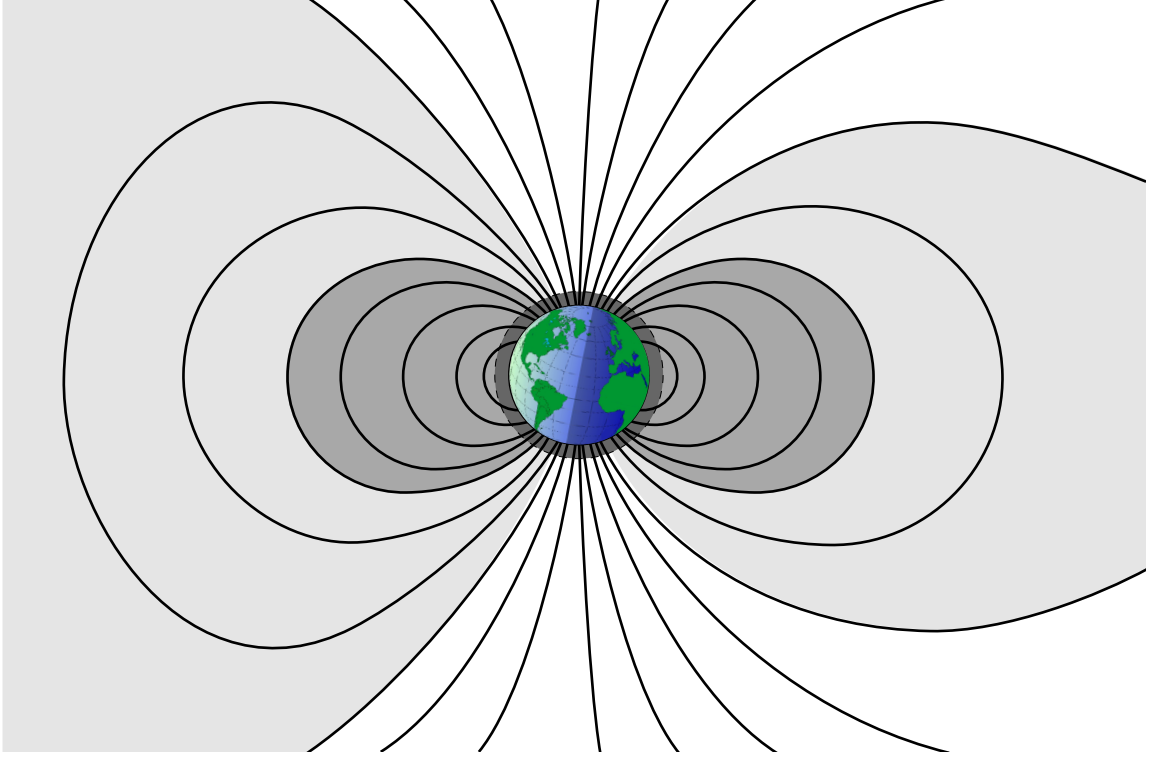


Figure 1.2: The black lines represent the geomagnetic field lines, and the dark (light) gray refers to the cold plasma inside (outside) the plasmapause. Adapted from [Inan, 1977]

energetic electron density, known as the slot region [Walt, 1994, p. 80]. Figure 1.4 shows flux versus L -shell above various energy thresholds. Note that from $L \sim 2-3$, there is a pronounced decrease in electron flux. For the purpose of this study, we focus primarily on the electrons that are >100 keV in energy because these electrons are most dangerous to space assets [Baker, 2000].

The trapped energetic electrons that comprise the radiation belts execute three types of motion. First, they gyrate around the magnetic field with an angular frequency known as the cyclotron frequency or gyrofrequency. Additionally, these electrons also move along the magnetic field line, bouncing back and forth between the hemispheres. The electron reverses its direction at points known as the mirror points. Finally, energetic electrons also drift around the Earth from west to east. The magnitude of the cyclotron frequency is directly proportional to the magnitude of the

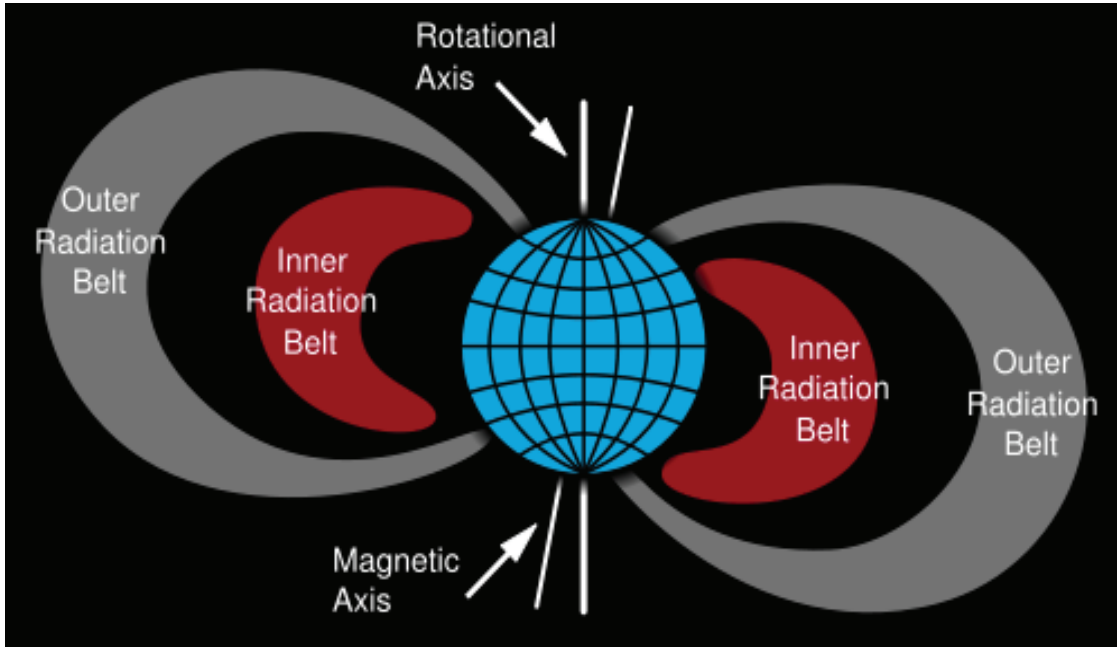


Figure 1.3: Note the existence of both an inner and an outer radiation belt. This work focuses on wave-particle interactions in the inner belt.

Earth's geomagnetic dipole field, and is therefore a function of both radial distance and geomagnetic latitude. It is approximately 880 kHz at the equator at the Earth's surface. Bounce times depend on the electron energy and L -shell, but are typically on the order of 0.2 to 1 second. The drift period also depends on energy and location, but timescales range from tens of minutes to a few hours. Figure 1.5 shows the three types of motion of a trapped energetic electron. These three types of electron motion—gyration, bounce motion, and longitudinal drift—are associated with the adiabatic invariants of the particle. In principle, the electron can remain trapped in its adiabatic motion indefinitely [Walt, 1994, p. 42].

However, cyclotron-resonance interactions with VLF whistler-mode waves can perturb the trapped motion of the electron, causing the mirror point to be lowered to denser regions of the Earth's atmosphere. Within these denser regions, collisions with atmospheric constituents effectively remove the electron from its trapped motion, and

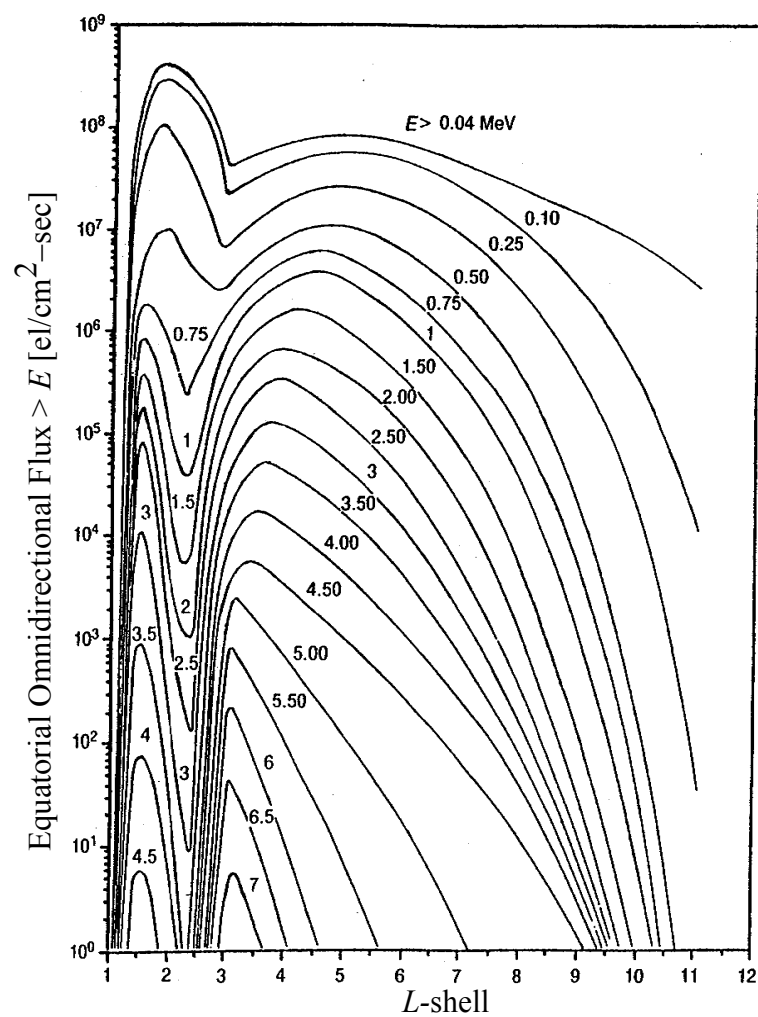


Figure 1.4: Equatorial values of the integral, omnidirectional electron flux above various energy thresholds. Based on data from the National Space Science Data Center [Walt, 1994, p. 80].

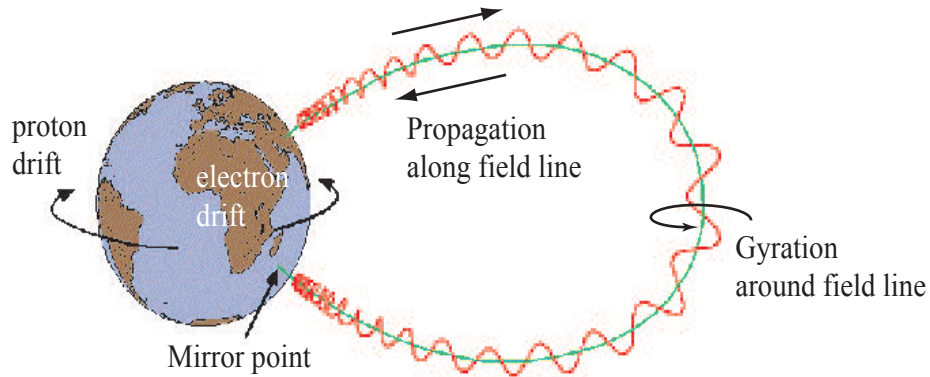


Figure 1.5: Motion of an energetic electron trapped on a magnetic field line. The electron gyrates around and moves along the field line. It reverses direction at the mirror point. Note that electrons drift from west to east.

the electron is said to have been precipitated. At ~ 100 km altitude, the atmosphere is sufficiently dense such that loss-cone electrons that propagate to that point will undergo numerous collisions. The trapped adiabatic motion of the electron (see Chapter 2 for more detail) is then disturbed, the electron deposits its energy and is said to be precipitated.

It is through these processes—resonant interactions with whistler-mode waves—that ground-based and space-based VLF sources may be used to precipitate radiation belt electrons. In Chapter 2, we describe in greater detail the physics of whistler-mode wave propagation and cyclotron-resonance interaction.

1.1.3 Anthropogenic VLF Sources

To precipitate energetic electrons from the radiation belts, anthropogenic sources of VLF waves can be used to inject whistler-mode wave energy into the inner magnetosphere. To do so, we can use a VLF transmitter on the Earth’s surface or one placed on a satellite orbiting in the near-Earth space environment. Figure 1.6 shows how waves from such sources populate the magnetosphere. In the left panel, the red dot denotes the location of a ground-based VLF transmitter. In fact, such sources already

exist at several locations around the world. These existing VLF transmitters radiate electromagnetic wave energy continuously for the purpose of naval communications. The wave energy mostly propagates within the so-called Earth-ionosphere waveguide, where the base of the ionosphere is shown in dashed green lines in Figure 1.6. Some of the wave energy inevitably leaks into space and propagates in the near-Earth space environment. These waves (shown in red arrows in Figure 1.6a) propagate in the plasmasphere, resonantly interact with and precipitate energetic electrons. In fact, anthropogenic sources and specifically ground-based VLF transmitters are already an important driver of loss processes in the inner radiation belts [Abel and Thorne, 1998a,b]. Chapter 5 discusses in more detail the precipitation of energetic electrons induced by ground-based VLF sources.

Figure 1.6b shows how a space-based VLF source would precipitate energetic electrons in the inner radiation belt. The yellow square refers to the location of the source, and the dashed green lines represent geomagnetic field lines. A space-based VLF source thus situated would radiate whistler-mode energy directly into the radiation belts. Typical raypaths of waves that would be injected by such a source are shown in red. Note that the wave energy reflects multiple times along the raypath, a process known as a magnetospheric reflection [Edgar, 1972] that is discussed in greater detail in the following three chapters.

For the ground-based VLF sources considered here, the injected waves do not propagate beyond $\sim 3R_E$ (see Chapter 5) and are almost always contained within the plasmasphere. Additionally, we only consider space-based sources at $L \leq 2.5$. For these reasons, this study focuses on the inner radiation belt, rather than the outer radiation belt.

1.2 Review of Past Work

A complete description of all the work on whistler-mode wave propagation and wave-particle interactions in the inner magnetosphere is outside the scope of this study. We choose instead to highlight the work that this study directly builds upon and depends on, and note briefly how our work advances previous results. The specific

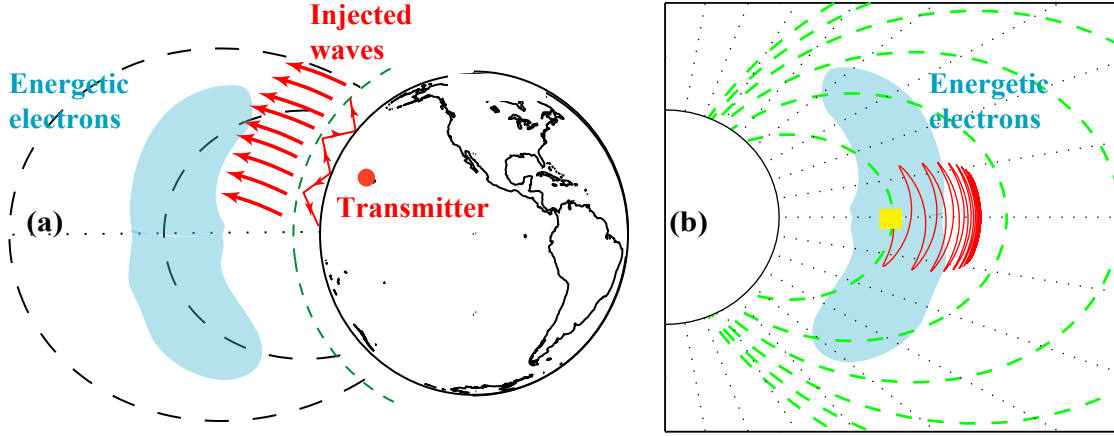


Figure 1.6: (a) The red dot denotes the location of a ground-based VLF source, and the dashed green line is the base of the ionosphere. VLF wave energy escapes into space and interacts with radiation belt electrons. (b) The yellow square is the location of a space-based VLF source that emits whistler-mode wave energy (shown in red) directly into the radiation belts.

details, simulation results and major conclusions are presented in Chapters 3, 4, and 5.

Three papers in the 1960's first broached the idea of using anthropogenic VLF sources to impact energetic electrons in the inner radiation belt. *Helliwell and Bell* [1960] suggested that a ground-based VLF transmitter radiating a decreasing frequency tone could make use of the gyroresonance phenomenon to accelerate electrons from 1 keV up to 1 MeV in energy. That is, resonance interactions with VLF whistler-mode waves would result in energy exchange with the particles, resulting in acceleration of the electrons. The authors noted that transmitters need to operate at power levels over 100 kW to accomplish this goal. *Bell* [1964] also noted that the gyroresonance phenomena leads to energy exchange, but instead used a wave frequency that increases with time leading to deceleration of the electrons (and associated amplification of the wave), thereby causing precipitation of electrons. *Dungey* [1963] also argued that the resonance interaction with whistler-mode waves can induce the loss

of energetic electrons from the Van Allen belts. *Dungey* [1963] emphasized that the interaction would change the pitch-angle of the energetic electron, causing the mirror point to enter the Earth’s dense upper atmosphere. Other research has explored the amplification of whistler-mode waves by the gyroresonance interaction (see [*Gibby*, 2008; *Gołkowski et al.*, 2008] and references therein).

The mid-1960’s witnessed the first attempts at studying the resonance wave-particle interaction using ground-based anthropogenic VLF sources. While focusing on wave amplification (leading to de-energization of energetic electrons), the transmitter established in Byrd Station, Antarctica attempted, but was unable, to successfully generate VLF waves to inject into the magnetosphere [*Helliwell and Katsufurakis*, 1974]. From 1971 to 1988, Stanford University operated a more long term magnetospheric wave injection experiment at Siple Station, Antarctica. This experiment successfully produced many observations of wave amplification, and the results maintain their importance to present experimental and theoretical investigations in space physics [*Gibby*, 2008].

Constructing VLF transmitters on the Earth’s surface is often prohibitively difficult because the wavelengths of interest are tens of kilometers, requiring extremely long antennas. The Siple Station VLF transmitter was able to take advantage of the 2 km thick ice sheet that elevated the horizontal antenna above the conducting plane a significant fraction of a wavelength. However, most locations on Earth do not offer this benefit. To overcome this difficulty, scientists in the 1970’s devised a new method to generate ELF/VLF wave frequencies by utilizing naturally occurring ionospheric currents [*Getmantsev et al.*, 1974; *Stubbe et al.*, 1977, 1982]. High Frequency (HF) waves between 3 and 30 MHz can be easily generated on the ground due to shorter wavelengths, and are used to change the conductivity of the ionosphere at altitudes of 60–100 km. By modulating the HF signal, the natural currents in the ionosphere are then transformed into a giant radiating antenna in the sky. Such facilities have been used to study wave amplification in the inner magnetosphere [*Gołkowski et al.*, 2008].

In addition to undergoing amplification, waves injected by man-made VLF sources can also induce precipitation through the cyclotron-resonance interaction that lowers

the electron's mirror altitude into the denser regions of the atmosphere [Inan *et al.*, 1982]. Several authors have suggested that this process plays a dominant role in the loss of energetic electrons from the radiation belts [Kennel and Petschek, 1966; Lyons *et al.*, 1972]. Simulation and theoretical analysis also suggest that such ground-based VLF sources may indeed induce substantial energetic electron precipitation. Inan *et al.* [1984] used a test-particle simulation to determine the spatial distribution of electron precipitation caused by existing ground-based VLF transmitters. While exclusively considering only propagation along the magnetic field lines (i.e., within ducts of enhanced ionization) this study concluded that transmitter geographic location and operating frequency strongly affect precipitation flux levels and spatial extent. Abel and Thorne [1998a,b] calculated electron lifetimes driven by wave-particle interactions using bounce-averaged pitch-angle diffusion coefficients and concluded that VLF transmitters have a substantial effect on energetic (>100 keV) electron lifetimes at $L < 2.6$. These results imply that such sources may be used specifically to target >100 keV electrons, the energy range of interest.

The present study builds upon the results presented in Inan *et al.* [1984] by removing the restriction of ducted propagation, and instead uses the Stanford 2D VLF Raytracing program [Inan and Bell, 1977] to determine regions of magnetospheric illumination using raytracing in a smooth magnetosphere. We determine the induced energetic electron precipitation for numerous hypothetical ground-based VLF sources in addition to the existing sources considered by Inan *et al.* [1984]. Based on these simulation results we are able to make, for the first time, quantitative conclusions regarding the operating frequencies and source locations that most effectively precipitate >100 keV electrons.

Inan *et al.* [2003] were the first to suggest that space-based sources may be particularly effective at precipitating energetic electrons, especially those that are >1 MeV in energy. By power scaling the results from Abel and Thorne [1998a], Inan *et al.* [2003] indicated that a space-borne transmitter at operating frequencies of 1–10 kHz can drive diffusion rates that, compared to signals from ground-based VLF transmitters, may be higher by up to a factor of ~ 30 . The high diffusion rates can be further leveraged because whistler-mode waves at the frequencies considered often

undergo multiple magnetospheric reflections [Edgar, 1972]. A single injected wave packet may endure for several seconds and can be much more efficiently stored in the magnetospheric cavity as compared to the higher wave frequencies from ground-based transmitters that typically make only a single traverse of the magnetosphere. In drawing their conclusions, *Inan et al.* [2003] concentrated on waves injected at a single point at $L=2$ at the magnetic equator and considered only a small number of frequencies and injection wave normal-angles.

This study expands on the results presented in *Inan et al.* [2003] by considering a broad range of source locations, operating frequencies and initial wave normal angles. We have also accounted for path-integrated Landau damping and utilized a realistic model [Wang and Bell, 1970] of dipole antenna radiation in a magnetosplasma. We examine the effects of sources at both equatorial and off-equatorial locations, as well as wave frequencies below and above the local lower hybrid resonance frequency. Based on these results, we determine the precipitation that would be induced by space-based sources distributed in L -shell and geomagnetic latitude, noting that the efficiency of pitch-angle scattering is partly affected by the direction of the wave \mathbf{k} -vector. The magnetospherically reflecting whistler-mode waves injected from a space-based source propagate with highly oblique wave normal angles. While previous work has concluded that such waves may be ineffective at precipitating >1 MeV electrons [Inan and Bell, 1991; Albert, 1999], they have done so by excluding the effects of wave propagation. Our work, on the other hand, includes a more detailed analysis that incorporates numerical raytracing.

To quantitatively evaluate the energetic electron precipitation induced by both ground and space-based anthropogenic VLF sources, we draw upon past work that has investigated the interactions between naturally occurring whistler-mode waves (especially those injected by lightning discharges) and energetic electrons. In fact, the physics of the wave-particle interaction is identical whether the whistler-mode wave is injected from a lightning strike or a VLF transmitter. The basic gyro-averaged equations of motion for resonance interactions between obliquely propagating whistler-mode waves and energetic electrons were developed by Bell [1984]. We use the method of Bortnik et al. [2006a] to integrate these equations to calculate

the pitch-angle changes induced by the VLF transmitter signals considered here.

In the context of the *Bortnik et al.* [2006a] model, extensive raytracing, Landau damping and interpolation are combined to produce a wave map that contains the relevant parameters (refractive index, wave power, wave normal angle) at one-degree intervals along each field line from -40 to 40 degrees in geomagnetic latitude. At each one-degree interval range, these wave characteristics are used to compute the root-mean-square (i.e., averaged over Larmor phase) pitch-angle change for loss-cone electrons with parallel velocities in a narrow range around the resonant parallel velocity at that location. The interactions are assumed to be linear (i.e., wave intensity is not large enough to phase-trap the electrons) and independent at different latitudes. To determine the total flux of precipitated particles, the calculated pitch-angle changes are applied to near loss-cone electrons (i.e., to electrons immediately above the loss cone), recognizing that their scattering is similar to that which was calculated for the electrons at edge of the loss cone. While the methodology described in *Bortnik et al.* [2006a] was applied to a transient lightning stroke, we have made appropriate modifications to allow us to model a one-half second long VLF pulse at a given transmitter frequency. Chapter 2 describes these models in greater detail and also provides additional insight into the wave-particle interaction.

1.3 Thesis Organization

The present work is organized into 6 chapters.

Chapter 1, the present chapter, highlights the relevant background and motivation for this work.

Chapter 2 describes in great detail the theoretical models that underlie this work. Specifically, we discuss whistler-mode wave propagation in the inner magnetosphere, Landau damping, and the cyclotron-resonance wave-particle interaction.

Chapter 3 presents simulation results and analysis regarding the number of space-based VLF sources needed to fill the inner magnetosphere with whistler-mode wave energy. This chapter also analyzes the effect of incorporating realistic models of antenna radiation in a magnetoplasma.

Chapter 4 advances the initial analysis shown in Chapter 3 by calculating the precipitation that would be induced by those sources. Chapter 4 also carefully determines how the orientation of the wave \mathbf{k} -vector impacts the effectiveness of the wave-particle interaction.

Chapter 5 transitions from space-based to ground-based VLF sources, and displays simulation results for numerous hypothetical and existing VLF transmitters. Based on this extensive numerical modeling, Chapter 5 offers quantitative conclusions on the relative importance of source location, operating frequency and radiated power for the purpose of precipitating energetic electron.

Chapter 6 summarizes and suggests future work on this topic.

1.4 Scientific Contributions

This work makes several scientific contributions described below:

1. Identified the number of sources, geospace locations and operating frequencies necessary for space-based transmitters to fill the inner magnetosphere with whistler-mode wave energy [*Kulkarni et al.*, 2006]
2. Calculated the energetic electron precipitation signatures that would be induced by space-based sources distributed in L -shell and geomagnetic latitude [*Kulkarni et al.*, 2008a]
3. Determined that magnetospherically reflecting whistler-mode waves propagating with wave normal angles close to the resonance cone do indeed induce significant levels of energetic electron precipitation [*Kulkarni et al.*, 2008a]
4. Calculated the relative energetic electron precipitation induced by existing ground-based VLF transmitters [*Kulkarni et al.*, 2008b]
5. Modeled hypothetical ground-based VLF sources to determine the importance of source location over operating frequency and radiated power for the purpose of energetic electron precipitation [*Kulkarni et al.*, 2008b]

Chapter 2

Theoretical Background

The simulation results discussed in this study and presented in Chapters 3, 4, and 5 are based on a number of assumptions and were obtained using a number of different computational tools. Here we present these details in full, carefully describing the underlying models used. The precipitation induced by ground and space-based sources both utilize three computational tools: numerical raytracing, path-integrated Landau damping, and a test-particle based calculation of the pitch-angle change and resultant precipitated flux from resonance interactions between energetic electrons and VLF whistler-mode waves.

Additionally, in calculating precipitation induced by ground-based VLF sources, we incorporate assumptions regarding the Poynting flux radiated by such sources, and the attenuation due to collisional absorption in the D-region (from $\sim 60\text{--}90$ km altitude) as the waves propagate through the ionosphere. For space-based sources, we also account for the radiation characteristics of an antenna immersed in the magnetoplasma. We proceed with descriptions of the three models common to both types of VLF sources, and then individually treat the unique features of precipitation induced by each.

2.1 Numerical Raytracing

To describe the propagation of whistler-mode waves in near-Earth space, it is important to account for the fact that the ambient magnetic field and particle density have different values at different locations in space. While the presence of spatial gradients in plasma density and magnetic field renders it computationally difficult to obtain wave trajectory solutions under arbitrary and general conditions, significant simplifying assumptions can be made under certain conditions. If the properties of the medium vary slowly within one wavelength (up to a few kilometers), then we can adopt the geometric optics approximation, where electromagnetic waves are treated as particles [Hecht, 2002, p. 36]. These particles are called rays, and the trajectories they follow in space are termed raypaths. Geometric optics assumes that the properties of the medium are locally constant within a given “slab”, but change slowly as the ray propagates to another slab. More generally, we can conceptualize this process of ray propagation in an inhomogeneous medium in terms of repeated applications of Snell’s Law.

Numerical raytracing refers to the usage of computation tools to solve the differential equations that determine the path of a ray in a given stratified medium. The equations used in this study were first pioneered by Jenifer Haselgrove in a landmark paper [Haselgrove, 1954]. This formulation properly considers both the inhomogeneity as well as the anisotropic nature of the near-Earth space plasma. In other words, in addition to the properties of the medium changing at different points in space, the group velocity is not in the direction of the phase velocity because of the presence of the ambient magnetic field. The so-called Haselgrove’s Equations are used extensively in radio science as the basis for raytracing calculations that have been crucial for the interpretation of experimental observations [Edgar, 1972; Nickisch, 2008; Ngo, 1989]. Kimura [1966] and Edgar [1972] used numerical raytracing to elucidate that observed frequency-time signatures of nonducted lightning-generated whistler waves were the result of the magnetospheric reflection process.

While the original Haselgrove’s equations were three dimensional, it is common to neglect azimuthal variations and only trace rays in the meridional plane. The

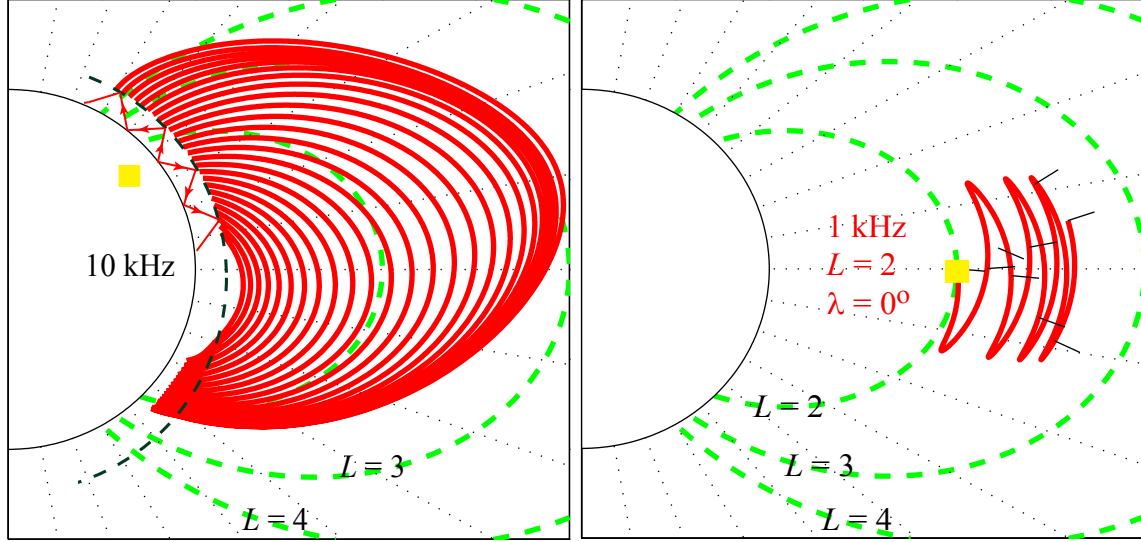


Figure 2.1: Raypaths as calculated by the Stanford VLF raytracing program. The left panel shows the type of rays that would be typically injected by a ground-based VLF source. The dashed black line refers to the base of the magnetosphere. The right panel shows the same for a space based transmitter. In both figures, the yellow box denotes the source-location.

differential equations used in this study, as given in *Kimura* [1966], are:

$$\frac{dr}{dt} = \frac{1}{\mu^2} \left(\rho_r - \mu \frac{\partial \mu}{\partial \rho_r} \right) \quad (2.1a)$$

$$\frac{d\varphi}{dt} = \frac{1}{r\mu^2} \left(\rho_\varphi - \mu \frac{\partial \mu}{\partial \rho_\varphi} \right) \quad (2.1b)$$

$$\frac{d\rho_r}{dt} = \frac{1}{\mu} \frac{\partial \mu}{\partial r} + \rho_\varphi \frac{d\varphi}{dt} \quad (2.1c)$$

$$\frac{d\rho_\varphi}{dt} = \frac{1}{r} \left(\frac{1}{\mu} \frac{\partial \mu}{\partial \varphi} - \rho_\varphi \frac{dr}{dt} \right) \quad (2.1d)$$

where r and φ are the distance from the center of the Earth and colatitude respectively, μ is the refractive index, ρ_r and ρ_φ are radial and colatitude components of the refractive index vector (a vector of length μ oriented parallel to the wave \mathbf{k} -vector), t is the integration variable and f is the wave frequency.

The Stanford VLF raytracing program [Inan and Bell, 1977] used in this dissertation integrates these equations with a 4th order Runge-Kutta routine along with an Adams predictor-corrector [Hairer *et al.*, 2000b,a]. Figure 2.1 shows two sample raypaths calculated with the Stanford VLF raytracer. The left panel shows 10 kHz rays injected from 1000 km altitude, representative of rays that would be injected by a ground-based VLF source. Note that VLF waves originating from a single source (yellow box) first propagate within the Earth-ionosphere waveguide over a broad range of geomagnetic latitudes. From each of these locations the wave energy propagates up through the lower ionosphere and enters the magnetosphere. Beyond the sharp boundary of the lower ionosphere, the assumptions of numerical raytracing are satisfied and it is possible to calculate the raypath using Equations (2.1). Due to their relatively high frequency, 10 kHz waves make only a single traverse of the magnetosphere. Also note that they propagate to relatively large L -shells, up to $L \simeq 3$. The panel on the right displays a 1 kHz ray injected by a space based source at $L=2$. Note that this ray reflects in the magnetosphere multiple times along its path, typical for few kHz whistler-mode waves in the inner magnetosphere [Edgar, 1972].

The Stanford VLF raytracing code has previously been used by Bortnik *et al.* [2003b] to model the frequency-time spectra of lightning-generated magnetospherically reflecting (MR) whistler waves. Bortnik *et al.* [2003b] reproduced the frequency-time signatures of MR whistlers observed by Smith and Angerami [1968], and also found agreement with observations made by Shklyar and Jiřiček [2000] and Edgar [1972].

Note that Equations (2.1) above requires calculating the refractive index μ . The derivation of μ in a cold magnetoplasma is done elsewhere [Bittencourt, 2004; Stix, 1992] and is not repeated here. For the purpose of our work, it is simply important to know that the refractive index depends on the magnetic field and local electron and ion species densities. Above $L=2.25$, we use the Carpenter and Anderson [1992] model under geomagnetically quiet conditions for the cold plasma density, with a plasmopause at $L=5.5$, and other parameters $d=0$, $t=2$, $K_{p(\max)}=0$, and $\bar{R}=90$ being for day of year, time of day, maximum K_p in the preceding 24 hours and average 13-month sunspot number. Below $L=2.25$, we model the cold plasma electron density

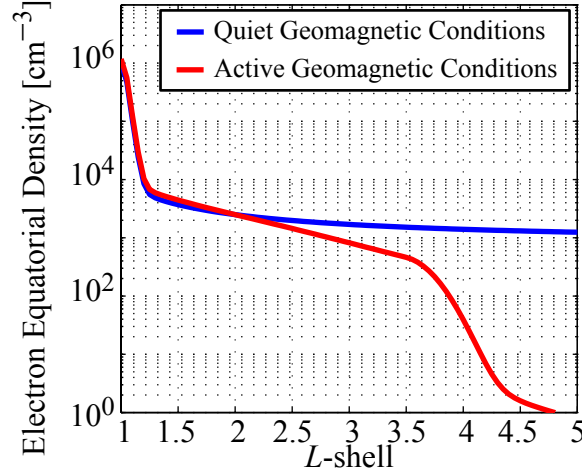


Figure 2.2: The two cold plasma density models used in this work.

with the diffusive equilibrium model of *Angerami and Thomas* [1964]. We have also investigated the effect of more active geomagnetic conditions, where $K_{p(\text{max})}=4$ and the plasmapause is at $L=3.8$. The K_p index, a method of quantifying geomagnetic activity, runs from 0 (geomagnetically quiet conditions) to 9 (very strong geomagnetic storms).

Figure 2.2 shows these density models. Note that up to $L \simeq 2.6$ there is negligible difference between active and quiet geomagnetic conditions. Accordingly, changing the density model does not affect our results for space-based sources, which are located within the plasmasphere. For ground-based sources, changing the density model does modify the distribution of raypaths and thus our results, as described in greater detail in Chapter 5. For the magnetic field, the Stanford VLF raytracing program adopts a centered dipole with a value of 880 kHz for the electron cyclotron frequency at the equator at the Earth's surface [*Inan and Bell*, 1977]. At the locations of interest, i.e., within the plasmasphere, these assumptions are well justified.

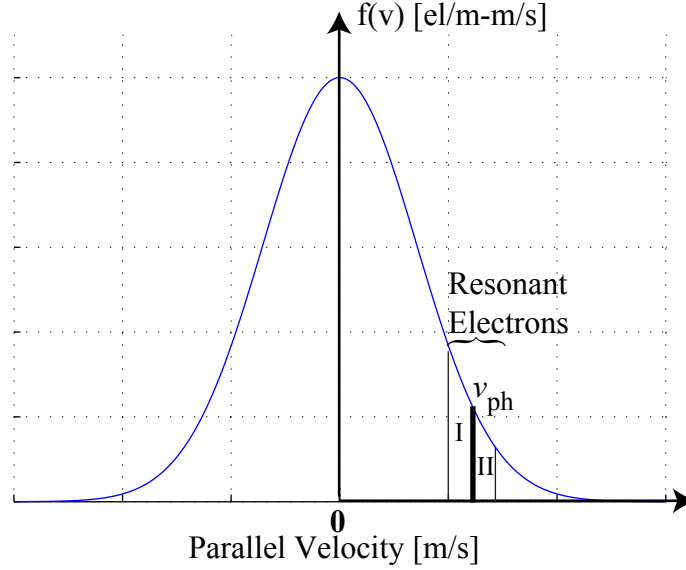


Figure 2.3: A picture of a one-dimensional Maxwellian distribution, where v_{ph} is the phase velocity of the wave. Electrons with velocities close to v_{ph} will resonate with the wave. Because area I is larger area II, the wave will be damped.

2.2 Landau Damping

Lev Landau, the great Russian theoretical physicist, first recognized the collisionless damping mechanism that carries his name in 1946 [Landau, 1946]. Though his derivation appeared to be mathematically sound and innovative, the physical process governing this phenomena was not elucidated in the literature. Landau damping occurs because of a resonance interaction between the wave and electrons traveling with a parallel (with respect to the ambient magnetic field) velocity close to the phase velocity of the wave. As the wave propagates, its electric field accelerates and decelerates resonant electrons, causing them to gain or lose energy respectively. If the wave moves faster (slower) than the electron, the electron is accelerated (decelerated), causing the wave to lose (gain) energy. Over time, the wave is damped if there are on average more particles with a slower velocity than that of the wave. The distribution of resonant electrons (i.e., electrons with thermal velocities close to the wave phase velocity) therefore determines whether damping occurs.

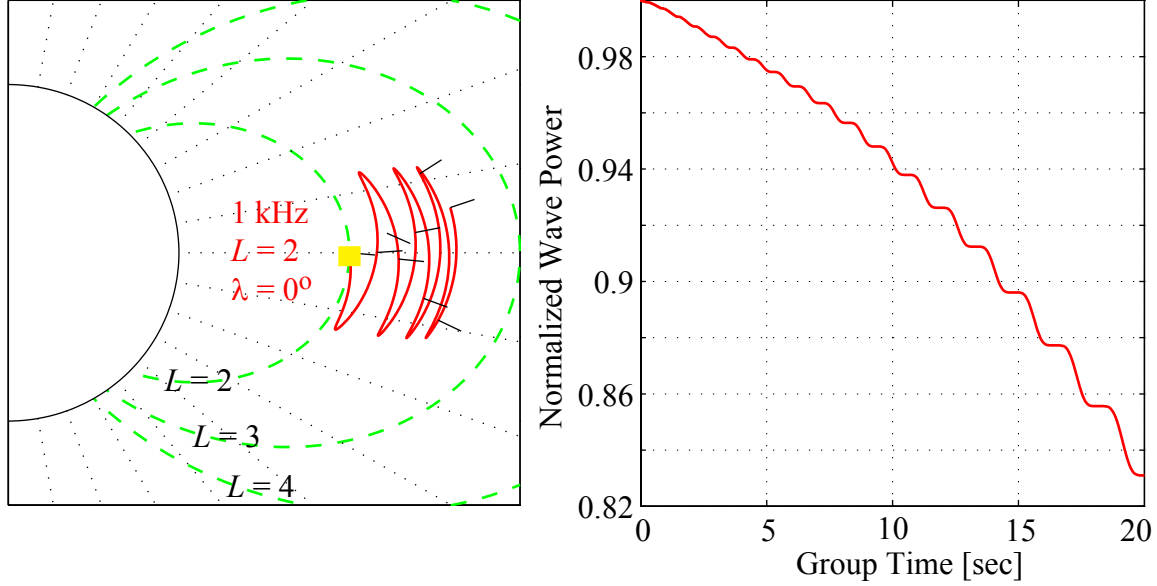


Figure 2.4: Raypath and Landau damping of a 1 kHz ray injected from $L=2$ at the equator.

Consider as an example Figure 2.3, which shows a one-dimensional Maxwellian distribution. The wave phase velocity v_{ph} is labeled on the horizontal axis. The narrow area around v_{ph} represent the resonant velocities. Electrons with a thermal velocity in this range resonate with the wave and take part in damping. Note that the area to the left of v_{ph} (labeled I) is larger than the area to the right (II), implying that there are more particles with velocities slower than the wave. Overall more particles will gain energy from the wave rather than lose energy to it, resulting in wave attenuation. In fact, waves are damped as long as the electron distribution function decreases with energy.

Landau damping only occurs when electrons have a non-zero thermal velocity along the wave propagation direction. Although the magnetospheric plasma is often accurately modeled under the cold-plasma assumption, i.e., $T_e=0$ where T_e represents the electron temperature, there is in fact a distribution of thermal velocities. Electrons from $\sim 100 \text{ eV}$ to 1 keV are generally involved in attenuating the wave via Landau

damping. While the distribution function used in this work is not a Maxwellian, in form it does exhibit a similar velocity dependence. Our formulation is based on the work of *Bell et al.* [2002], who used a numerical fit to extensive data gathered by the Polar spacecraft. The distribution function used in units of $\text{s}^3\text{-cm}^{-6}$ is:

$$f(v) = \frac{a}{v^4} - \frac{b}{v^5} + \frac{c}{v^6} \quad (2.2)$$

where a , b , and c are constants equal respectively to $4.9 \times 10^5 \text{ cm}^2\text{-s}$, $8.3 \times 10^{14} \text{ cm-s}^2$, $5.4 \times 10^{23} \text{ s}^3$, and v is the electron velocity in cm-s^{-1} . To calculate attenuation, we utilize the output of the raytracing calculation and, at each time-step, determine the attenuation according to the method described in *Brinca* [1972]. Figure 2.4 shows the raypath and Landau damping for a 1 kHz wave injected from $L=2$ at the equator. Observe that the wave damps with time.

2.3 Wave-Particle Interaction

The raytracing and Landau damping calculations thus described allow us to determine the trajectory of the ray and normalized power at locations in the inner magnetosphere. To calculate the resulting wave-induced precipitation, we need to model the wave-particle interaction at these locations. To do so, we utilize the methodology of *Bortnik et al.* [2006a], based on the integration of the motion equations developed in *Bell* [1984].

Bell [1984] solves the Langevin equation of motion in conjunction with Maxwell's equations, and gyro-averages these equations to yield solutions for the resonance interaction between an obliquely propagating whistler-mode wave and an energetic electron for a general harmonic resonance m . The result is an equation for the change of the particle pitch-angle α with time:

$$\frac{d\alpha}{dt} = - \underbrace{\frac{\omega_{\tau m}^2}{k_z v_{\perp}} \left(1 + \frac{\omega \cos^2 \alpha}{m\omega_H - \omega} \right) \sin \eta}_{\text{wave forces}} + \underbrace{\frac{v_{\perp}}{2\gamma\omega_H} \frac{\partial \omega_H}{\partial z}}_{\text{adiabatic force}} \quad (2.3)$$

where

$$\omega_{\tau m}^2 = (-1)^{m-1} \omega_{\tau 0}^2 [J_{m-1}(\beta) - \alpha_1 J_{m+1}(\beta) + \gamma \alpha_2 J_m(\beta)] \quad (2.4a)$$

$$\omega_{\tau 0}^2 = \frac{\omega_1 k_z p_\perp}{\gamma m_e} \quad (2.4b)$$

$$\omega_1 = \frac{e}{2m_e} (B_x^w + B_y^w) \quad (2.4c)$$

$$\omega_2 = \frac{e}{2m_e} (B_x^w - B_y^w) \quad (2.4d)$$

$$\alpha_1 = \frac{\omega_2}{\omega_1} \quad (2.4e)$$

$$\alpha_2 = \frac{e E_z^w}{\omega_1 p_\perp} \quad (2.4f)$$

$$\beta = \frac{k_x p_\perp}{m_e \gamma \omega_H} \quad (2.4g)$$

$$k_z = k \cos \psi = \left(\frac{\omega \mu}{c} \right) \cos \psi \quad (2.4h)$$

$$k_x = k \sin \psi \quad (2.4i)$$

The variable k refers to the magnitude of the wave \mathbf{k} -vector, μ is the refractive index, $J_i(\cdot)$ are Bessel functions of the first kind of order i , v_\perp is the component of the electron velocity v perpendicular to the ambient magnetic field, ψ is the wave normal angle measured with respect to the ambient magnetic field (assumed to be in the z -direction), B_x^w, B_y^w, E_z^w are the real magnetic and electric field components of the whistler-mode wave, η is the phase between the right hand component of the wave magnetic field and v_\perp , ω_H is the electron gyrofrequency, and γ is the relativistic factor: $\gamma = \sqrt{(1 - v^2/c^2)}^{-1/2}$ where c is the speed of light.

Equation (2.3) shows that the electron pitch-angle changes as a result of both the wave forces and the adiabatic variation. In principle, an electron is trapped indefinitely on a given field line in the absence of wave forces [Walt, 1994, p. 42]. The wave forces can induce a change in the electron equatorial pitch-angle of the particle which otherwise remains constant during adiabatic motion. Wave-induced pitch-angle change accumulates only when the phase angle η remains constant for extended periods. This restriction implies that the interaction is maximally effective

where $d\eta/dt=0$, which leads to the resonance condition between an energetic electron and a whistler-mode wave:

$$v_z = \frac{m\omega_H/\gamma - \omega}{k_z} = \frac{m\omega_H/\gamma - \omega}{\omega\mu \cos\psi} c \quad (2.5)$$

where v_z is the electron resonance velocity along the Earth's magnetic field, the integer m is the resonant mode number, and the remaining terms have been defined above. This equation describes the manner in which the magnetic field (which affects ω_H) and wave frequency ω affect resonant velocity. If k_z is held constant, v_z decreases with increasing ω but increases with ω_H . Moreover, as the absolute value of m increases, the resonant energy increases. Non-zero m indicates transverse or cyclotron resonance between the wave magnetic field and electron, while $m=0$ represents the Landau resonance.

To determine precipitation, we use these equations along with extensive raytracing, Landau damping calculations, and interpolation to produce a wave map that contains the relevant parameters (refractive index, wave power, wave normal angle) at one-degree intervals along each field line from -40 to 40 degrees in geomagnetic latitude. At each one-degree interval range, these wave characteristics are used to compute the root-mean-square (i.e., averaged over Larmor phase) pitch-angle change for near loss-cone electrons with parallel velocities in a narrow range around the resonance velocity at that location. We assume that the interactions are linear (i.e., wave intensity is not large enough to phase-trap the electrons) and independent at different latitudes. To determine the total flux of precipitated particles, we apply the calculated pitch-angle changes to near loss-cone electrons (i.e., to electrons immediately above the loss cone), recognizing that their scattering is similar to that which was calculated for the electrons at the loss cone. This methodology is described in great detail in *Bortnik et al.* [2006a].

The numerical raytracing, Landau damping and wave-particle interaction models described above are necessary to properly calculate the energetic electron precipitation induced by both ground and space-based VLF sources. In addition, it is also necessary to determine the far-field Poynting flux radiated by each type of source.

This calculation yields the initial power spectrum of the rays. The specific input power calculation depends on the type of source studied. For ground-based VLF sources, we need to calculate the radiated power from the transmitter to the base of the ionosphere as well as the attenuation of wave energy through the ionosphere. The resultant wave energy at the top of the ionosphere is used as the initial condition for the raytracing and the Landau damping calculation. For a space-based VLF source, the input power calculation depends on additional models that describe the radiation characteristics of a VLF antenna immersed in the near-Earth space plasma.

2.4 Antenna Radiation and Ionospheric Absorption

To quantitatively model the precipitation induced by ground-based VLF sources, we must determine the input power at 1000 km altitude as a starting point for raytracing calculations. For this purpose, we account for VLF-antenna radiation properties, subionospheric propagation, and ionospheric absorption losses. *Rodriguez et al.* [1994] conducted an extensive study of the ionospheric modification caused by ground-based VLF transmitters. Because of the long (10–15 km) wavelengths of waves radiated by such sources, the antennas can be analyzed as short vertical monopoles on a ground plane. However, reflections from the conducting plane allows us to treat a monopole of height $h/2$ as a dipole of height h [*Rodriguez*, 1994, p. 63]. The formula for the radiated Poynting flux for a dipole of height h is given as:

$$S(r, \theta) = \frac{3P_{\text{tot}} \sin^2 \theta}{4\pi r^2}$$

where P_{tot} represents total transmitter radiated power, θ is the angle measured from the vertical dipole axis, and r the radial distance from the dipole axis to the observation point [*Rodriguez*, 1994, p. 65, Eq 4.6]. We use the above formula to calculate the Poynting flux at the base of the ionosphere, taken to be at 100 km altitude, at points ranging from 10° to 60° latitude with r measured from the source location.

From the base of the ionosphere, the wave energy is assumed to propagate vertically through the ionosphere to the base of the magnetosphere (i.e, from 100 to 1000 km), and is attenuated according to a night-time absorption factor taken from [Helliwell, 1965, Fig. 3-35]. This collisional absorption in fact occurs over the altitude range of $\sim 75\text{--}120$ km, where the imaginary part of the refractive index (representing attenuation due to collisional losses) is large, and is dependent on the particular ionospheric profile in effect at the time [Helliwell, 1965, Fig. 3-29]. However, for our purposes here we simply need to capture its magnitude in an average sense, but more importantly its dependence on geomagnetic latitude. We thus use an interpolation of the results given in [Helliwell, 1965, Fig. 3-35], including the dependence on geomagnetic latitude.

In this way, our results incorporate the different absorption that would occur for different transmitter locations and operating frequencies. More specifically, our location-dependent precipitation signatures include the effects of, for example, higher absorption at 20° versus 50° , and 20 kHz versus 10 kHz. However, we do not include the up to 3 dB polarization loss, as this is constant for all locations and transmitters and thus does not affect our comparative analysis of the effects of different input parameters (see Chapter 5). For the purpose of this study, we assume a smoothly varying ionosphere without horizontal density gradients so that the wave normal angles at 1000 km are largely vertical. After entering the magnetosphere, the rays propagate in a manner determined by the cold plasma density and Earth’s magnetic field gradients as described above.

To calculate the energetic (>100 keV) electron precipitation induced by space-based VLF transmitters, we must incorporate the radiation pattern of an antenna immersed in a magnetoplasma. Wang and Bell [1970] modeled the radiation properties of a short, electric dipole oriented perpendicular to the ambient magnetic field, radiating in the VLF range, in a magnetoplasma. The authors ignored the effects of the plasma sheath and any warm plasma effects. In this context, we note that our results can also be used with any other antenna-in-magnetoplasma-model. We choose the Wang and Bell [1970] model for our work because it specifically addressed the VLF frequency range that we are interested in and presents results that encompass

the magnetoplasma parameter ranges of interest.

The *Wang and Bell* [1970] model indicates that a perpendicular dipole in a magnetoplasma emits the bulk of its radiated power as waves at wavelengths approximately equal to the antenna length. Wave frequencies well below the local lower hybrid resonance frequency f_{LHR} have very long ($\gtrsim 1$ km) wavelengths. For antenna lengths of 100–500 meters and for waves of a few kHz at the source sites considered here, this result effectively restricts the driving frequency f to $f \gtrsim 0.9 f_{\text{LHR}}$. In our calculations, the frequency is furthermore limited to 1 kHz above the local f_{LHR} because of strong Landau damping for higher frequencies (see Chapter 3). Waves operating at frequencies, for example, 2–3 kHz above the local f_{LHR} are attenuated by more than 10 dB within 1–2 seconds and thus produce only a small fraction of the total precipitation.

Due to the anisotropic nature of the magnetospheric plasma, the wavelength is strongly dependent on the wave normal ψ along with wave frequency. For ψ more than $\sim 3^\circ$ from the resonance cone angle ψ_{res} , the wavelength is much longer than antenna lengths of a few hundred meters. We therefore consider only \mathbf{k} -vectors that lie within 3° of ψ_{res} . See the Appendix for a more complete derivation of this assumption. To summarize, we restrict the frequency from $0.9 f_{\text{LHR}}$ to 1 kHz above the local f_{LHR} ($f_{\text{LHR}} + 1$ kHz). We also select initial wave normal angles ψ to within 3° of the local resonance cone ψ_{res} . A more detailed description of the rationale with which we limit our choice of the initial wave parameters is given in *Kulkarni et al.* [2006], and the complete derivation can be found in *Wang and Bell* [1969].

Chapter 3

Distribution of Whistler-Mode Wave Energy

3.1 Introduction

To precipitate energetic electrons with space-based VLF sources, it is necessary to understand the manner in which whistler-mode wave energy injected from a space based source distributes in the inner magnetosphere. This chapter aims to expand on the initial results presented in *Inan et al.* [2003] by utilizing the Stanford VLF raytracing code [*Inan and Bell*, 1977] coupled with an accurate estimation of the path-integrated Landau damping to determine the distribution of wave energy throughout the inner radiation belt based on injection location, wave frequency and injection wave normal angle.

We first focus on a single transmitter at $L=2$ and consider both equatorial and off-equatorial injection points for wave frequencies ranging from well below, to well above, the local lower hybrid resonance (LHR) frequency and also for a broad range of injection wave normal angles. We initially neglect the details of antenna radiation in a magnetoplasma in order to facilitate a more complete picture of whistler-mode wave propagation in the inner magnetosphere as a result of space based injection. We then modify these results by incorporating the limitations that would be imposed by the *Wang and Bell* [1970] model for a short electric dipole radiating in a magnetoplasma.

These results demonstrate that a space based source can target L -shells both higher and lower than the source site by varying the frequency of the injected waves, with wave frequencies below (above) the local lower hybrid resonance, f_{LHR} , moving to higher (lower) L -shells. We show that only three sources placed at various locations in the inner magnetosphere are required to project wave power over the range $1.4 \leq L \leq 2.7$ (i.e., to illuminate this region), which comprises the bulk of the inner radiation belt.

The work presented in this Chapter has been previously published in *Kulkarni et al.* [2006], but is repeated here for completeness. We begin by introducing the magnetospheric cavity enhancement factor, a parameter that is used throughout this Chapter.

3.2 Magnetospheric Cavity Enhancement Factor

As noted by *Edgar* [1976], whistler-mode waves in the magnetosphere can undergo total internal reflections as they propagate from regions where the wave frequency f is above the lower hybrid frequency f_{LHR} to points where $f \simeq f_{\text{LHR}}$. This reflection process can occur numerous times, with the magnetosphere thus constituting a resonant ELF/VLF cavity wherein repeated reflections may lead to persistent presence of wave energy and resultant enhancement of induced precipitation. To properly quantify the manner in which wave energy is distributed within the magnetosphere, we must thus properly account for the fact that successive reflections may cause wave energy represented by a single injected ray to cross the same region numerous times before the wave power is significantly damped. To this end, we introduce the concept of the magnetospheric cavity enhancement factor (see below) to quantify the combined effects of magnetospheric reflections and Landau damping along the ray path. The ray path and attenuation change dramatically with the input parameters, as is examined in greater detail below. (For the remainder of this study the parameter λ refers to the geomagnetic latitude in degrees.)

Spacecraft observations indicate that a single whistler-mode wave can magnetospherically reflect up to 40 times before being significantly damped [*Smith and Angerami*, 1968; *Edgar*, 1976; *Gurnett and Inan*, 1988], resonantly interacting with,

and pitch-angle scattering, energetic electrons at all points along the ray path. We nevertheless focus our attention on the magnetic equator because the slow variation of the Earth’s magnetic field at that point allows for the longest interaction time for the fixed frequency signals considered here. Accordingly the wave-particle interactions are most effective at that region, which results in the highest diffusion (or scattering) coefficients. We then divide the magnetic equator into equally sized radial “bins” of, e.g., $0.1L$ in length and, for each equatorial crossing, note the location of the ray in L -shell and assign it to the appropriate L -bin. To arrive at the cavity enhancement factor for each L -bin, we simply sum the normalized wave power (i.e., starting with a value of unity at the injection point) for every crossing of that bin by any ray.

To illustrate this concept consider the ray path shown in Figure 3.1a of a 2.5 kHz wave injected from $L=2$ at the magnetic equator with an initial wave normal angle ψ of -85° . For simplicity, only the injection and the first two equatorial crossings are expanded and shown in more detail in Figure 3.1b, along with the normalized wave power as attenuated by Landau damping and the location in L -shell of the ray at each magnetic equatorial crossing. We then divide the magnetic equator into bins such that the ray position at injection ($L=2.0$) and first equatorial crossing ($L=2.08$) are both assigned to the $L=2.0$ shell, and the ray position at the second equatorial crossing ($L=2.13$) is assigned to the $L=2.1$ shell. Finally, for each L -bin, we sum the normalized wave power of the ray at every equatorial crossing within that bin to determine the resulting cavity enhancement factor. Referring again to Figure 3.1b, the cavity enhancement at the $L=2.0$ shell is 1.996 (normalized power of 1.0 at injection plus a ray power of 0.996 at the first crossing) and 0.992 at the $L=2.1$ shell. Of course, had we examined more than just the first two crossings, the cavity enhancement factor at both the $L=2.0$ and the $L=2.1$ regions may have been higher and the ray may also have propagated (and thus carried wave energy) to additional L -shells. Figure 3.1c displays the cavity enhancement factor at the $L=2.0$ and $L=2.1$ shells after the first two equatorial crossings. It is important to note that a cavity enhancement factor greater than unity does not imply amplification of the wave power; it simply represents the fact that, for example, an injected signal of 1-sec duration would cross the geomagnetic equator multiple times over a time period

longer than 1-sec, scattering electrons each time. A cavity enhancement factor of 1.5 thus implies that this signal could be 1.5 times more effective in pitch-angle scattering than it would have been in the absence of magnetospheric reflections. Alternatively, for the case of injection of a continuous wave train, we can think of the enhancement factor as the factor by which the total wave power multiplicatively increases with time as the wave energy is stored within the cavity. The magnetospheric reflections thus allow a single wave packet to interact with the energetic particles multiple times, with the wave power density decreasing with time. Accordingly, with several equatorial passes, the cumulative normalized wave power at a given L -shell region is effectively greater than unity.

We also note that the cavity enhancement factor discussed herein differs from the cavity enhancement ‘gain’ factor, G_c , described in *Inan et al.* [2003]. The latter was determined by weighting each equatorial crossing (regardless of the L -value) with the wave power density at that point. The convention adopted in this dissertation quantifies more precisely the L -shell distribution of the wave energy, accounting for the fact that successive rays can cross different L -bins. The two approaches are similar in that we can arrive at the G_c values used by *Inan et al.* [2003] by simply summing the cavity enhancement factor at the different L -bins.

3.3 Simulation Results

As discussed above, our objective in this chapter is to quantify the projection of electromagnetic wave power onto a specific L -shell region from a particular injection point in space. At any given time, it may be desirable to project wave power either to regions close to the satellite location or to L -shells far away from the source. The input parameters (wave frequency and wave normal angle at injection) are likely to be different depending on the location of the satellite and the region where we wish to project wave power. We therefore simulate a substantial number of rays with a range of input parameters so that conclusions can be drawn with regards to appropriate frequencies and wave normal angles. One particular question of practical interest is to determine the number and location of space-based sources needed to completely

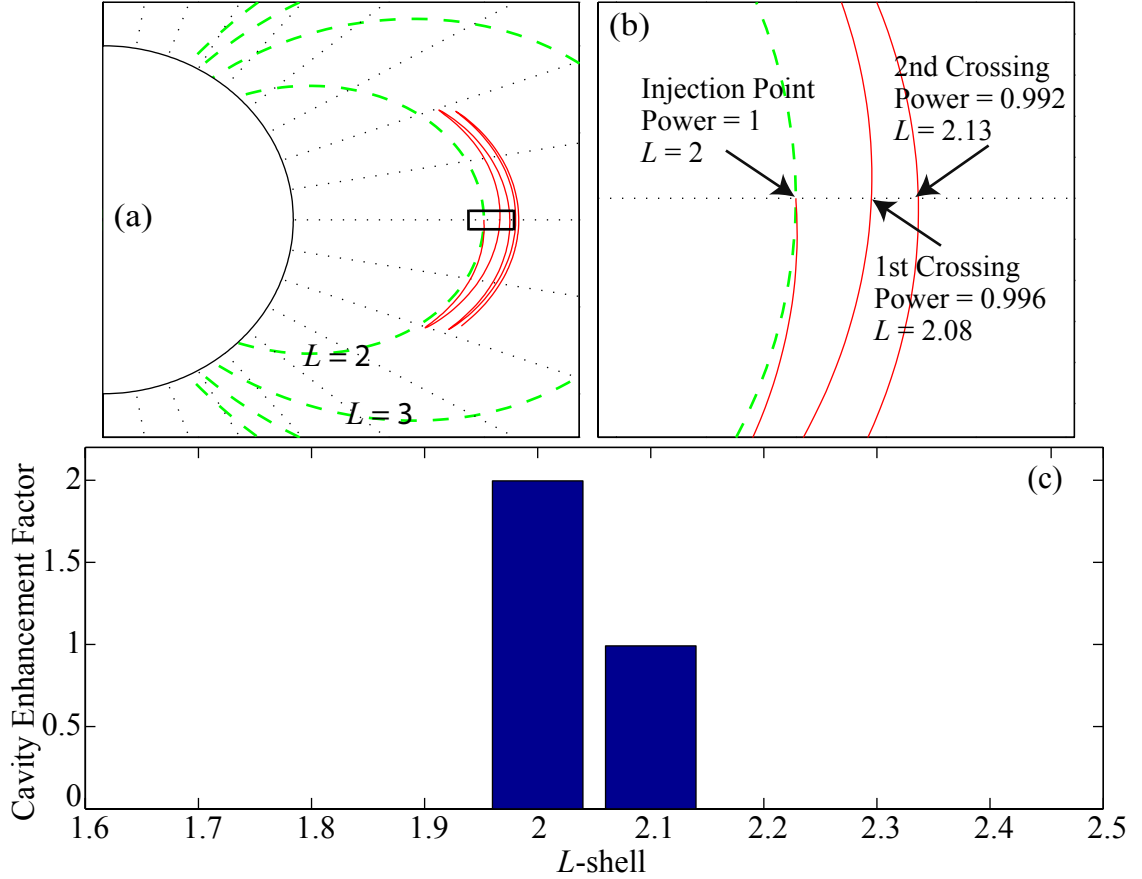


Figure 3.1: (a) Ray path of a 2.5 kHz signal injected at the geomagnetic equator at $L=2$ with an initial wave normal angle of -85° . (b) An expanded portion from the ray path shown in (a). (c) The cavity enhancement factor after signal injection plus the first two equatorial crossings.

illuminate the region $1.3 < L < 3$ with ELF/VLF whistler-mode wave energy.

The simulation procedure we use is as follows: We first start with a given injection L -shell and magnetic latitude. We consider three such L -shell locations ($L=1.5$, $L=2.0$ and $L=2.5$) as well as two geomagnetic latitudes, the equator and a latitude of 20° along each field line. This set of parameters constitutes a total of six different injection source sites. For each source site, we then inject waves at 100 different frequencies ranging from 1–10 kHz, in increments of 0.1 kHz, and, for each wave frequency, with initial wave normal angles from -75° up to the resonance cone if $f > f_{\text{LHR}}$ or up to

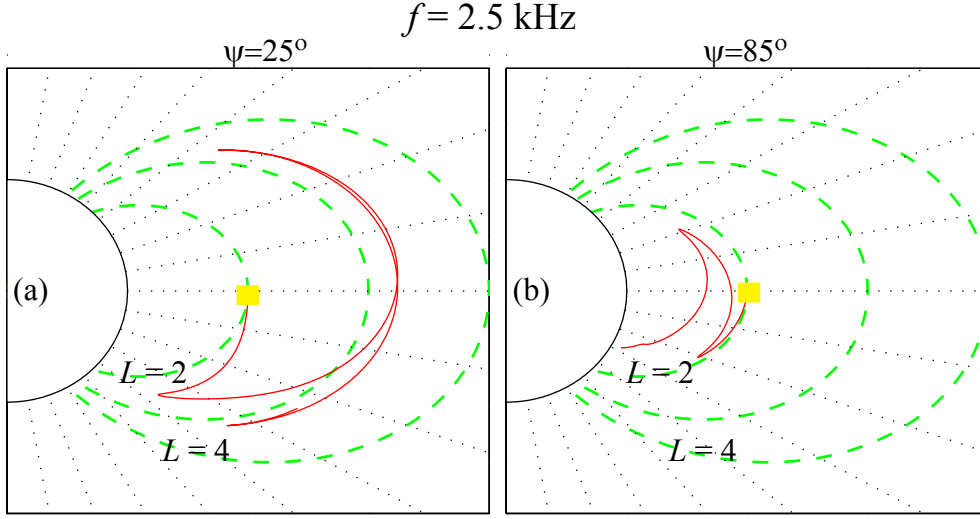


Figure 3.2: (a) Ray path of a wave injected at $L=2$ at the geomagnetic equator, at an initial wave normal angle of 25° . (b) A ray with an initial wave normal angle of 85° is absorbed in the ionosphere very quickly.

-89.9° for $f < f_{\text{LHR}}$, with each wave normal angle separated by 0.1° . For each ray, we also calculate the path-integrated Landau damping and the cavity enhancement factor at the geomagnetic equator. The frequency range is chosen to encompass frequencies ranging from well below the local LHR frequency at all equatorial regions in the inner radiation belts up to a frequency for which magnetospheric reflections no longer occur. We consider initial wave normal angles that are pointing away from the earth, $\psi < 0$, because rays with an initial inward pointing wave normal angle, $\psi > 0$, tend to take a longer time to reach their settling L -shell (see below), or get absorbed into the ionosphere. Figure 3.2 shows the raypaths for two 2.5 kHz rays, one with an initial wave normal angle of 25° and the other 85° .

The bulk of the simulation results shown are for a source located at $L=2$ for which we separately examine equatorial and off-equatorial injections. However, before presenting the bulk of the simulation results, it is instructive to briefly explore whistler-mode wave behavior in the inhomogeneous magnetospheric medium, especially the phenomena of the wave energy settling on a prescribed L -shell (dependent only on wave frequency) and also the relationship between initial wave parameters (frequency, wave normal angle) and the lifetime (i.e. cavity enhancement factors).

3.4 *L*-shell Settling and Wave Lifetimes

Whistler-mode waves propagating in the magnetosphere have the strong tendency, within the course of few initial magnetospheric reflections, to settle on an *L*-shell where the wave frequency is approximately equal to the equatorial f_{LHR} [Thorne and Horne, 1994; Ristic-Djurovic *et al.*, 1998]. Manipulation of the wave frequency thus represents a first order means for targeting a particular *L*-shell. The f_{LHR} frequency ($f_{\text{LHR}} \simeq (f_{\text{He}} f_{\text{Hi}})^{1/2}$ for $L=2$, where f_{He} is the electron gyrofrequency and f_{Hi} is the ion gyrofrequency), is generally larger at locations closer to the Earth's surface. To selectively target lower *L*-shell field lines, frequencies higher than the local f_{LHR} should be used, while lower frequencies should be used to project power toward higher *L*-shells. This behavior is a strong function of wave frequency and does not change substantially with the injection location (*L*-shell and geomagnetic latitude) or injection wave normal angle, although some exceptions will be noted. However, waves with an initially smaller normal angle or waves injected off the magnetic equator tend to propagate farther from their injection point before returning back, thereby taking a longer time to reach their settling *L*-shell. Figure 3.3a demonstrates this principle by showing *L*-shell location versus group travel time for four separate injections from $L=2$ ($f_{\text{LHR}} \simeq 2.5$ kHz) of 4 kHz waves. All four rays move, as expected, to lower *L*-shells and eventually settle on $L \simeq 1.72$, where the equatorial f_{LHR} is ~ 4 kHz.

The presence of path-integrated Landau damping greatly limits the ability of a whistler-mode wave of a given frequency to reach its settling *L*-shell without significant power loss. For space-based injections, waves injected above the local f_{LHR} or off the geomagnetic equator experience especially strong damping [Bortnik *et al.*, 2003a]. To clarify the preceding point, Figure 3.3b shows that such rays are Landau damped by 10 dB after only 10 seconds and these rays therefore do not reach their settling *L*-shell with significant intensity. Nonetheless, inspection of Figure 3.3a indicates that the rays have begun propagating toward lower *L*-shells at this point, with two out of the four rays reaching $L \simeq 1.8$. The various tradeoffs apparent from the above discussion, between injecting higher or lower frequency waves at equatorial and off-equatorial sites, are examined in more detail below.

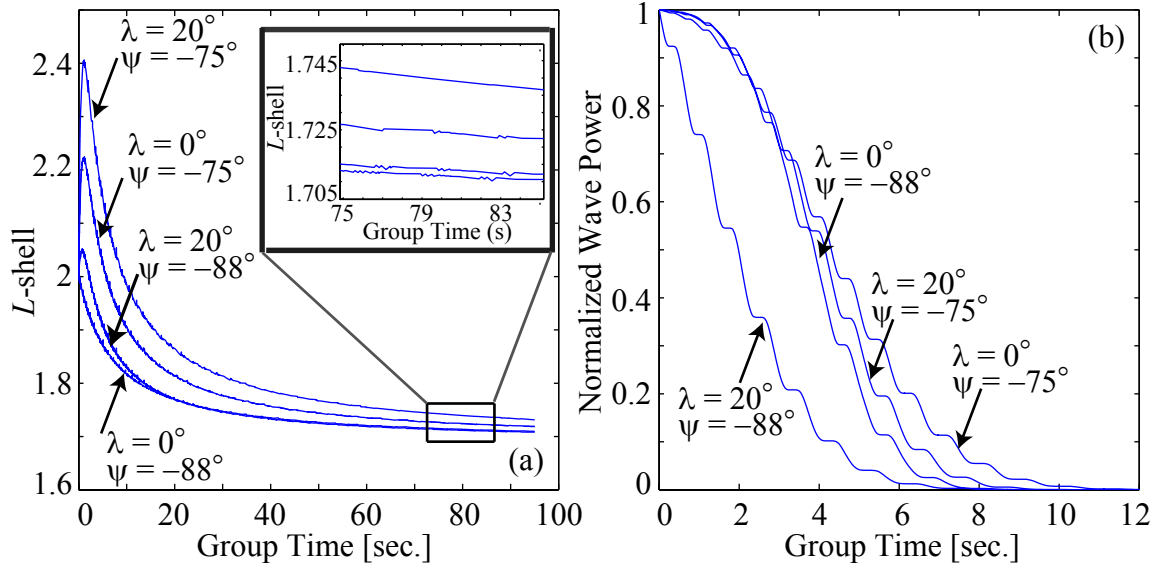


Figure 3.3: (a) L -shell versus group time for 4 kHz waves injected at $L=2$. For a wide range of injection latitudes and wave normal angles, all four rays eventually settle on $L \sim 1.72$ (expanded portion shown in inset). (b) Landau damping for the rays shown in (a).

3.4.1 Injections at the Geomagnetic Equator

We first consider a single wave-injection source at $L=2$ at the magnetic equator radiating 2.5 kHz waves, approximately equal to the local lower hybrid resonance frequency. Such waves tend to stay very close to the source location and are damped more slowly than waves with frequencies higher than the local f_{LHR} [Bortnik *et al.*, 2003a]. The resultant raypath and damping are also dependent on the wave normal angle at injection, with wave normals initially closer to the resonance cone persisting much longer and resulting in larger cavity enhancement factors. This point is illustrated in Figure 3.4, which shows that, for 2.5 kHz waves, changing the wave normal angle ψ at injection from -75° to -85° to -89° results in progressively longer ray lifetimes and larger cavity enhancement factors. However, the rays injected with $\psi = -75^\circ$ and -85° disperse much farther than the ray injected $\psi = -89^\circ$ and hence interact with energetic electrons over a broader range of L -shells. Examining rays injected at a continuum of normal angles from -75° to -89.9° indicates that, although 2.5 kHz waves usually propagate slightly outward from $L=2$, certain

L -shells can be preferentially targeted by carefully choosing the injection wave normal angle. For example, as shown in Figure 3.5, a 2.5 kHz wave injected from the equator at $L=2$ with $\psi=-80^\circ$ remains in the $L=2.2$ equatorial region during most of its lifetime, but also crosses the magnetic equator near $L=2.2$, $L=2.1$ and $L=2.0$. Conversely, a 2.5 kHz wave initially with $\psi=-89^\circ$ remains very close to the injection source and does not significantly illuminate remote L -shells.

We also show the effect of injecting, from $L=2$ at the geomagnetic equator, waves with frequencies both well below and above the local f_{LHR} . As stated earlier, waves at a frequency below (above) the local f_{LHR} generally move to higher (lower) L -shells and are also damped more slowly (quickly). As a consequence of longer lifetimes, lower frequency waves also tend to attain overall larger cavity enhancement factors, although the L -shell regions of wave energy deposition differs from that of higher frequency waves. Figure 3.6 demonstrates these effects by showing the result of injection of both a 1 and 4 kHz wave at $\psi=-85^\circ$. The 1 kHz wave immediately propagates to higher L -shells and persists for well over 60 seconds, whereas the 4 kHz wave moves closer to the Earth and its normalized power is reduced by ~ 10 dB within 10 seconds. Additionally, the maximum equatorial cavity enhancement factor for the 1 kHz ray occurs at $L \simeq 2.8$, but occurs at $L \simeq 2.0$ for the 4 kHz ray. Although the raypath for the 4 kHz wave migrates down to $L \simeq 1.7$, strong Landau damping prevents significant wave power from reaching those lower L -shells.

Our results indicate that it may be particularly difficult to project wave power to some regions of the magnetosphere with a single source located at $L=2$. Attempting to direct wave energy to $L=1.3$, for example, would require the use of higher frequency (e.g., ~ 9 kHz) waves that often tend not to undergo magnetospheric reflections and that also would Landau damped very quickly. On the other hand, taking advantage of cavity enhancement at L -shells as far away as $L=3.5$ is not possible with a single equatorial source at $L=2$. To fill larger regions of the plasmasphere with whistler-mode wave energy, one must therefore vary the radial distance where the satellite is placed. For injections from locations closer to the Earth we expect that the higher f_{LHR} implies higher frequencies should be used to target the source L -shell while lower frequencies should be used for injection sites farther from the earth. As described

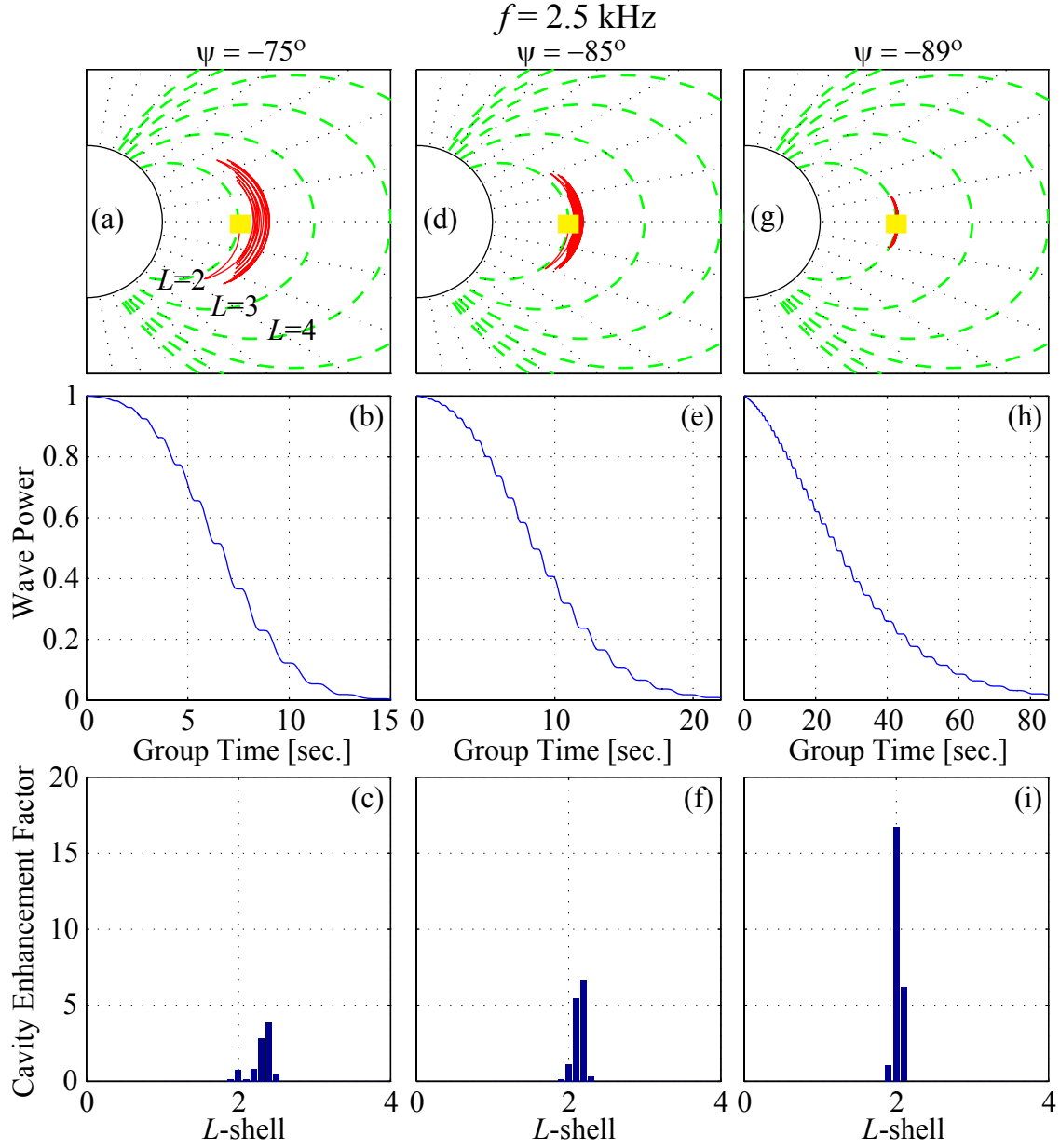


Figure 3.4: (a) Ray path of a 2.5 kHz ($\sim f_{\text{LHR}}$) signal injected at the equator at $L=2$ at a wave normal angle of -75° . (b) Normalized wave power along the ray path. (c) Cavity enhancement factor at equator as a function of L -shell. (d) - (f) Ray path, Landau damping and cavity enhancement factor for a wave injected at a wave normal angle of -85° . (g) - (i) Initial wave normal angle of -89° .

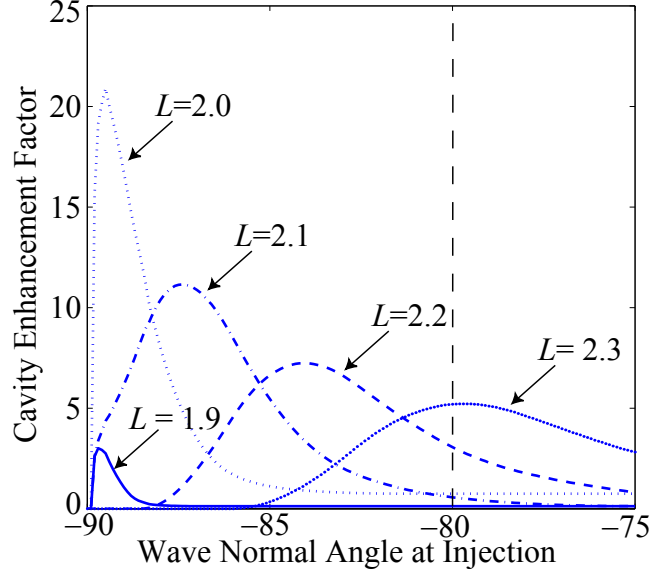


Figure 3.5: Cavity enhancement factor as a function of injection wave normal angle for a 2.5 kHz wave at $L=2$ at the geomagnetic equator. A vertical line drawn from the horizontal axis represents how wave power disperses in L -shell for a single injection at a specific initial wave normal angle.

previously, we examine the wave power propagation from space-based sources located at $L=1.5$ and $L=2.5$ and, to compare with the results shown earlier for a satellite located at $L=2$, for 1 kHz, 2.5 kHz and 4 kHz waves.

While at $L=2$ these three frequencies are below, approximately equal to, and above the f_{LHR} respectively, at $L=1.5$ all three frequencies are well below the local f_{LHR} (~ 6 kHz). Accordingly, injections from $L=1.5$ at these wave frequencies propagate to higher L -shells and exhibit very high cavity enhancement factors as a result of longer lifetimes. This result can be seen in Figure 3.7, showing a comparison of the integrated cavity enhancement factor (integrated along the raypath, then normalized, over all wave normal angles considered), for injections from the equator at $L=1.5$, $L=2.0$ and $L=2.5$. Note that 2.5 kHz waves injected from $L=1.5$ induce an integrated cavity enhancement factor at $L=2$ that is a factor of ~ 4 higher than 2.5 kHz waves injected from $L=2$. This result underscores the fact that wave frequencies below the local f_{LHR} persist for longer times than waves above the f_{LHR} . Also note that since the equatorial f_{LHR} is ~ 6 kHz, all three frequencies exhibit cavity enhancement primarily

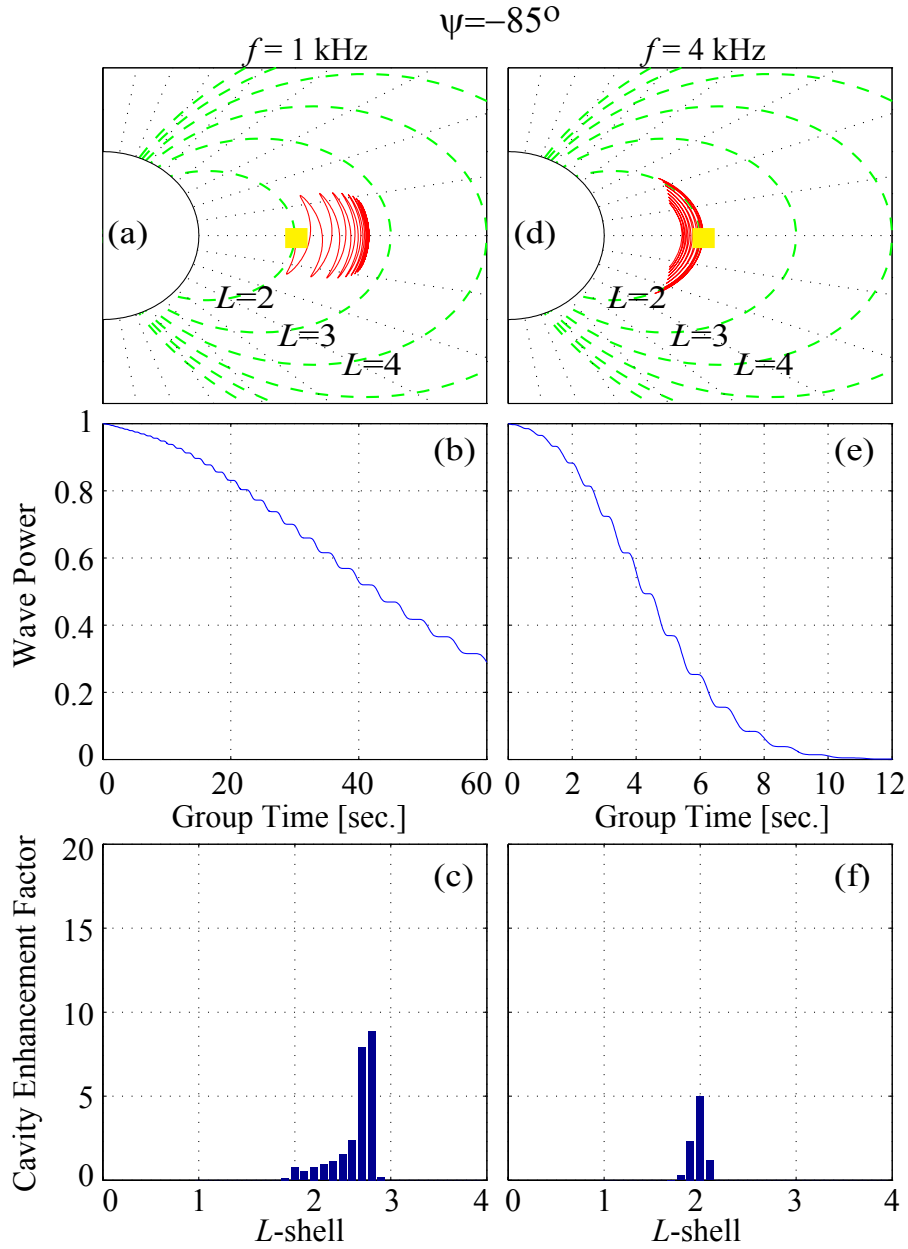


Figure 3.6: (a) - (c) Raypath, Landau damping and cavity enhancement factor for a 1 kHz signal injected at $L=2$ at the equator at a wave normal angle of -85° . (d) - (f) The same plots for a 4 kHz signal.

at *L*-shells higher than *L*=1.5.

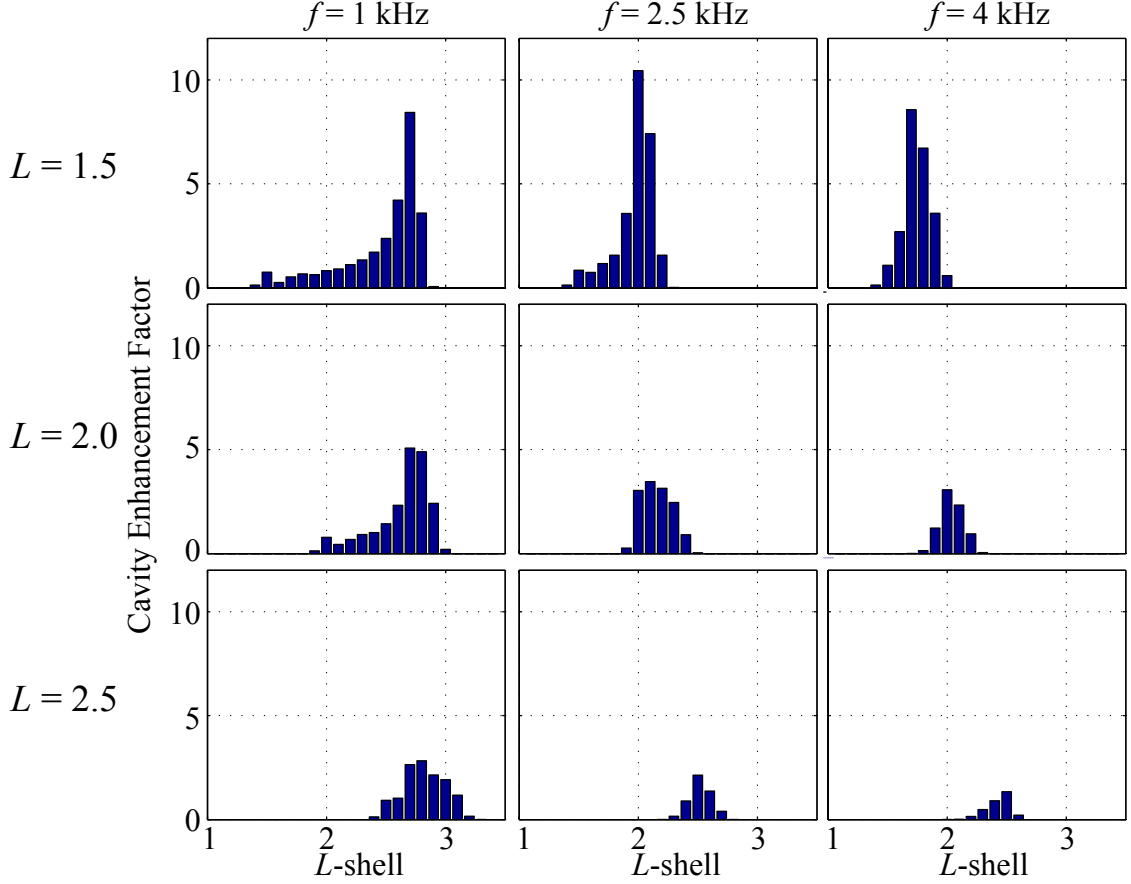


Figure 3.7: Cavity enhancement factor integrated over all wave normal angles considered and then normalized by the total number of injections. The three columns display the three sample wave frequencies of 1 kHz, 2.5 kHz, and 4 kHz; and each row represents the three separate injection source sites ($L = 1.5, 2.0, 2.5$). All waves were injected from the magnetic equator.

On the other hand, for 5 kHz, 6 kHz and 7 kHz waves, corresponding to just below, approximately equal to and above the local f_{LHR} , Figure 3.8 shows that the $L=1.5$ region can be more effectively illuminated by simply changing the input wave frequency. It is interesting to observe that even at a frequency of 7 kHz, field lines for $L < 1.3$ are not illuminated because of very rapid Landau damping and fewer magnetospheric reflections. Taking advantage of cavity enhancement at locations

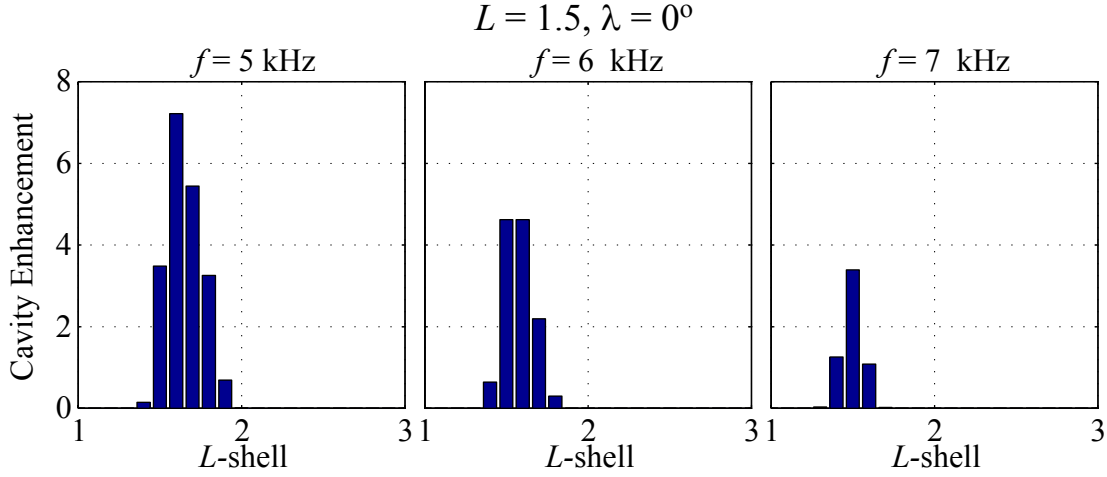


Figure 3.8: Integrated cavity enhancement factor for injection from the geomagnetic equator at $L=1.5$.

extremely close to the earth's surface ($1.1 < L < 1.3$) may therefore require sources placed at those L -shells.

In order to explore wave propagation from $L=2.5$ (equatorial $f_{\text{LHR}} \sim 1.3$ kHz), we refer to the bottom row in Figure 3.7. As opposed to the previous source locations, 2.5 and 4 kHz waves injected from $L=2.5$ are above the local f_{LHR} . They therefore propagate down to lower L -shells and get damped more quickly than similar frequency waves injected from $L=1.5$ and $L=2.0$. Interestingly, even though 1 kHz is below the f_{LHR} at all three source sites considered, injections from $L=2.5$ still cause substantially lower integrated cavity enhancement factors. Clearly, waves which are 5 kHz below the local f_{LHR} —as is a 1 kHz wave injected from $L=1.5$ —endures much longer than a wave frequency much closer to the local f_{LHR} . In fact, among the three source locations investigated so far, the integrated cavity enhancement factor is smallest for injections from $L=2.5$. Despite the smaller cavity enhancement, the results demonstrate that, for the sample frequencies shown, a single source at the geomagnetic equator at $L=2.5$ can effectively illuminate at L -shells from $L \sim 2.1$ up to $L \sim 3.2$. This illumination range does not increase significantly with the inclusion of additional, higher frequencies because these frequencies would be damped before reaching their settling L -shell.

3.4.2 Off-Equatorial Injections

Up to this point we have considered wave injection from sources located solely at the geomagnetic equator. In practice, any spacecraft-based source in orbit would necessarily spend a lot of time at locations off the equator. It is thus useful to consider the injection of waves from other locations. *Bortnik et al.* [2003a] have examined the disparity in ray lifetimes, and by implication cavity enhancement factors, for injections from different locations. Off-equatorial injections result in stronger Landau damping than equatorial ones because such waves are above the local f_{LHR} for a longer time along their path. For wave frequencies above the local f_{LHR} , the refractive index surface $\mu(\psi)$ is open and the refractive index can have a large magnitude, which leads to strong damping [*Bortnik et al.*, 2003a].

For the simulations considered here, insight into the differences between equatorial and off-equatorial injections can be gained by comparing the results in Figure 3.9 with the results shown in Figure 3.4 earlier. Here, we inject three 2.5 kHz rays from $L=2$ at a geomagnetic latitude of 20° , with initial wave normal angles of -75° , -85° and -89° respectively. For each case, the off-equatorial injection leads to more rapid damping of the wave and illumination of a wider range of L -shells than the corresponding equatorial injection.

Figure 3.10 clearly shows the differences between the two different source sites. The top (bottom) row shows the integrated cavity enhancement factor at the geomagnetic equator ($\lambda=20^\circ$). The off-equatorial injections, shown in the bottom row, consistently result in smaller integrated cavity enhancement factors but illuminate a broader range of L -shells. For instance, 2.5 kHz waves injected at the equator from $L=2$ project power up to $L=2.5$ with a normalized integrated enhancement factor as high as ~ 6 . Injections from 20° can affect L -shells as far as $L=2.7$ but also result in lower cavity enhancement factors. While similar results can be also be demonstrated for injections from $L=1.5$ and $L=2.5$, they are not shown here for the sake of brevity. Chapter 4, however, shows the induced precipitation for all source sites.

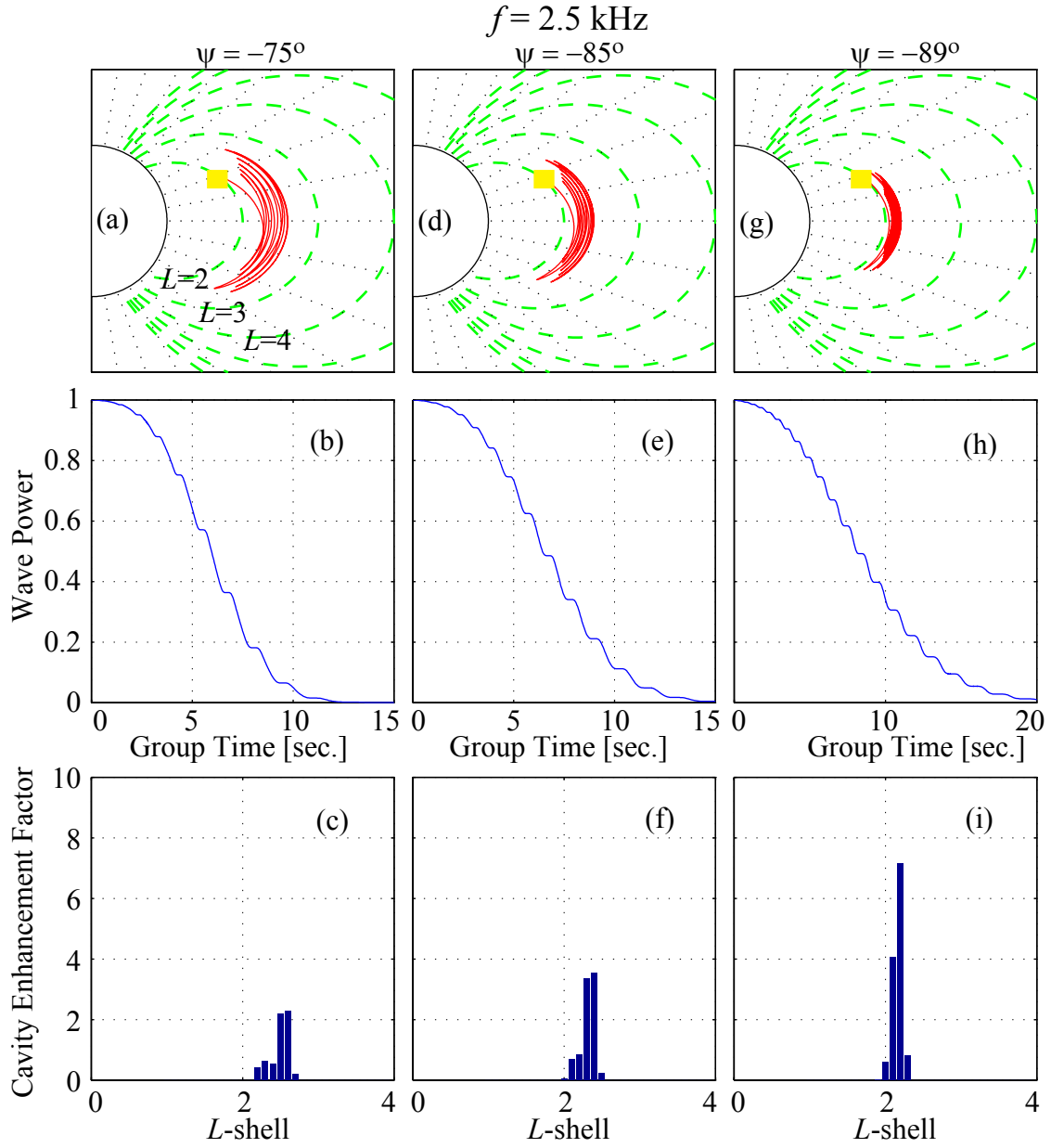


Figure 3.9: Ray paths, Landau damping and cavity enhancement factors for 2.5 kHz waves injected from $L=2$ at $\lambda=20^\circ$.

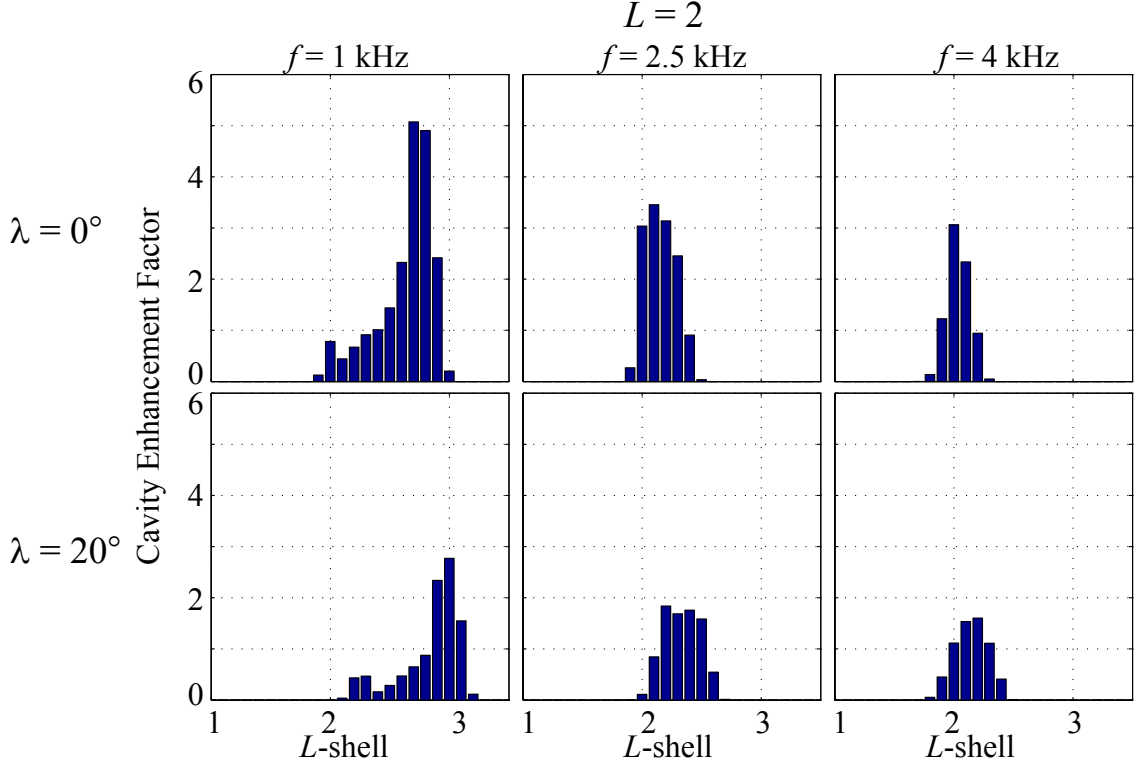


Figure 3.10: Cavity enhancement factor integrated for sources at $L=2$ at the equator and $\lambda=20^\circ$.

The tradeoff between greater more localized cavity enhancement factors for equatorial injections versus smaller more distributed cavity enhancement factors for off-equatorial injections may be important in the design of a practical system for controlled precipitation of radiation belt electrons.

3.4.3 Comparison and Analysis

We have investigated the effects of varying three principal parameters: injection source location, wave frequency and initial wave normal angle. The results presented thus far allow us to highlight the primary tradeoffs in these parameters. First, it is important to observe that across all injection locations considered ($L=1.5$, $L=2$ and $L=2.5$) there is a consistent pattern of equatorial injections resulting in a larger integrated cavity enhancement factor than off-equatorial injections, but also affecting

a narrower region of L -shells. Second, waves at frequencies below (above) the local f_{LHR} have longer (shorter) lifetimes with larger (smaller) resultant cavity enhancement factors and propagate to higher (lower) L -shells. Finally, rays with an initial wave normal angle that is nearly perpendicular to the ambient magnetic field have much longer lifetimes and stay closer to the source location than less oblique initial wave normal angles. To maximally target the source L -shell, the optimum condition would be to use a source, situated at the equator of the desired L -shell, injecting waves at a frequency equal to the local f_{LHR} at wave normals very close to the resonance cone. Rays with an initial wave normal closer to parallel to the magnetic field, on the other hand, would disperse to more distant locations over a broader region of L -shells, albeit with a shorter lifetime and smaller resultant cavity enhancement factors.

We can quantify the role of the initial wave normal and frequency by studying the dispersal of wave power from a single L -shell for a wide range of input parameters. Consider two sources at $L=2$, one at the equator and another at $\lambda=20^\circ$ on the same field line. Given these two locations, we wish to identify the frequencies and injection wave normal angles that lead to maximum cavity enhancement factors in a given L -shell range, $1.8 \leq L \leq 2.2$. Based on the above discussion, we expect that, for a source at $L=2$, the $L=2.0$ shell is best targeted with 2.5 kHz waves injected with initial wave normal angles close to the resonance cone. On the other hand, the $L=1.8$ shell would best be targeted with waves ~ 4 kHz and the $L=2.2$ shell with ~ 2 kHz waves. Figure 3.11 shows the equatorial cavity enhancement factor at a range of L -shells as a function of wave frequency and initial normal. The left (right) column represents the results of equatorial ($\lambda=20^\circ$) injections, and corresponding pixels in the individual panels refer to a single injection point. For example, consider a 5 kHz ray injected at $L=2$ at the equator at a wave normal of -85° (the corresponding point is highlighted with asterisks on the left column in Figure 3.11). This wave primarily moves inwards and with resultant cavity enhancement at lower L -shells. Thus the $L=2.2$ shell is not significantly illuminated if a wave with these input parameters is injected from the geomagnetic equator at $L=2$. The injection of the same wave from $\lambda=20^\circ$, however, does result in minimal cavity enhancement at $L=2.2$. For clarity, the ray path and

cavity enhancement factor for this individual injection parameters are shown.

As expected, the cavity enhancement factors at lower L -shells are smaller than those at higher L -shells. The fundamental reason for this difference lies in the fact that the higher frequency waves which tend to move inwards are also the waves that will be damped the strongest because the refractive index surface is open and unbounded for much of the raypath (see above and *Bortnik et al.* [2003a]). Additionally, the appearance of a resonance cone in the refractive index surface at frequencies above the local f_{LHR} narrows the region in wave normal space available for propagating waves. The resonance cone can be seen as the sloping region of blue in the lower right hand corner of each panel in Figure 3.11. As the frequency increases, propagating wave solutions are possible over an increasingly narrow range of wave normal angles. For these high frequencies, the most oblique wave normal angles will not propagate. The resonance cone becomes a factor at higher frequencies for off-equatorial injections (right column) since the local LHR frequency is higher at points off the equator. As such, a 4 kHz wave injected from $L=2$ at the equator is above the local f_{LHR} whereas a similar frequency wave would be below the local f_{LHR} at a latitude of 20° . These facts slightly modify the appropriate frequencies and wave normal angles needed to illuminate target L -shells. Referring to the middle panel in the first and second column of Figure 3.11, it can be seen that, for a source located at $L=2$ targeting power on $L=2$, one would use ~ 2.5 kHz waves for injections at the equator. For injections from a geomagnetic latitude of 20° , on the other hand, ~ 3 kHz waves should be used. The final point we should highlight here is that, although the resolution may not be high enough to clearly discern the difference, off-equatorial injections (displayed in the right column of 3.11) indeed result in lower cavity enhancement factors than equatorial injections. On the other hand, if we had displayed additional L -shells, we would see that these rays also propagate over a wider range of L -shells than similar rays injected at the equator. This tradeoff—higher cavity enhancement factors versus broader projection of power—can be leveraged effectively in designing a practical system aimed at controlled precipitation of energetic radiation belt electrons.

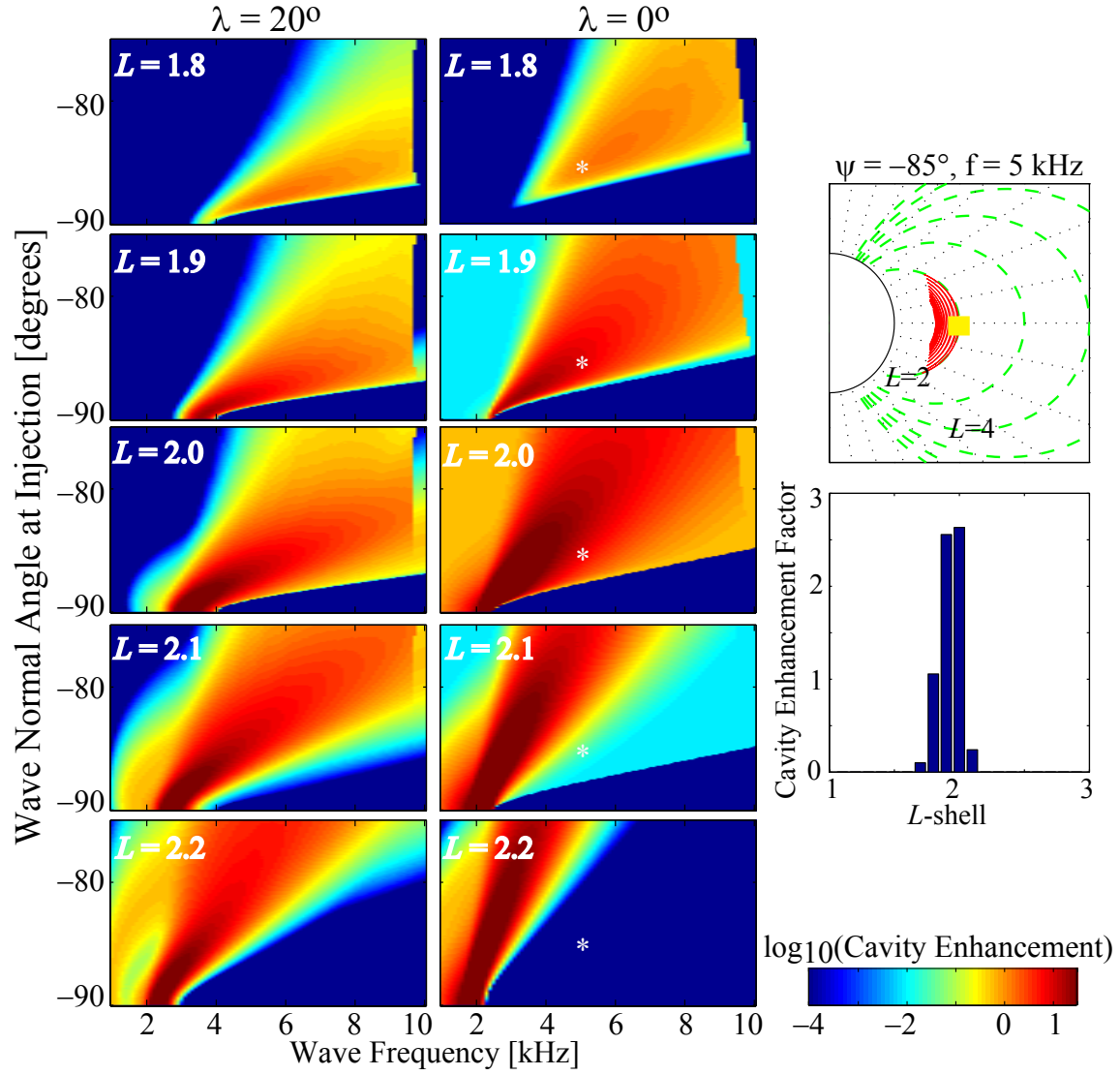


Figure 3.11: Cavity enhancement factor at $1.8 \leq L \leq 2.2$ for waves injected from $L=2$ with the injection latitude shown at the top of each column. The asterisk in each panel in the left column represents the cavity enhancement caused by a 5 kHz wave injected at the equator at a wave normal angle of -85° .

3.5 Effects of Antenna Radiation Efficiency

Our discussions thus far indicate that whistler-mode wave energy injected from a space-based source from a given position can be efficiently (i.e., with relatively large cavity enhancement factors) directed to a L -shell region as far away as $\sim 0.3L$ from the source for locations closer to the Earth and up to $\sim 1L$ for locations farther from the Earth. In formulating these results, we did not consider the restrictions that would inevitably be present as a result of the dramatically different radiation properties of practical antennas immersed in a magnetosplasma. We now investigate the effects of practical antenna efficiency and radiation pattern on our results using the model presented by *Wang and Bell* [1970] of a short electric dipole transmitting antenna immersed in a cold, magnetized plasma.

As described in Chapter 2, we assume antenna lengths of ~ 100 – 500 meters and restrict the operating frequency and initial ψ . A source located at the equator at $L=2$ would not effectively radiate VLF waves below ~ 2.3 kHz—which clearly indicates that our results presented above for 1 kHz waves should be properly qualified. Moreover, waves must have a wave normal angle within a few degrees of the resonance cone (or within a few degrees of $\psi=90^\circ$ if $f < f_{\text{LHR}}$) in order to satisfy the requirement for the radiated wavelength to be approximately equal to the antenna length.

The above restrictions limit the allowable wave frequencies and the range of wave normal angles that can be used to direct the dispersal of whistler-mode wave energy. While in Figures 3.7, 3.8 and 3.10 we integrated and normalized over wave normal angles up to -75° , the *Wang and Bell* [1970] theory suggests that there would be negligible radiated power beyond $\sim \pm 85^\circ$. We thus expect that antenna radiation efficiency considerations, which limit effective radiation to only the most oblique wave normal angles, would then limit the L -shell range of illumination. To be consistent with the *Wang and Bell* [1970] model, we adjust the lower integration bound to be no more than three degrees away from the maximum wave normal angle considered (-89.9° if $f < f_{\text{LHR}}$ or ψ_{res} if $f > f_{\text{LHR}}$). Furthermore, we choose wave frequencies that are no lower than 90% of the local f_{LHR} .

This result of the inclusion of antenna radiation considerations is illustrated in

Local Lower Hybrid Resonance Frequency				
$\lambda_s = 0^\circ$			$\lambda_s = 20^\circ$	
$L = 1.5$	5.4 kHz		9 kHz	-89.3°
	6 kHz	-89.3°	10 kHz	-89°
	7 kHz	-88.9°	11 kHz	-88.8°
$L = 2.0$	2.3 kHz		3.8 kHz	
	2.5 kHz	-89.9°	4.2 kHz	-89.6°
	3.5 kHz	-88.7°	5.2 kHz	-88.9°
$L = 2.5$	1.2 kHz		2.0 kHz	
	1.3 kHz		2.2 kHz	-89.8°
	2.3 kHz	-88.1°	3.2 kHz	-88.5°

Table 3.1: The wave frequencies simulated for the six different injection sites shown in Figure 3.12. At each location, the middle frequency is approximately equal to the local f_{LHR} while the top and bottom frequencies are $\sim 10\%$ below and 1 kHz above respectively. Also shown are the resonance cone angles whenever they exist.

Figure 3.12. For each graph in Figure 3.12, we show the corresponding cavity enhancement factor for frequencies $\sim 10\%$ below, approximately equal to, and 1 kHz above the local f_{LHR} , with the frequencies chosen for each injection site given in Table 3.1. Additionally, for each wave frequency chosen, we have integrated and normalized over only the first three degrees in wave normal angle.

There are several important features of the results shown in Figure 3.12. As expected, a restricted range of initial ψ yields cavity enhancement over a smaller range of L -shells (compare to Figure 3.7). For instance, 2.5 kHz waves injected at the equator from $L=2$, shown in white in the top middle graph of Figure 3.12, lead to relatively large cavity enhancement factors in the range $1.9 < L < 2.2$, whereas including the full angular range (middle column, 2nd row in Figure 3.7) leads to large cavity enhancement factors up to $L \sim 2.4$. The requirement that the wave frequency be no more than $\sim 10\%$ below the local f_{LHR} also prevents the use of wave frequencies that would be suitable to target regions far from the injection site. This restraint is most evident for injections from $L=1.5$, as shown in the left column of Figure 3.12, where the f_{LHR} at the geomagnetic equator and at a latitude of 20° is 6 kHz and 10 kHz respectively. The top panel, comparable to Figure 3.8, shows that restricting the angular and frequency range results in cavity enhancement just in the immediate

vicinity of the transmitter location. Waves radiated from $L=1.5$ and a latitude of 20° (refer to the bottom panel in the left column) are at such a high frequency—9, 10 and 11 kHz—that no magnetospheric reflections occur. Sources this close to the Earth’s surface can therefore be used to affect energetic electrons only on the first equatorial pass of the ray path, after which the ray energy is absorbed within the ionosphere. Another noteworthy feature is that the normalized, integrated cavity enhancement factor is larger when we integrate over only the first three degrees in wave normal space. Again referring to 2.5 kHz waves injected equatorially from $L=2$, we see that cavity enhancement factor at $L=2$ is ~ 3 when the full angular range is considered (middle panel in Figure 3.7) and ~ 10 for the smaller range (shown in green in the top, middle panel in Figure 3.12). This result is a consequence of the fact that rays with an initial wave normal almost perpendicular to the ambient magnetic field have much longer lifetimes than those with lower initial wave normal angles. Hence, integrating over a much broader range of wave normal angles does not add significantly to the cavity enhancement factor, and the small gain is then completely lost upon normalization over the number of injected rays. The most persistent (i.e., the most efficiently stored) rays are still retained and available for illumination of particular L -shell regions.

For the six source sites studied here ($L=1.5, 2.0, 2.5$ and $\lambda_s=0^\circ, 20^\circ$ for each L -shell), a major overall conclusion is that only three sources, radiating power according to the *Wang and Bell* [1970] model, are required to project whistler-mode wave energy from $1.4 \leq L \leq 2.7$. The affected L -shell region displayed in Figure 3.12 in fact represents a lower-bound because we only investigated a single off-equatorial location, $\lambda_s=20^\circ$. Simulating source locations at additional geomagnetic latitudes would necessarily increase the range of L -shells upon which significant cavity enhancement factors can be attained.

We have so far determined the number of sources, locations and operating frequencies required to illuminate the inner magnetosphere with whistler-mode wave energy. We now turn to the crucial task of determining the induced energetic electron precipitation. Even if it is possible to project wave energy, controlled precipitation from

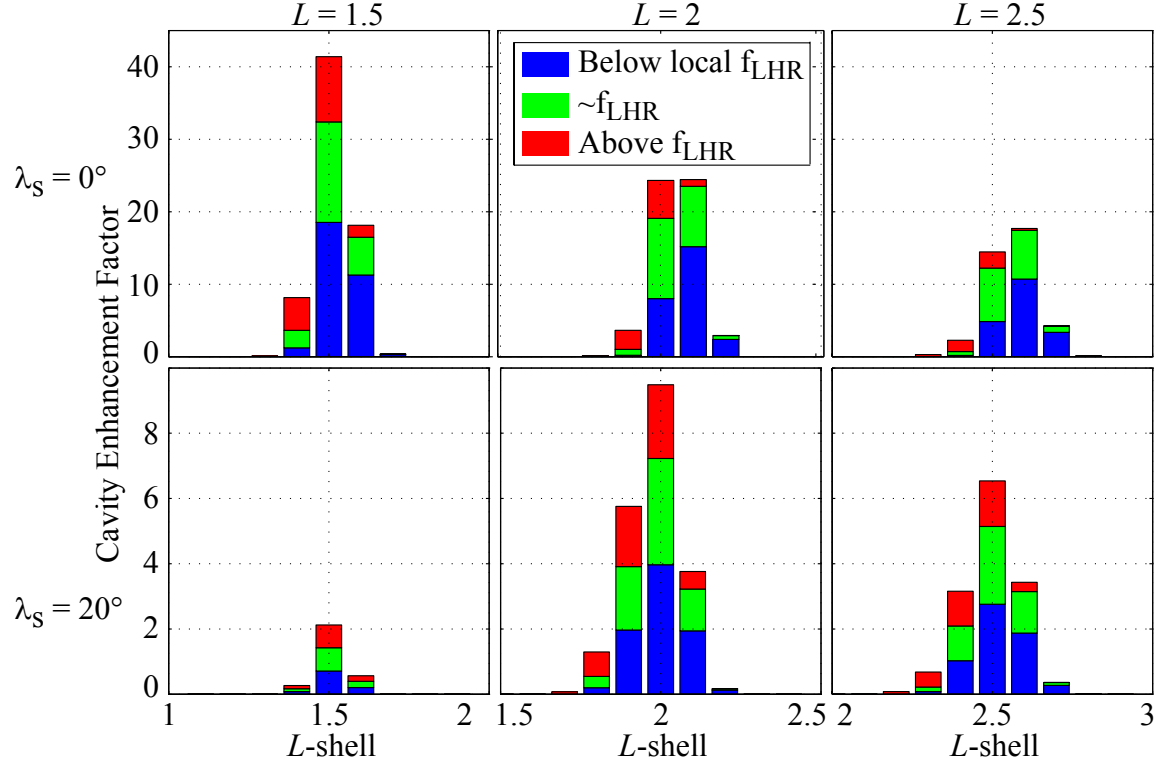


Figure 3.12: The contributing cavity enhancement factor for each frequency is given by the color code shown in the top, middle panel. Frequencies used are given in Table 3.1.

space-based sources would not be feasible if these sources do not sufficiently precipitate >100 keV and, especially, >1 MeV electrons. We are also interested in the effect on precipitation of waves that propagate with ψ very close to the resonance cone. We now address these issues in Chapter 4.

Chapter 4

Precipitation Induced by Space Based VLF Sources

4.1 Introduction

The results of both *Inan et al.* [2003] and the previous chapter lay the groundwork for determining the degree to which space-based injection is a feasible means of achieving controlled precipitation of energetic electrons. The results in *Inan et al.* [2003] highlighted the effectively larger diffusion brought about by the long lifetimes of low-frequency magnetospherically reflecting (MR) whistler-mode waves. *Inan et al.* [2003] noted that a single wave packet injected from a space-based source may endure for several seconds and can be much more efficiently stored in the magnetospheric cavity as compared to the higher wave frequencies injected from ground-based transmitters that typically make only a single traverse of the magnetosphere. It was noted, however, that the degree to which such enhanced scattering would come about depends on the efficiency of pitch angle scattering by waves propagating with wave normals at high angles near the resonance cone.

Chapter 3 identified specific locations and operating frequencies that would be most effective in precipitating >100 keV electrons. We considered both equatorial and off-equatorial source locations, and concluded that three transmitters radiating in accordance with the *Wang and Bell* [1970] antenna model are sufficient to fill the

inner magnetosphere with whistler-mode wave energy. A crucial remaining research question is the determination of the precipitation that would be induced by such space-based sources.

In this connection, it is important to note that *Inan et al.* [2003] estimated diffusion based on power scaling the results from *Abel and Thorne* [1998a,b] and duration of scattering by waves at a constant wave normal angle ψ of 45° . Magnetospherically reflecting whistler-mode waves, on the other hand, propagate obliquely with ψ near the resonance cone which for our parameters is near 90° (see below). Therefore, the diffusion estimates presented by *Inan et al.* [2003] may not be valid for waves injected from a space-based source at wave normal angles near the resonance cone, or after these waves have reflected one or more times (at which time the wave normal angle stays near the resonance cone). If high wave normal angles result in less pitch-angle scattering—a result implied by both *Inan et al.* [2003] and *Inan and Bell* [1991]—the benefit gained by multiple reflections (which enhance the duration of scattering) may be lost. This issue, which was recognized but left unresolved by *Inan et al.* [2003], is addressed in this Chapter.

We show that compared to a single-pass interaction, highly oblique magnetospherically reflecting whistler-mode waves precipitate up to 16 times more 100 keV to 5 MeV electrons. Waves injected at initial wave normal angles closer to the magnetic field, e.g., 45° , in fact precipitate fewer >1 MeV electrons than waves injected close to the resonance cone. The work presented in this chapter has been previously published in *Kulkarni et al.* [2008a], but is repeated here for completeness. We first describe the procedure used, involving the Stanford VLF Raytracing program [*Inan and Bell*, 1977] and the model described by *Bortnik et al.* [2006a].

4.2 Simulation Procedure

We launch rays representing a wave pulse of a half-second duration from the six locations specified in Chapter 3: $L=1.5$, $L=2$ and $L=2.5$ at the equator and a geomagnetic latitude of 20° for each L -shell. We primarily focus on the last two locations, however, because waves injected from $L=1.5$ induce significantly less precipitation and often

do not even magnetospherically reflect (see below and Figure 4.5.) At each source location, we select three wave frequencies as described previously: $90\%f_{\text{LHR}}$, f_{LHR} , and $f_{\text{LHR}} + 1 \text{ kHz}$. For each frequency, we then launch 30 rays separated by 0.1° in wave normal angle, starting at ψ_{res} . Table 3.1 shows the source locations, operating frequencies and, if necessary, resonance cone angles considered here. We consider a transmitter with a total radiated power of 1 W and divide this power equally among the rays, assuming that the wave \mathbf{k} -vectors are primarily directed along the resonance cone [Wang and Bell, 1972]. We then determine the latitudinal and azimuthal ($\pm 3^\circ$) spread of the rays at 1 km distance (along the ray path) from the source. This calculation results in each ray being assigned an initial Poynting flux of $1 \times 10^{-9} \text{ [W/m}^2\text{]}$. However, because we are interested in relative comparisons and dependencies of parameters, rather than the absolute amount of induced precipitation, our analyses and conclusions are insensitive to the specific value chosen here.

As the wave energy propagates along the raypath, it interacts with and precipitates energetic electrons. We use the methodology described in *Bortnik et al.* [2006a] and apply the calculated pitch-angle change to near loss-cone electrons. This procedure allows us to determine the induced precipitation that would be observed at 100 km altitude at a range of L -shells around the source [Bortnik et al., 2006b].

The AE8 distribution for trapped energetic electrons, with an assumed sinusoidal loss cone pitch-angle distribution, exhibits a sharp dropoff in flux levels with increasing energy [Vette, 1991]. While this model would yield more realistic electron precipitation signatures, its use herein obscures our evaluation of the potential efficiency of MR waves at inducing $>1 \text{ MeV}$ precipitation. The signatures that result from using the AE8 radiation belt model (Figure 4.3) show large fluxes of $<100 \text{ keV}$ electrons, and relatively weak fluxes of $>1 \text{ MeV}$ electrons. However, such results preclude us from determining if MR whistler-mode waves are ineffective at scattering $>1 \text{ MeV}$ electrons, or if weak fluxes occur simply because there are too few electrons at those energies to precipitate. We therefore assume a constant flux of $5 \times 10^4 \text{ cm}^{-2}\text{s}^{-1}\text{ster}^{-1}\text{keV}^{-1}$ for all electron energies up to 5 MeV, with a square loss cone pitch-angle distribution. The numerical value is taken to be approximately equal to

the 100 keV flux at $L=2$ in the AE8 model. Using this somewhat contrived distribution function allows us to make meaningful comparisons between >1 MeV and <1 MeV precipitation.

4.3 Relevant Physics

Before we present our simulation results, it is instructive to go into additional detail of the relevant physics of MR whistler-mode waves and the wave-particle interaction. While some of this material was presented in Chapter 2, here we reiterate the key concepts and provide deeper analysis.

4.3.1 MR Whistler-Mode Waves

As described previously, the low frequency waves considered here undergo several magnetospheric reflections along their path [Edgar, 1976]. Such waves eventually ‘settle’ on an L -shell where the wave frequency is approximately equal to the equatorial f_{LHR} . We simulate frequencies that are close to the local f_{LHR} at each source location and inject these waves at initial wave normal angles very close to ψ_{res} , which implies that the injected waves do not travel far from the source site. In fact the region of illumination is $\sim \pm 0.1L$ of the source L -shell. While the slowest variation of ω_{H} occurs around the equator and thus equatorial scattering often dominates the precipitation signature (see below and Inan *et al.* [1982]), off-equatorial wave-particle interactions can also be important.

Another important point is that MR whistler-mode waves generally propagate with wave normal angles very close to ψ_{res} [Jasna *et al.*, 1990]. One way to view the results is to examine the variation of the quantity $Y=|\psi - \psi_{\text{res}}|$, where ψ is the wave normal angle along the raypath, as is done in Figure 4 of Jasna *et al.* [1990]. Figure 4.1 shows Y along a raypath for waves injected from $L=2$ at the equator, for wave frequencies of 1, 2.5 and 4 kHz, and initial wave normal angles of $\psi=-85^\circ$, -45° , and 0° . Note that regardless of operating frequency, initial wave normal angle, or whether the frequency is below or above the local f_{LHR} , the wave normal angle ψ approaches

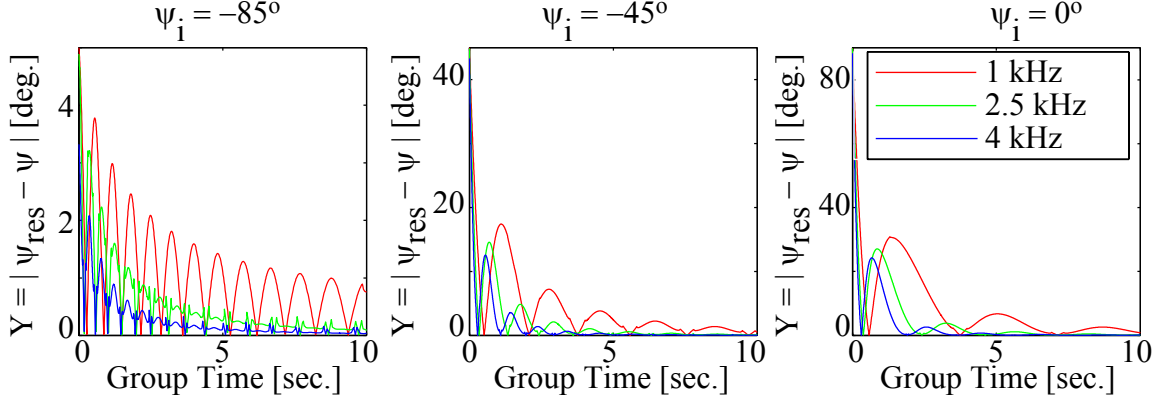


Figure 4.1: (a) - (c) $Y = |\psi - \psi_{\text{res}}|$ for three different wave frequencies and initial wave normal angles, all injected from the equator at $L=2$. The quasi-periodicity seen is a result of repeated magnetospheric reflections along the raypath. Regardless of frequency or initial wave normal angle, ψ rapidly ends up very close to the resonance cone.

the resonance cone ($Y \simeq 1^\circ$) within 10 seconds. Wave frequencies just below or above the local f_{LHR} , ~ 2.5 kHz, approach the resonance cone even more quickly.

This last point is relevant from the point of view of the feasibility of using space-based injection to precipitate energetic electrons. The results shown in the previous Chapter suggest that the restricted initial wave normal angles we have chosen, for antenna lengths of ~ 100 – 500 meters, limited the region of illumination. While this statement is true, a more important factor may be the scattering efficiency. Even if it were possible to effectively radiate at low wave normal angles of, e.g. 45° , the propagation characteristics in a cold, smooth magnetoplasma would remain the same. Within two to three magnetospheric reflections, all waves attain wave normal angles very close to the resonance cone regardless of wave frequency or initial ψ . Thus, in the cold, smooth magnetoplasma considered here, all MR whistler-mode waves quickly attain wave normal angles close to the resonance cone. These resultant high wave normal angles might negatively impact scattering efficiency, as was suggested by *Inan et al.* [2003].

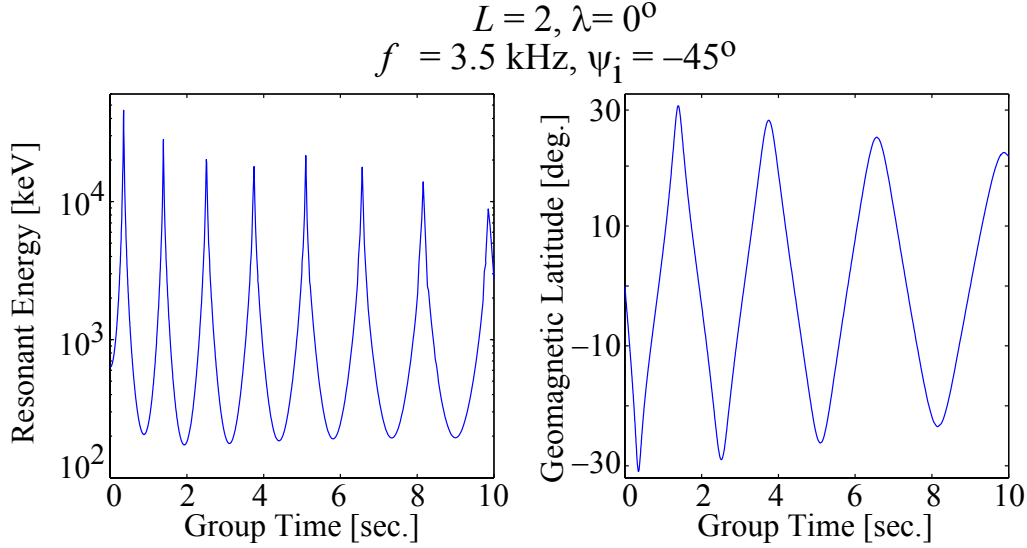


Figure 4.2: The top panel shows resonant electron energy along the raypath for the $m=1$ resonance mode for a 3.5 kHz wave injected from the equator at $L=2$. The bottom panel shows geomagnetic latitude along raypath. Note that E_{res} increases off the equator, and that the resonant energy stays above 100 keV at all points along the raypath.

4.3.2 Wave-particle Interaction

Using Equation (2.5), Figure 4.2 plots the resonant electron energy for $m=1$ along the raypath. Note that resonant energy E_{res} increases off the equator because ω_H increases away from the equator. Within the plasmopause, the 1–5 kHz waves injected from a space-based source always undergo cyclotron resonance with electrons of energies >100 keV, and often resonate with >1 MeV electrons. Note that as ψ increases, $k_z = \omega\mu \cos\psi/c$ decreases if everything else is kept constant. While $\mu=\mu(\psi)$, the decrease in the cosine factor is more important than the increase in μ near ψ_{res} unless ψ is very close ($\lesssim 1.5^\circ$) to the resonance cone, leading to a decrease in k_z . Smaller k_z in turn leads to higher parallel resonant energies as shown in Equation (2.5). Thus a wave propagating at, e.g., $\psi=45^\circ$, generally resonates with lower energy electrons than a wave propagating at $\psi=85^\circ$. These high resonant electron energies, along with long lifetimes due to magnetospheric reflections, are among the reasons that led *Inan et al.* [2003] to suggest space-based injection could be a promising means of achieving controlled precipitation of MeV electrons.

MR whistler-mode waves can resonate with and pitch-angle scatter energetic electrons at all points along the propagation path. However, the inhomogeneity of the Earth's magnetic field plays a dominant role in determining the wave-particle interaction time (or the duration of the resonant scattering). Slower variation of magnetic field amplitude, which occurs at the equator, allows the resonant wave-particle interaction to endure for a longer time (per particle) and thus often leads to the strongest precipitation [Inan *et al.*, 1982]. Also note that several terms in Equation (2.3) depends on the wave normal angle ψ between the wave \mathbf{k} -vector and \mathbf{B}_0 . The wave normal angle can thus play a crucial role in determining the precipitation signatures induced by a space-based source. Inan *et al.* [2003] noted that high wave normal angles are associated with decreased pitch-angle scattering, which might inhibit the effectiveness of an space-based source.

To summarize: MR whistler-mode waves undergo cyclotron resonance with >100 keV and >1 MeV electrons along their path. Pitch-angle scattering, however, is most effective near the magnetic equator and partially depends on the wave-normal angle ψ . The \mathbf{k} -vector of an MR whistler-mode wave stays very close to ψ_{res} during most of its raypath (regardless of the initial value emitted by the source), which results in large electron resonant velocities and which also affects pitch-angle scattering efficiency.

We should also note that in our simulations we specifically calculate precipitation induced by a one-half second long VLF pulse. In practice, VLF sources used for controlled precipitation may operate continuously, and thus may have long-term effect on the pitch-angle distribution of energetic electrons that are not revealed in our calculations. Nevertheless, a recent study by Shprits *et al.* [2006] documented that electron lifetimes are primarily governed by the value of pitch angle scattering close to the loss cone. Accordingly, it is likely that the induced precipitation of loss-cone energetic electrons as is calculated here may indeed yield useful information regarding the long-term effects of space-based VLF sources. However, in this study we only examine the effect of a short pulse on a very small range of pitch angles near the loss cone, which do not directly affect the entire distribution. If we were considering continuous precipitation then we would have to examine the complete pitch angle distribution and work toward a solution based on diffusion concepts.

We now return to the primary question raised in *Inan et al.* [2003] regarding the effectiveness of space-based injection to achieve controlled precipitation: do the benefits of high v_z and long lifetimes due to magnetospheric reflections outweigh the possible reduced pitch-angle scattering associated with wave normal angles close to ψ_{res} ? We must highlight that *Inan et al.* [2003] calculated diffusion coefficients versus wave frequency and resonance harmonic number for 1.5 MeV and 3 MeV electrons at a single equatorial location. Resonant wave frequency versus ψ was also shown at only that source location. In another study that implies large ψ leads to weak diffusion, *Albert* [1999] keeps ψ constant and calculates resonant frequencies. Such is not the case, however, for the precipitation induced by a space-based source: rather than ψ , the wave frequency is fixed, but ψ changes along the raypath and the wave undergoes both cyclotron and Landau resonance, at different points in space, with electrons from ~ 10 keV to >1 MeV. Because plasma and wave parameters, such as ω_H and μ , vary along the raypath, we should not infer the total >1 MeV precipitation induced by MR whistler-mode waves from the diffusion of 1.5 MeV electrons calculated at a single location. In fact, as our simulation results show, waves injected at ψ close to ψ_{res} can induce more >1 MeV precipitation than waves injected parallel to \mathbf{B}_0 .

4.4 Simulation Results and Analysis

We first briefly address sources located at $L=1.5$, and then proceed to analyze the results from sources at $L=2$ and $L=2.5$. We focus on the latter two source locations because waves injected from those locations induce significantly more precipitation than sources at $L=1.5$. Table 4.1 and Figure 4.5 show that waves injected from that location precipitate approximately 100 times fewer 100 keV–5 MeV electrons than the corresponding frequencies at the remaining locations. (Figure 4.5 should be compared with the results shown in Figures 4.6 and 4.7). Moreover, the 9 kHz, 10 kHz and 11 kHz waves that would be injected from a source at $L=1.5$, $\lambda=20^\circ$ do not magnetospherically reflect and therefore the cavity gain factor is exactly 1. (The total number of precipitated electrons equals the number precipitated before the first reflection). Our calculations do reveal that an equatorial source at $L=1.5$

	Frequency	Precipitated Electrons		Cavity Gain Factor	
	kHz	>100 keV	>1 MeV	>100 keV	>1 MeV
$L=1.5, \lambda=0^\circ$	5.4	0.039	0.038	211.2	216.3
	6	0.026	0.024	23.5	22.4
	7	0.073	0.072	36.7	36.2
$L=1.5, \lambda=20^\circ$	9	0.033	0.033	1	1
	10	0.043	0.043	1	1
	11	0.052	0.052	1	1
$L=2, \lambda=0^\circ$	2.3	1.57	1.57	16.1	16.1
	2.5	1.89	1.89	15.9	15.9
	3.5	2.20	2.18	10.5	10.5
$L=2, \lambda=20^\circ$	3.8	4.37	4.24	14.5	14.1
	4.2	3.47	3.32	10.7	10.2
	5.2	2.33	2.10	5.6	5.4
$L=2.5, \lambda=0^\circ$	1.2	8.96	8.91	10.8	10.7
	1.3	8.61	8.52	9.4	9.4
	2.3	5.65	4.29	4.2	5.3
$L=2.5, \lambda=20^\circ$	2.0	16.76	13.98	6.9	6.3
	2.2	14.56	11.65	6.1	5.8
	3.2	6.93	4.85	2.8	3.1

Table 4.1: The number of precipitated electrons ($\times 10^5$) and cavity gain factors for the source locations and frequencies considered here. 9 kHz, 10 kHz and 11 kHz waves injected from $L=1.5$ do not magnetospherically reflect and the cavity gain factor is exactly 1.

does produce relatively large cavity gain factors. However, this outcome is offset by overall weak precipitation. That is, even though MR waves injected by a source at $L=1.5$ precipitate many electrons after the first reflection, few total electrons are precipitated. The primary reason for relatively little induced precipitation is the extremely high electron resonant energies, from 3 MeV up to ~ 27 MeV, at locations close to the Earth's surface (see analysis and Equation (2.5) above). To precipitate >5 MeV electrons very close to the Earth's surface ($L \simeq 1.5$), 5.4 kHz, 6 kHz, and 7 kHz waves from the equator at $L=1.5$ should then be particularly effective. Except for a short discussion of magnetospheric hiss waves, the remainder of this section focuses on sources at $L=2$ and $L=2.5$.

Figure 4.3 shows differential number flux at 100 km altitude induced by an equatorial source at $L=2$. We show the energy-time signatures of precipitation that would be observed in the northern and southern hemispheres at 100 km altitude at a range of L -shells around that of the source. These results show the combined effect of including resonance modes $-5 \leq m \leq 5$, and both equatorial and off-equatorial interactions. In this figure alone, we use the AE8 radiation belt for the trapped radiation fluxes. The precipitation flux values are representative of those that would be measured in practice for a total radiated wave power of 1 Watt.

The f_{LHR} at $L=2$ at the equator is ~ 2.5 kHz. Note that 2.3 kHz waves propagate outwards to $L \simeq 2.1$, and persist for more than 20 seconds. The precipitation induced by 3.5 kHz waves, on the other hand, occurs at $L=1.9$ and the waves induce precipitation for a much shorter period of time. The quasi-periodicity seen in all the panels results from the interaction occurring primarily near the equator. Because the waves magnetospherically reflect, we observe precipitation bursts roughly with the periodicity governed by the time it takes for the wave to reach the equator. Second, note that there are large, intense precipitation peaks < 100 keV, and very weak, sometimes barely visible, precipitation bursts $\gtrsim 1$ MeV. The former peaks are the result of the Landau resonance, and the latter case is due largely to cyclotron resonance. There are many more electrons at lower energies and thus the differential number flux is more intense.

For the rest of this study, we use the constant initial electron distribution function as described above. Our goal is to quantify the amount of additional > 100 keV and > 1 MeV precipitation that occurs as a result of the MR process. To that end, we calculate the number of energetic electrons precipitated before and after the first magnetospheric reflection. To be consistent with *Inan et al.* [2003], we denote this parameter the cavity gain factor. In this study, however, the gain represents additional precipitation, not solely the number of equatorial crossings weighted by wave power density. We then compare the cavity gain factor for all the wave frequencies and source locations considered here.

Figure 4.4 shows the differential number flux, in the northern hemisphere, precipitated by a 3.5 kHz equatorial source at $L=2$. For these calculations, we use a constant

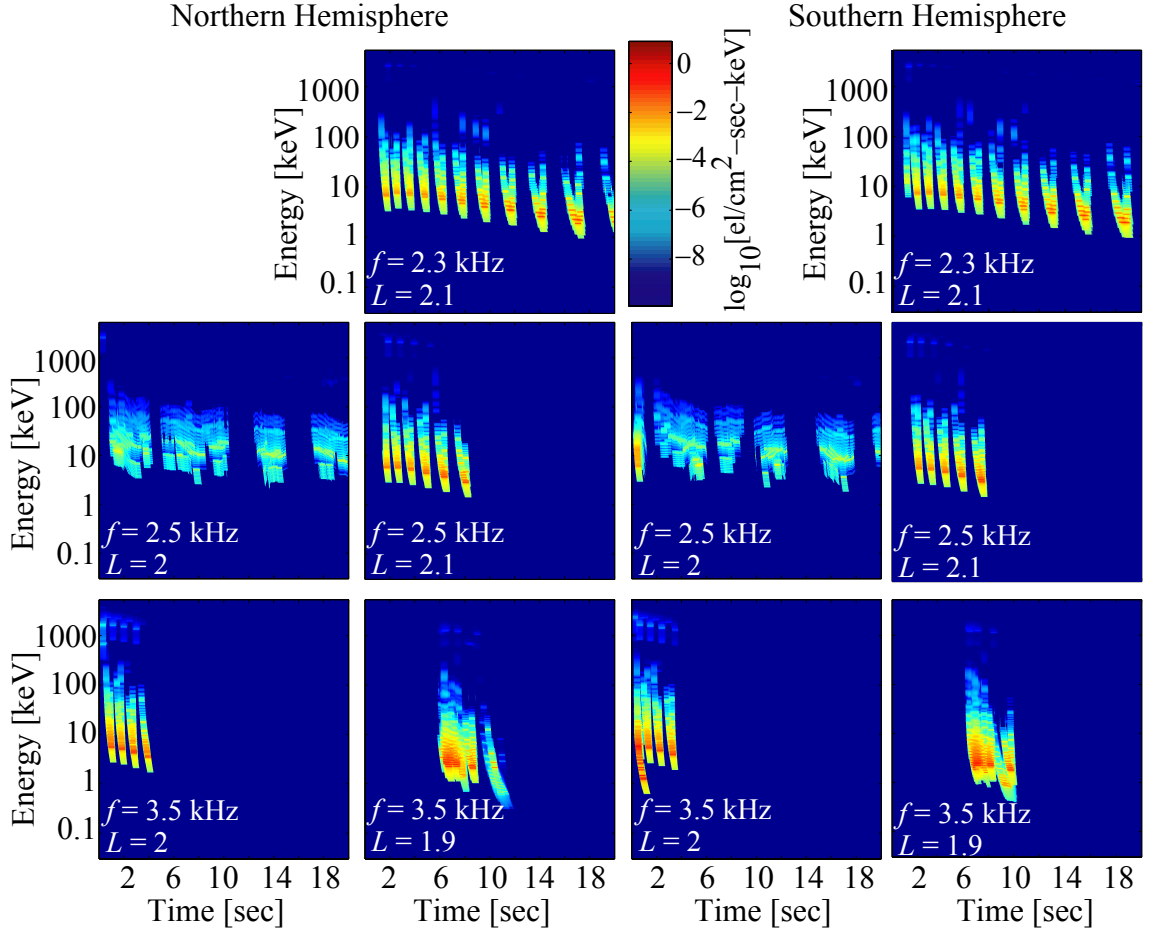


Figure 4.3: Differential number flux at 100 km altitude induced by an equatorial source at $L=2$. The left (right) two columns display the flux induced at the northern (southern) hemisphere. Shown across the rows are three different operating frequencies: 2.3 kHz, 2.5 kHz and 3.5 kHz (from top to bottom). Individual panels show where, in L -shell, precipitation occurs.

distribution function of $5 \times 10^4 \text{ cm}^{-2} \text{ s}^{-1} \text{ ster}^{-1} \text{ keV}^{-1}$ with a square loss-cone. Thus, the results greatly underestimate (overestimate) the actual <100 (>100) keV electron precipitation (see Figure 4.3 for a more realistic precipitation signature). Compared to Figure 4.3, the >1 MeV precipitation in Figure 4.4 is much stronger relative to the <1 MeV precipitation. In fact, during the first 3–4 reflections, precipitation for electrons both above and below 1 MeV is approximately equal. As the wave settles at $L=1.9$ after several reflections, the precipitation flux for >1 MeV electrons is 2–3 orders of magnitude weaker than for <1 MeV electrons. In Figure 4.3, the >1 MeV precipitation is approximately 8 orders of magnitude lower at all times. Those apparently substantially weaker signatures therefore reflect largely the AE8 distribution, which contains relatively few energetic electrons, rather than the presumed inefficient scattering induced by MR whistler-mode waves. Figure 4.4 shows that MR whistler-mode waves propagating at high wave normal angles can effectively precipitate >1 MeV electrons. Moreover, MR whistler-mode waves resonate with much higher energy electrons because large ψ increases resonant electron velocity through smaller k_z (see Chapter 2 and discussion above). Even though ψ extremely close ($\leq 0.5^\circ$) to ψ_{res} , which occurs after the first few reflections, leads to decreased scattering efficiency, the much larger resonant electron energies appear to compensate, so that >1 MeV precipitation fluxes are not lower.

Table 4.1 shows the ‘cavity gain factors’ for >100 keV and >1 MeV for all the source locations and frequencies considered here. We include the total number of precipitated electrons in both the northern and southern hemisphere. We should reiterate that these numerical results are based on a constant energetic electron distribution function. The relevant trends can be explained as follows: For each source site, except for an equatorial source at $L = 2$, higher wave frequencies induce less precipitation because of shorter lifetimes. At the equator at $L = 2$ however, 2.3 kHz and 2.5 kHz waves undergo cyclotron resonance primarily with >5 MeV. Thus the total induced precipitation is relatively low because our initial energetic electron distribution contains no electrons >5 MeV in energy. For all source locations, the cavity gain factor decreases with frequency due to, once again, shorter lifetimes, which leads to fewer magnetospheric reflections. For 3.5 kHz waves, e.g., there is relatively

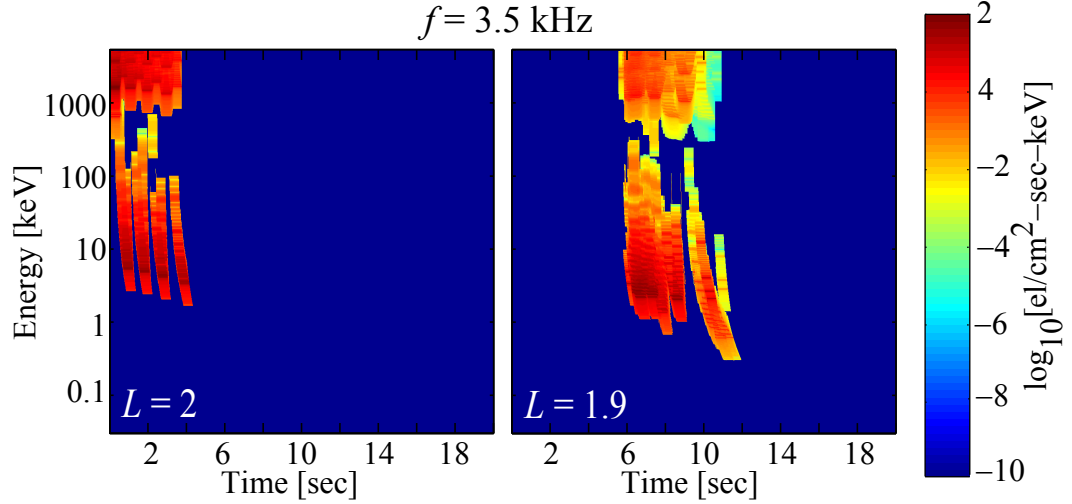


Figure 4.4: Differential number flux in the northern hemisphere at $L=2$ and $L=1.9$ induced by a 3.5 kHz equatorial source at $L=2$. These results used a constant energetic electron distribution function of $5 \times 10^4 \text{ cm}^{-2} \text{ s}^{-1} \text{ ster}^{-1} \text{ keV}^{-1}$ with a square loss-cone.

less precipitation induced after the first pass than for 2.5 kHz waves. Off-equatorial sources induce stronger precipitation because resonance energy increases at higher latitudes, and the longer raypaths therefore resonate with more energetic electrons. The decreased scattering efficiency at higher latitudes [Inan *et al.*, 1982] appears to be less important than high resonant energy. Finally, the stronger precipitation fluxes for a source located at $L=2.5$, compared to $L=2$, occur because waves injected from that source location have longer lifetimes (not shown). In all cases, waves which undergo magnetospheric reflections precipitate several times more >1 MeV electrons as compared to a single pass interaction. These results demonstrate that the MR whistler-mode waves that are injected from space-based sources may be effective at controlled precipitation of energetic electrons, and more so specifically due to their multiple reflections in the magnetospheric cavity.

Figure 4.6 and 4.7 show the precipitation and illumination spectra for the source sites and frequencies just discussed. Note that waves with frequencies below (above) the local equatorial f_{LHR} precipitate electrons primarily at L -shells higher (lower) than the source location. Also note that off-equatorial sources induce stronger >1 MeV precipitation signatures, and that higher frequencies generally induce weaker

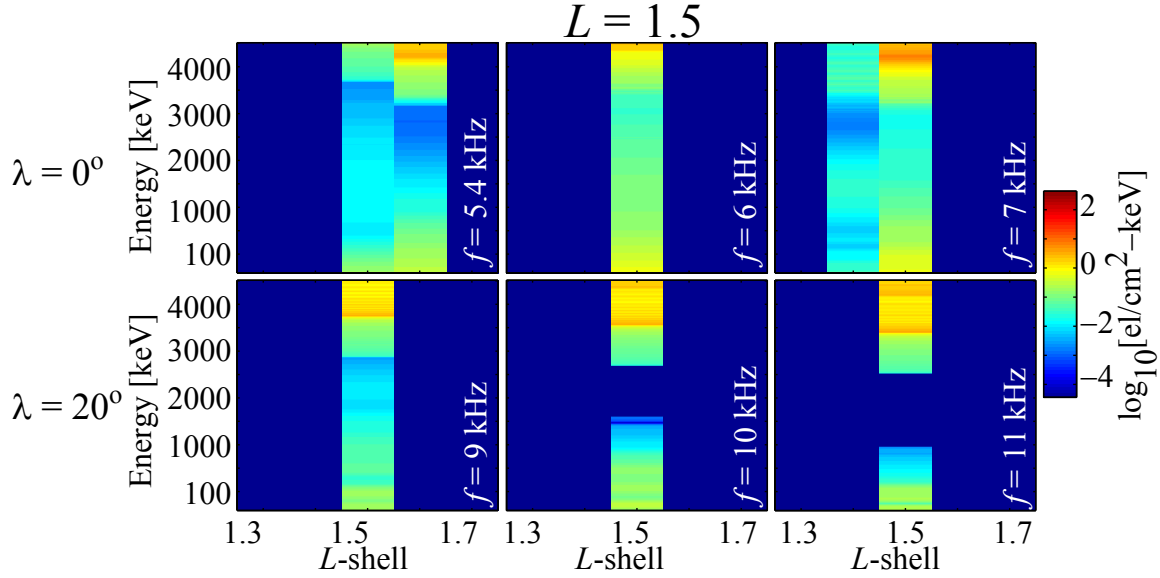


Figure 4.5: Precipitation and illumination spectra induced by sources at $L=1.5$, at the geomagnetic equator and a latitude of 20° . Note that, compared to Figure 4.6 and Figure 4.7, there is much less precipitation induced by sources at $L=1.5$.

ones. The exception for an equatorial source at $L=2$ was explained above. In this case, Figure 4.6 shows that 2.3 kHz and 2.5 kHz waves only precipitate 3–5 MeV electrons, while 3.5 kHz waves resonate with electrons energies down to 2 MeV.

The results shown thus far are all based on sources radiating waves with f close to the local f_{LHR} and injected at initial wave normal angles very close to the resonance cone. Such waves tend to remain close to the source site and settle very quickly at an L -shell. Furthermore, such waves tend to persist for 15 to 20 seconds before being Landau damped by as much as 10 dB. Waves injected with less oblique wave normal angles, on the other hand, propagate much farther from the source and have relatively short lifetimes (see Chapter 3 and *Kulkarni et al.* [2006]). Although we have restricted the initial wave normal angle, it is still instructive to compare the precipitation induced by waves with lower initial ψ with our previous calculations. These results would be useful in the event that a longer antenna can be used to effectively radiate at initial ψ far from the resonance cone.

Figure 4.8a and 4.8b shows two 3.5 kHz rays injected, at initial ψ of -88° (Ray 1) and 0° (Ray 2), from the geomagnetic equator at $L=2$. The middle panel shows

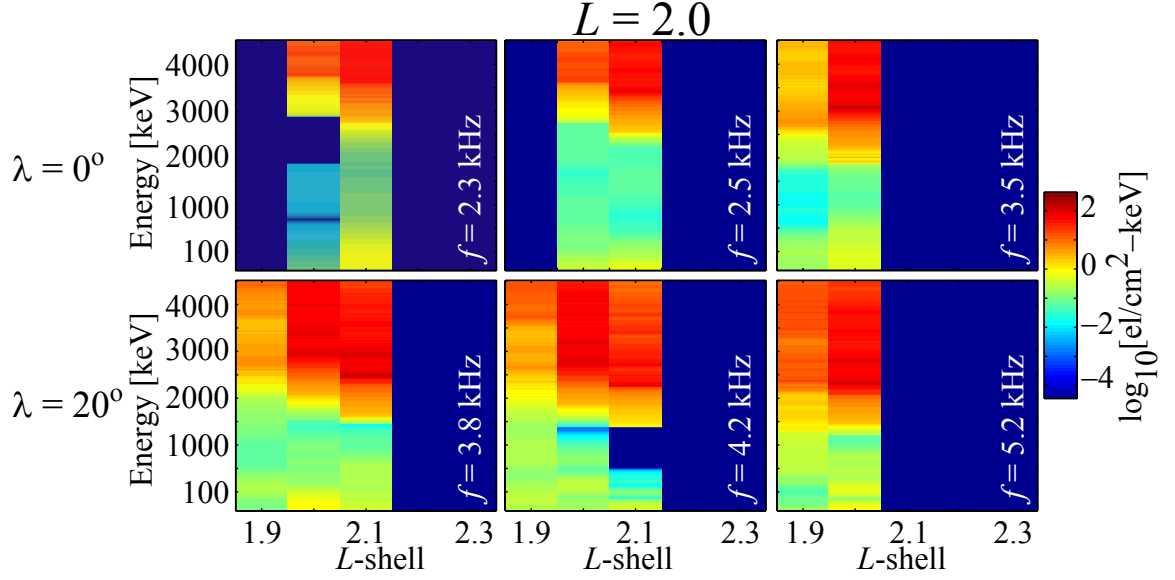


Figure 4.6: Precipitation and illumination spectra induced by sources at $L=2$. These results were obtained by integrating the differential number flux over time.

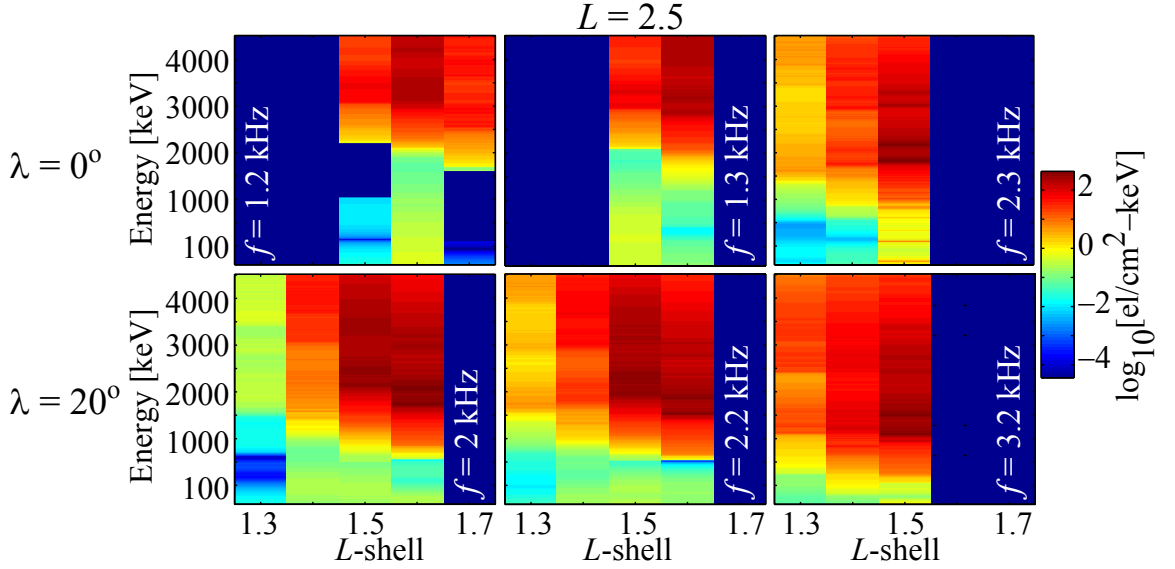


Figure 4.7: Similar to the Figure 4.6, except for a source at $L=2.5$.

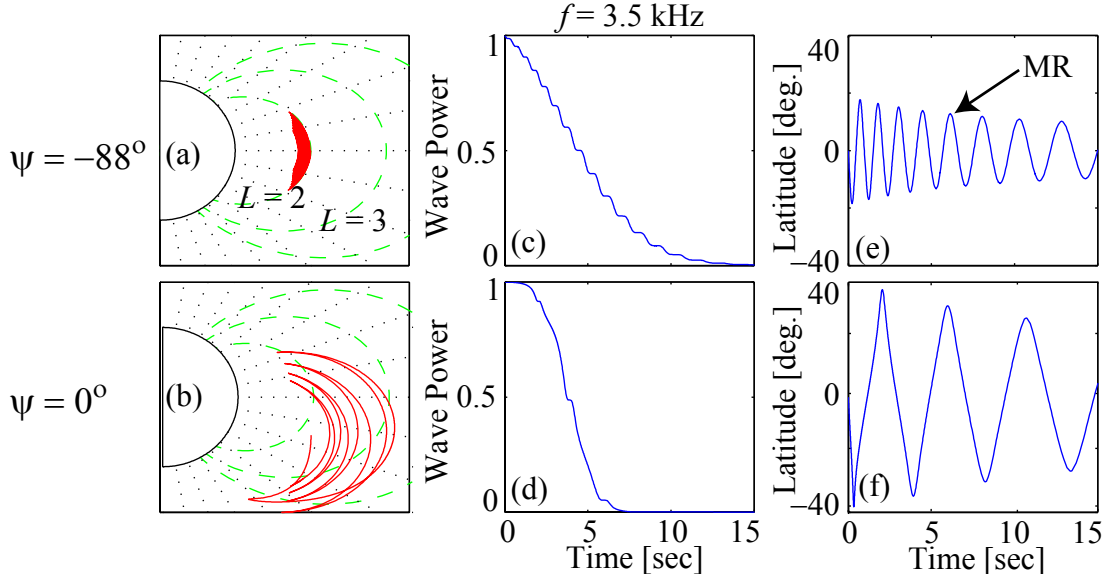


Figure 4.8: Raypaths, Landau damping and latitude along raypath for two 3.5 kHz rays injected from the equator at $L=2$. The top row displays these parameters for a ray with an initial wave normal angle of -88° , while the bottom row is for $\psi=0^\circ$.

the Landau damping along the raypath for these two rays. There are several relevant features that we must highlight. Note that Ray 1 stays very close to the source L -shell, persists for ~ 15 seconds, and magnetospherically reflects several (actually 17) times very close to the geomagnetic equator. In fact, the ray stays within $\pm 10^\circ$ of the equatorial region. Ray 2, on the other hand, propagates up to $L \simeq 3$, is Landau damped by 10 dB within 10 seconds, magnetospherically reflects only 7 times, and propagates up to a geomagnetic latitude of $\sim 30^\circ$. Shorter lifetimes and fewer magnetospheric reflections imply that waves injected at lower initial ψ precipitate fewer energetic electrons as compared to the results shown earlier. Moreover, waves injected at low initial ψ (e.g., Ray 2) propagate up to relatively high geomagnetic latitudes along the field line where pitch-angle scattering is relatively inefficient due to the more rapid gradients of the Earth's magnetic field [Inan *et al.*, 1982].

Table 4.2 compares the >100 keV and >1 MeV electron precipitation induced by a 3.5 kHz equatorial source at $L=2$. We follow an identical procedure described earlier, but consider rays centered at 0° , -25° , -45° and -65° rather than the resonance cone. For reference the last row reproduces the results shown in Table 4.1, where the

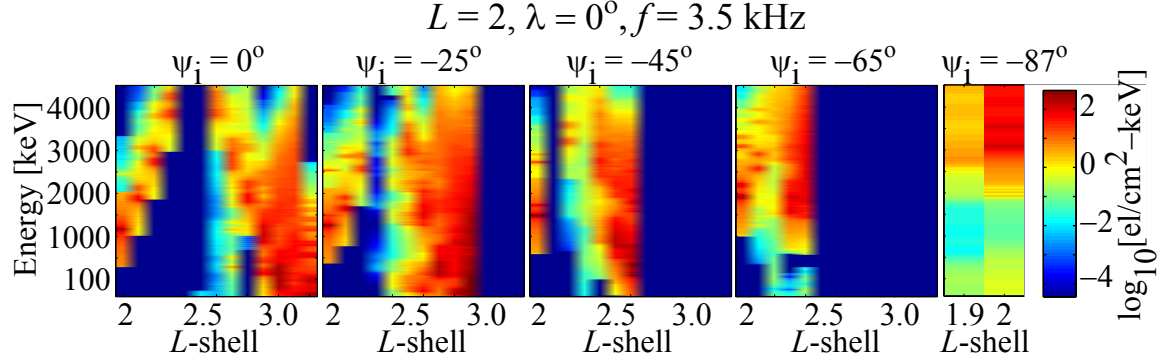


Figure 4.9: Precipitation and illumination spectra for 3.5 kHz waves injected at a range of initial wave normal angles. In all panels, the source site was at the equator at $L=2$.

rays were injected within 3° of ψ_{res} . Note that waves injected at less oblique initial wave normal angles generally precipitate fewer >1 MeV electrons. The >100 keV precipitation, however, is stronger when the initial wave normal angle is closer to \mathbf{B}_0 because the larger k_z leads to lower resonant energies than waves with ψ close to ψ_{res} . Although such waves are less effective at inducing >1 MeV electron precipitation, they do precipitate electrons at a broader range of L -shells. Figure 4.9 shows the precipitation and illumination spectra for the range of initial wave normal angles just described. Note that the precipitation is generally stronger at lower energies, and that increasing ψ leads to illumination over a narrower range of L -shells. For waves injected at $\psi \simeq 0^\circ$, the ray paths are such that certain L -shells are not illuminated with whistler-mode wave energy (see Figure 4.8b).

Our results indicate that MR whistler-mode waves injected at high initial wave normal angles may be effective at inducing >1 MeV electron precipitation in spite of the concern raised by [Inan *et al.*, 2003] due to the high values of ψ . Compared to a single-pass interaction, multiple reflections sometimes induce an order of magnitude more energetic electron precipitation. However, only locations within $\sim 0.1L$ of the source site can be effectively targeted. Projecting whistler-mode wave energy to more distant L -shells require injecting high power waves at low ($\lesssim 45^\circ$) initial wave normal angles, typically not feasible at electrical dipole antenna lengths of a few hundred

	Number of Precipitated Electrons		Cavity Gain Factor	
	>100 keV	>1 MeV	>100 keV	>1 MeV
0°	2.38	1.09	14.6	21.7
25°	3.90	1.32	32.4	80.7
45°	1.83	0.73	18.3	51.0
65°	2.94	2.06	21.4	51.4
~87°	2.20	2.18	10.5	10.5

Table 4.2: The number of precipitated electrons ($\times 10^5$) and cavity gain factors for different initial wave normal angles for a 3.5 kHz equatorial source at $L=2$.

meters. Even if such injection were possible, such waves are Landau damped relatively quickly and induce less >1 MeV precipitation. These two conclusions together imply that illuminating a broad region of the magnetosphere may require multiple sources distributed radially. Further investigation is required to determine if three-dimensional raytracing, warm plasma effects, or the existence of density irregularities might change this conclusion.

We now briefly consider magnetospheric hiss waves that induce electron precipitation at $L=2$ to $L=2.5$. Previous studies [*Lyons et al.*, 1972; *Meredith et al.*, 2007] have suggested that magnetospheric hiss plays an important role depleting energetic electrons from those L -shells. The landmark study by *Abel and Thorne* [1998a,b], however, concluded that man-made VLF transmitters are needed to account for the observed electron lifetimes below $L<2.6$. Anthropogenic sources—including possible future space-based transmitters—thus may be important in any future scheme of controlled precipitation at these L -shells. A space-based source at $L=1.5$ might also be an important driver of precipitation at low L -shells, despite the weak precipitation signatures shown in that region.

As a final note, we reiterate that because we use a 2D raytracer, we can only trace rays within the meridional plane and our results thus represent at best a lower limit on the induced precipitation. Including ray paths outside of the meridional plane—as would be possible with a three-dimensional raytracer—may change some of the conclusions presented here. *Cairo and Lefeuvre* [1986] use three-dimensional raytracing to study the propagation of ELF/VLF hiss in the magnetosphere. Their study indicates

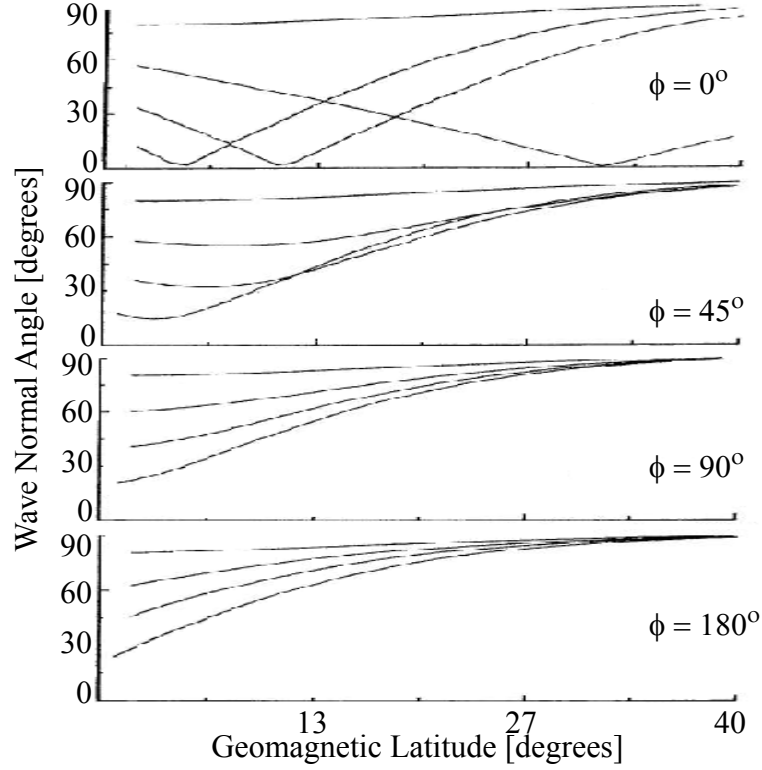


Figure 4.10: Figure 4 shown in *Cairo and Lefeuvre* [1986]. ϕ represents the geomagnetic longitude of injection.

that highly oblique whistler waves (with initial wave normal angles in the range considered in this study) tend to stay at an azimuthal angle around \mathbf{B}_0 ϕ which remains approximately constant in the course of their propagation. That is, highly-oblique waves injected outside of the meridional plane would not greatly modify the results shown here.

To further illustrate this point, we have reproduced plots from *Cairo and Lefeuvre* [1986]. In Figure 4.10 and 4.10, the geomagnetic longitude is denoted with ϕ , where $\phi=0^\circ$ and 180° lie in the meridional plane. Figure 4.10 shows that waves with initially high wave normal angles remain at those values even if the ray is injected outside of the meridional plane. In each panel in Figure 4.10, the top-most line denotes a wave injected very close to $\theta=90^\circ$. Note that as the initial ϕ is varied, θ remains highly oblique even for waves injected outside the meridional plane.

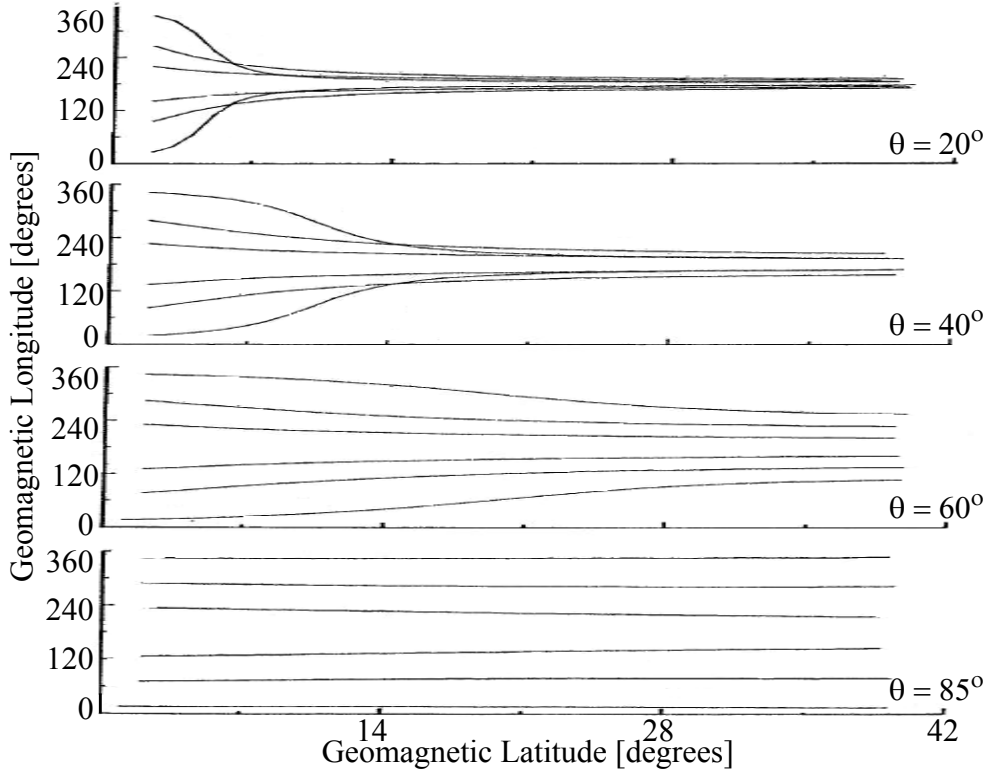


Figure 4.11: Figure 5 shown in *Cairo and Lefeuve* [1986]. As θ increases, the rays stay more confined to the injection longitude.

Figure 4.11 displays the variation in geomagnetic longitude for rays injected at different initial wave normal angles. The bottom panel of this figure most directly impacts our results. Note that as long as the initial θ is relatively large ($\gtrsim 85^\circ$), the ray will remain approximately confined to the meridian of injection. Accordingly waves injected at, for example, $\phi=120^\circ$ will not propagate over to $\phi=180^\circ$, the geomagnetic longitude of our simulation results. We are confident, therefore, that accounting for rays injected outside the meridional plane will not change the conclusions shown in this dissertation.

The results shown in Chapter 3 and 4 have answered key questions regarding the possibility of using a space-based source in a scheme of controlled precipitation of radiation belt electrons. We have shown that 3 sources distributed radially can illuminate the bulk of the inner magnetosphere with whistler-mode wave energy. We

have also shown that these sources do effectively precipitate >100 keV and >1 MeV electrons, even though the waves propagate with ψ close to ψ_{res} . We now turn our attention to the precipitation induced by ground-based VLF sources.

Chapter 5

Precipitation Induced by Ground-Based VLF Transmitters

5.1 Introduction

As described in Chapter 1, the landmark study by *Abel and Thorne* [1998a,b] calculated bounce-averaged pitch angle diffusion coefficients and concluded that ground-based VLF transmitters have a substantial effect on energetic (>100 keV) electron lifetimes at $L < 2.6$. These powerful sources operate continuously radiating signals that illuminate the Earth-ionosphere waveguide for naval communication, but the wave energy inevitably leaks into near-Earth space where the injected waves interact with and precipitate radiation belt electrons. Previous authors [*Inan et al.*, 1984; *Abel and Thorne*, 1998a,b] have attempted to quantify the energetic electron precipitation induced by ground-based VLF sources. In this chapter, we extend previous work by combining the theoretical models described earlier: numerical raytracing including Landau damping, and a calculation of precipitation induced in the resonance wave-particle interaction. We also utilize the model of antenna radiation as formulated by *Rodriguez et al.* [1994] and explained in Chapter 2.

We aim in this chapter to identify the tradeoffs among source location, operating frequency and radiated power for VLF sources designed at targeting >100 keV electrons in the inner radiation belt. We determine energetic electron precipitation

signatures induced by five existing ground-based VLF sources as well as five different hypothetical transmitters distributed broadly in geomagnetic latitude with a wide range of operating frequencies. For the existing VLF transmitters, we use geomagnetic coordinates in the centered dipole model that correspond to the source geographic latitudes. These results allow us to determine the wave frequencies and transmitter locations that most effectively precipitate >100 keV electrons. We interpret the numerically determined global signatures of transmitter induced particle precipitation in terms of the physics of VLF wave propagation (both in the Earth-ionosphere waveguide and in the magnetosphere) and the location and effectiveness of wave-particle interaction regions.

We show that source location affects induced precipitation more strongly than operating frequency or radiated power. Sources located at 35° to 45° induce the most >100 keV precipitation for the 10 to 40 kHz waves typical of ground-based VLF sources, while locations below $\lambda \simeq 15^\circ$ or above $\lambda \simeq 55^\circ$ are least effective at precipitating energetic electrons. In all cases, induced precipitation increases as the operating frequency decreases, with 10 kHz waves from a source at $\lambda \simeq 35^\circ$ being the most effective at precipitating >100 keV electrons. Precipitation signatures produced by five existing ground-based VLF transmitters are also simulated: the NAA, NLK, NAU, NPM, and NWC transmitters. NWC induces the strongest >100 keV electron precipitation signature, followed by NPM, NAU, NAA and NLK. The results below have been previously published [Kulkarni *et al.*, 2008b] but are repeated here for completeness.

5.2 Model Description and Simulation Procedure

Table 5.1 shows the properties of the five existing VLF transmitters considered in this study. To calculate the energetic (>100 keV) electron precipitation induced by VLF transmitters, we utilize four separate models: (1) antenna radiation pattern and attenuation of VLF wave energy versus distance from source for an electrically small vertical ground-based VLF antenna, (2) attenuation (mainly due to collisional absorption in the *D*-region) of VLF wave energy during propagation through the ionosphere

List of VLF Transmitters			
Transmitter	Latitude (deg)	Power (kW)	Frequency (kHz)
NAA (Cutler, Maine)	54.6 N	1000	24.0
NLK (Jim Creek, Washington)	52.9 N	192	24.8
NAU (Aguadilla, Puerto Rico)	28.6 N	100	40.75
NPM (Lualualei, Hawaii)	21.4 N	424	21.4
NWC (N. W. Cape, Australia)	31.7 S	1000	19.8

Table 5.1: Parameters of the five existing VLF transmitters considered in this study.

to the base of the magnetosphere, (3) raytracing determination of the configuration of ray paths within the magnetosphere, using magnetic field and cold-plasma density models, and accounting for Landau damping along raypaths as determined by the suprathermal particle distribution, and (4) pitch-angle scattering and precipitation of energetic electrons in resonance interactions with non-ducted VLF whistler-mode waves, with the precipitation flux levels dependent upon the efficiency of scattering but also on the assumed trapped electron distribution function near the loss-cone. While these models have been explained previously, we now apply them to the precipitation induced by ground-based VLF transmitters.

For ground-based sources, the resultant precipitation is calculated by launching rays representing a one-half second long pulse at the base of the magnetosphere, taken to be 1000 km, at points spaced 0.25° ranging from 10° to 60° in geomagnetic latitude. This latitude range captures all of the induced >100 keV precipitation that is of interest, because injections at very low ($\sim 10^\circ$) or very high ($\sim 60^\circ$) latitudes induce relatively little precipitation. We then determine the input power at 1000 km altitude, calculate the attenuation through the ionosphere and then utilize numerical raytracing through the magnetosphere, assuming quiet geomagnetic conditions. This procedure was also described in Chapter 2.

To summarize thus far, VLF wave energy radiates from a ground-based source in accordance with the formula given by Equation (2.6). We calculate Poynting flux values for rays at 100 km altitude, every 0.25° from 10° to 60° in geomagnetic

latitude. The attenuation of the wave energy due to collisional absorption during trans-ionospheric propagation (up to 1000 km) is separately accounted for, and the rays, which are traced for a one-half second pulse duration, are injected into the magnetosphere with vertical wave normal angles at 1000 km. We utilize numerical raytracing to determine raypaths through the magnetosphere and include Landau damping of the wave energy as a function of distance along the ray path. The wave energy propagating in the magnetosphere interacts with the energetic electrons in cyclotron resonance, leading to the pitch angle scattering and precipitation of the energetic electrons. To determine the total flux of precipitated particles, we initially use a square (i.e. sharp) pitch-angle distribution and model the initial (unperturbed) trapped energetic electron distribution function as in *Bortnik et al.* [2006a]:

$$f(v) = \frac{a_1}{v_m^4} - \frac{a_2}{v_m^5} + \frac{a_3}{v_m^6} \quad (5.1)$$

where f is in units of s^3cm^{-6} , v_m is $v/\sqrt{1-v^2/c^2}$, and a_1 , a_2 and a_3 are constants respectively equal to $4.9 \times 10^5\text{cm}^{-2}\text{s}^{-1}$, $8.3 \times 10^{14}\text{cm}^{-1}\text{s}^{-2}$, and $5.4 \times 10^{23}\text{s}^{-3}$. This equation is simply the relativistic extension of the distribution function specified in *Bell et al.* [2002] for the electron energies involved in Landau damping. We choose this approach to be consistent with the analysis in *Bortnik et al.* [2006a,b]. Below we also investigate the effect of considering the AE8 distribution with a sinusoidal loss-cone pitch angle distribution [*Vette*, 1991].

We now examine in greater detail the wave-particle resonance condition given earlier:

$$v_z = \frac{m\omega_H/\gamma - \omega}{k_z} \quad (5.2)$$

where v_z is the resonant electron velocity along the Earth's magnetic field, \mathbf{B}_0 , m , an integer, is the resonant mode, ω_H is the electron gyrofrequency, $\gamma = \sqrt{(1-v^2/c^2)}^{-1/2}$, ω is the wave frequency, and k_z the component of the wave \mathbf{k} -vector along \mathbf{B}_0 [*Bell*, 1984]. Because γ is a function of total electron velocity, v , Equation (2.5) is not an explicit formula for v . We therefore write $v_z = v\cos\alpha$ and solve the resulting quadratic equation to calculate resonant electron velocity for near loss cone electrons. Figure 5.1 shows the outcome of this calculation, with the explicit formula used being Equation

(2) in *Bortnik et al.* [2006b].

This equation illustrates the manner in which location of the interaction (which determines ω_H) and ω affect resonant velocity: v_z is generally inversely proportional to ω and directly proportional to ω_H . For electron energies of $\gtrsim 1$ MeV, however, relativistic effects imply that there is no such simple dependence, and our code properly accounts for the relativistic gamma factor. In Figure 5.1, we examine 20 kHz and 40 kHz rays injected at geomagnetic latitudes of 25° , 40° , and 55° , and calculate v_z along the raypath, where the short black lines on each raypath represent the direction of the \mathbf{k} -vector at selected discrete points. For a given source location, the 40 kHz ray resonates with lower energy electrons and crosses the geomagnetic equatorial plane at lower L -shells. Rays injected by any ground-based VLF source tend to cross the magnetic equatorial plane at an L -shell such that the wave frequency is less than or equal to half the electron gyrofrequency [*Inan and Bell*, 1991]. Because the gyrofrequency is larger closer to the Earth's surface, a 40 kHz ray crosses the equator at a lower L -shell compared to a 20 kHz ray. Figure 5.1 also shows that higher source latitudes lead to lower resonant energy along the raypath because the ray propagates to higher L -shells where ω_H is lower. For example, a 40 kHz ray injected from 25° resonates with more energetic electrons than a 20 kHz ray injected from both 40° and 55° .

This last result implies that source location may be more important than operating frequency in determining induced energetic electron precipitation. But although location does influence resonant velocity more than wave frequency, the resultant electron precipitation also depends on factors such as wave power flux and wave normal angle. These factors are in turn affected by gradients in ionospheric density, latitude-dependent trans-ionospheric absorption and Landau damping.

The methodology just described—calculation of pitch-angle change of near loss-cone electrons in resonance with the wave—allows us to determine the precipitation signatures that would be observed at 100 km altitude over a range of L -shells in the source hemisphere. For the existing VLF transmitters considered, we scale these results in longitude (by simply using r^{-2} dependence of wave power density) to determine precipitation zones on the Earth's surface (displayed in Figure 5.7) by using

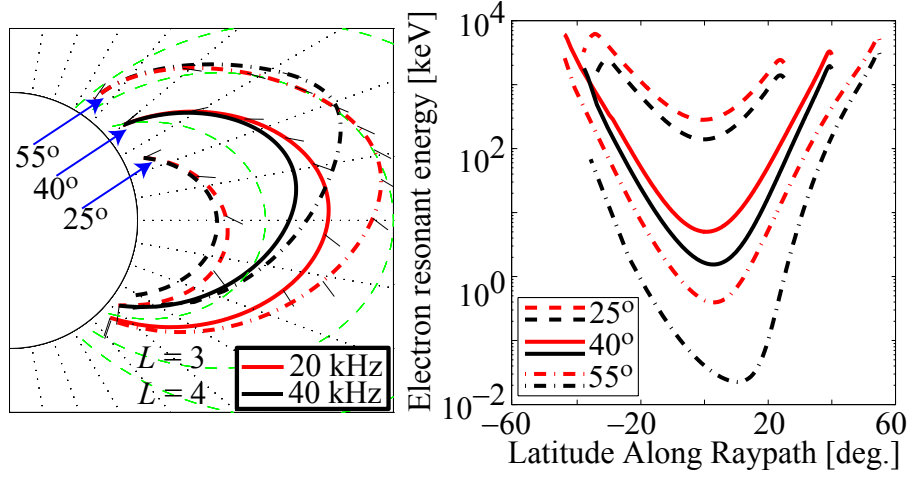


Figure 5.1: (a) 20 kHz and 40 kHz rays injected from geomagnetic latitudes of 25°, 40° and 55°. In each case, the red ray is 20 kHz, and the black ray is 40 kHz. Every 50 time steps, we have indicated the direction of the wave normal angle on three of the rays with black lines. (b) Energy of resonant electron versus geomagnetic latitude along raypath for the rays above. The legend is in the lower left.

the methodology of *Bortnik et al.* [2006b], where the precipitated flux as a function of longitude simply scales with distance from the source location [*Ibid*, Figure 6].

We focus herein on the first-order counterstreaming resonance between the wave and energetic electrons to more clearly capture and elucidate the essential physics and the dependencies on different parameters. Higher-order resonance modes are generally less efficient resonant interactions with higher energy electrons which are fewer in number. Simulation results demonstrate that including other resonant modes, m , $-5 \leq m \leq 5$ does not significantly (less than an order of magnitude) affect the calculated precipitation signatures at $L < 2.6$. Figure 5.8 compares the induced precipitation signature with including all resonance modes versus the fundamental $m=1$ mode for a source located at $\lambda=35^\circ$. Including all resonance modes results in precipitation in both the northern and southern hemispheres, which are properly calculated in our analysis. While the flux values are larger at $L \geq 2.6$, below $L=2.6$ there is very little difference between Figure 5.8a and 5.8b. This result indicates that the contributions due to higher order resonances do not significantly affect precipitation at $L < 2.6$ which is the region of maximum precipitation for 10 to 40 kHz signals and >100 keV electrons

of interest here. Below we also explore in greater detail the sensitivity of our results to the different model assumptions.

We stress that our calculated precipitation signatures result from considering wave frequencies of 10 kHz to 40 kHz and only >100 keV electrons. Wave frequencies of 3–5 kHz, e.g., undergo numerous magnetospheric reflections and would yield precipitation at substantially different L -shells. On the other hand, in our model 10–40 kHz waves make only a single traverse of the magnetosphere and do not propagate beyond $L \simeq 3$. Furthermore, focusing on electrons with energies >100 keV makes 10 kHz waves appear more effective because, as shown in Figure 5.1, 40 kHz waves often resonate with <100 keV electrons.

We now compare and contrast the energetic electron precipitation induced by hypothetical ground-based VLF sources distributed in geomagnetic latitude and operating frequency. We wish to highlight the underlying physics that leads to our numerical results, and to understand and elucidate the effects of varying transmitter location, operating frequency and radiated power. The remaining results for the actual VLF transmitters can then be explained in a straightforward manner in terms of the established dependencies.

5.3 Simulation Results and Analysis

We begin by displaying raypaths for 20 and 40 kHz waves, with all rays injected with vertical wave normal angles at the base of the magnetosphere. The raypaths shown in Figure 5.2 define the overall envelope of precipitation that would be observed at 100 km. Note that, as in Figure 5.1, 40 kHz illuminate a smaller region of the magnetosphere and cross the equatorial plane at lower L -shells. Although the raypaths shown are not different for different source locations and radiated power, the power flux and wave normal angle deposition do vary with these parameters. Figure 5.3 shows the wave power flux and wave normal angle distribution injected into the magnetosphere by 500 kW, 20 kHz sources located at 25° and 55° . While the resolution may not be high enough to discern the differences, more power is in fact injected closer to the source site, due to the latitude-dependent Helliwell absorption [Helliwell, 1965, Fig.

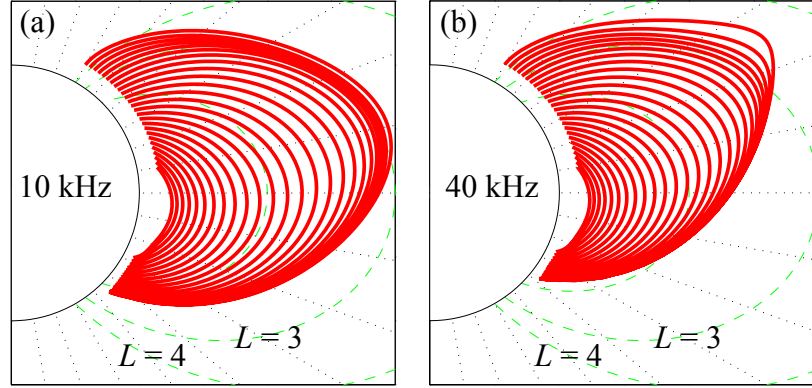


Figure 5.2: Raypaths for 20 kHz and 40 kHz sources, where rays were injected from 10° – 60° with initial vertical wave normal angles at the base of the magnetosphere. The plasmapause was located at $L=5.5$ in this figure, and for most of our simulation results.

3-35]. This absorption factor contributes to the relatively weak wave power deposited at low latitudes, as shown in the top row. Also note that, in both cases, the wave normal angle becomes highly oblique ($\sim 80^\circ$) in the southern hemisphere. The resultant >100 keV precipitation signatures depend on these parameters as well as electron resonant energy and pitch-angle scattering efficiency, all of which are accounted for in our calculations.

Because we are interested in all >100 keV precipitation, our results are shown in terms of energy flux. Energy flux combines both the number and energy spectra of the precipitated electrons. A large number of 100 keV electrons may produce a similar energy flux signature as a smaller number of 500 keV electrons. However, the distribution of energetic electrons decreases rapidly with increasing electron energy. This effect partially explains why sources at geomagnetic latitudes $\lesssim 20^\circ$ induce weak energy flux signatures despite high resonant electron energies (see below).

Figure 5.4 displays >100 keV energy flux versus L -shell induced by a one-half second pulse for sources at geomagnetic latitudes of 15, 25, 35, 45 and 55 degrees that radiate 10, 20, 30 and 40 kHz waves. We first decouple frequency and geographic location by considering these transmitters to operate at a constant radiated power of 1 MW. We vary radiated power after this initial analysis. Keeping source latitude constant, Figure 5.4 shows that induced precipitation decreases with wave frequency

for L -shells above $L \simeq 1.7$, while the opposite is true for below $L \simeq 1.7$. Furthermore, the region of illumination increases with decreasing wave frequency. In other words, 10 kHz waves illuminate geomagnetic equatorial regions ranging from $L=1.5$ up to $L \simeq 3$, while 40 kHz waves do not induce precipitation beyond $L \sim 2.3$ for any source location. At all locations, lower operating frequencies induce stronger precipitation peaks as well as total >100 keV energy flux.

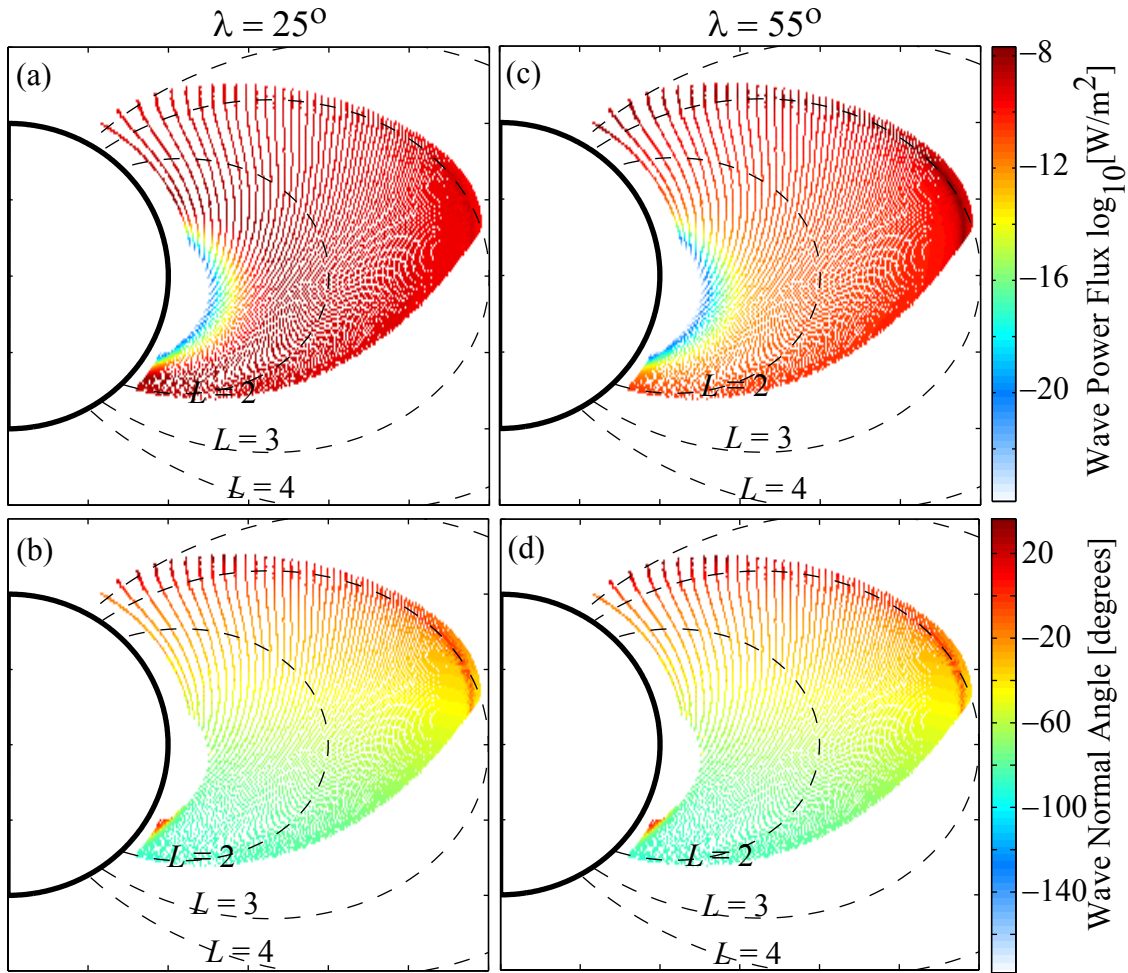


Figure 5.3: Wave power flux and wave normal angle distribution for 500 kW, 20 kHz sources at geomagnetic latitudes of 25° and 55° . These two wave properties, along with wave-particle resonance interactions, largely determine the precipitation signatures shown here.

The various dependencies exhibited can be understood in terms of the resonance

condition, disposition of raypaths through the magnetosphere, ionospheric absorption and Landau damping. According to Equation (2.5), as wave frequency increases, the resonant parallel velocity decreases if everything else is held constant. Therefore, 10 kHz waves resonate with more energetic electrons than 40 kHz waves, generally leading to stronger precipitation signatures for our chosen energetic electron distribution. For $L \lesssim 1.7$, however, 40 kHz waves are more effective than 10 kHz waves for two main reasons. First, higher wave frequencies deposit wave power flux at locations close to the Earth's surface. As seen in Figure 5.2, 40 kHz rays bend sharply toward the Earth and do not propagate beyond $L \sim 2.3$. Second, at $L \lesssim 1.7$, the high gyrofrequency leads to 10 kHz waves to be in resonance with very energetic electrons ($\gtrsim 500$ keV), the trapped flux levels of which are relatively low. Above $L \simeq 1.7$, the higher resonant electron energies combined with higher wave power flux at those locations yields stronger precipitation signatures for lower operating frequencies. In this same region, the stronger ionospheric attenuation and higher Landau damping with increasing frequency also contributes to cause 40 kHz waves to generally induce weaker precipitation fluxes than 10 kHz waves. For a given wave frequency, Figure 5.4 shows that there is an optimum source latitude from the point of view of precipitating >100 keV electrons. Sources located from 35° to 45° induce almost an order of magnitude higher >100 keV energy flux than those at $\leq 30^\circ$ or $\geq 50^\circ$.

The location-dependence of the precipitation signatures can be clarified by studying Figure 5.1 and the resonance condition (Equation (2.5)). As discussed above, rays injected from increasingly higher latitudes traverse the magnetosphere in a way such that v_z along the raypath decreases. Therefore sources at, e.g., 55° , primarily resonate with <100 keV electrons (see Figure 5.1 and related discussion). The relatively weak precipitation induced by sources at 15° and 25° is likely due to three factors. First, there are relatively fewer electrons at the very high resonant energies found at low L -shells. Second, the powerful rays injected close to the source site have very short raypaths before reaching the southern hemisphere. Finally, ionospheric absorption given by [Helliwell, 1965, Fig. 3-35] increases at low latitudes. These reasons, which result in weak >100 keV precipitation signatures from sources at low geomagnetic latitudes, plus the small v_z for sources at high latitudes, explain why mid-latitude

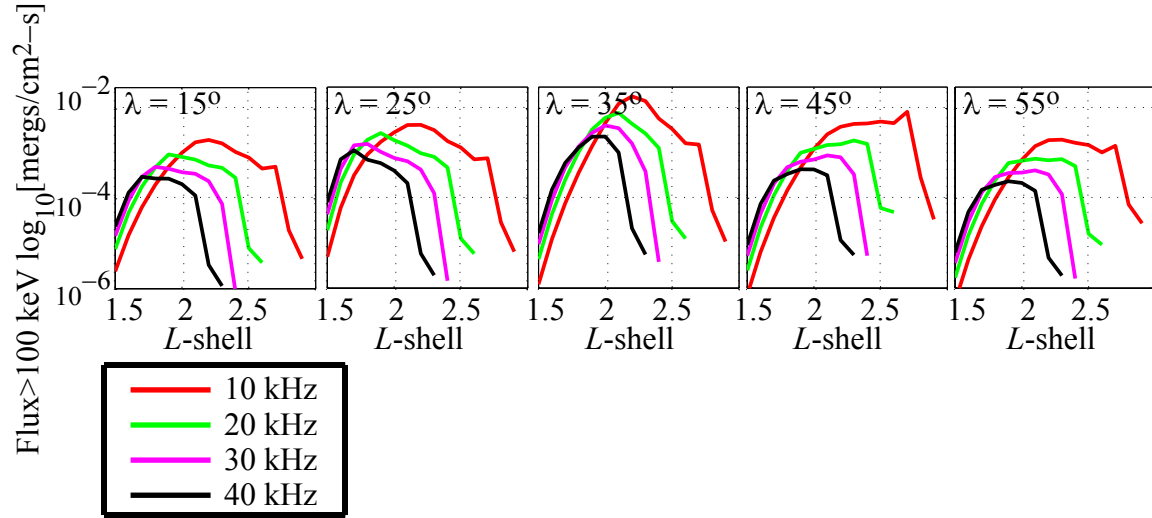


Figure 5.4: Energy flux $>100 \text{ keV}$ versus L -shell for hypothetical transmitters located at $\lambda = 15^\circ, 25^\circ, 35^\circ, 45^\circ$ and 55° , for operating frequencies of 10, 20, 30 and 40 kHz. Each transmitter radiates at 1 MW.

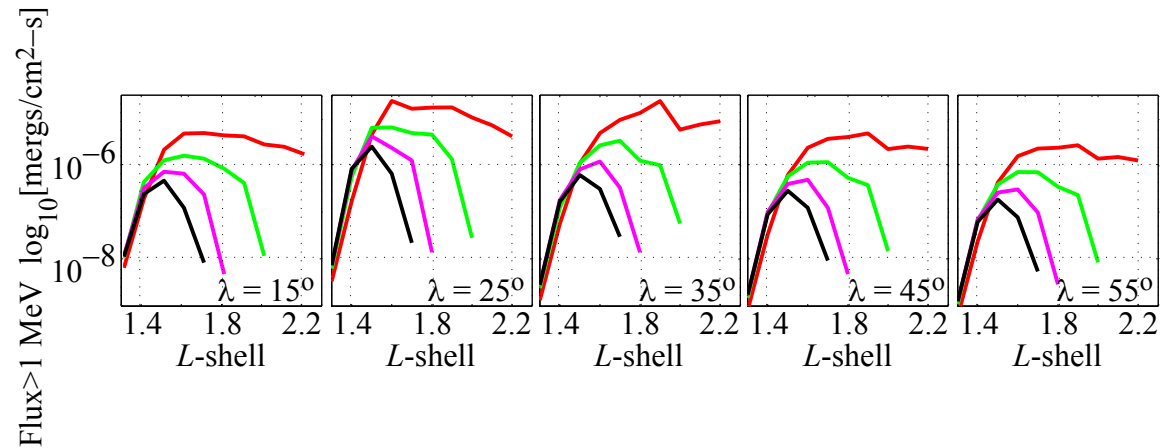


Figure 5.5: Energy flux $>1 \text{ MeV}$ versus L -shell for hypothetical transmitters located at $\lambda = 15^\circ, 25^\circ, 35^\circ, 45^\circ$ and 55° , for operating frequencies of 10, 20, 30 and 40 kHz. Each transmitter radiates at 1 MW. Legend is given in Figure 5.4 above.

source locations maximally precipitate >100 keV electrons.

The discussion above highlights that source location, more than operating frequency, impacts >100 keV electron precipitation. In fact, our results show that relatively ineffective 40 kHz waves injected from a source at 35° induces a stronger >100 keV precipitation peak than 20 kHz waves from a source at 15° , 25° or 55° .

If we consider instead >1 MeV electron precipitation, Figure 5.5 shows a similar trend, with source location once again being more important than operating frequency. In this case, however, the optimum location is from 25° to 35° latitude, as opposed to 35° to 45° for >100 keV electrons, because resonant energy near the magnetic equator is higher on L -shells closer to the Earth. Thus, the strongest >1 MeV electron precipitation signature is produced by transmitters located at lower latitudes than those that induce the strongest >100 keV energy flux. Also, the absolute energy flux levels are three to four orders of magnitude lower than in Figure 5.4 because the typical population of trapped electrons contain much fewer >1 MeV than >100 keV electrons. Finally, we note that both Figure 5.4 and 5.5 display identical trends for induced energy flux versus operating frequency.

Having investigated the importance of source location versus operating frequency at precipitating energetic electrons, we now turn to radiated power. We select a single frequency of 20 kHz, the same source latitudes used above, and radiated power levels of 100 kW, 250 kW, 500 kW, 750 kW and 1 MW. Again, we consider only the $m=1$ counterstreaming resonance, include latitude-dependent ionospheric absorption, and calculate pitch-angle scattering for resonant, loss-cone electrons. Figure 5.6 shows the results of these calculations. We first observe that sources located at 35° – 45° once again induce the strongest >100 keV energy flux for a given radiated power. Changing the power level from 100 kW to 1 MW has a much smaller effect on the precipitation signature than changing the frequency from 10 kHz to 40 kHz (see Figure 5.4). Figure 5.6 again highlights the importance of source location over other parameters, although high radiated power levels can sometimes compensate. The 2nd and 3rd panels show that a 1 MW source at 25° precipitates approximately as many electrons as a 100 kW source at 35° . A 100 kW source at 35° , however, precipitates more >100 keV electrons than a 1 MW source at either 15° or 55° .

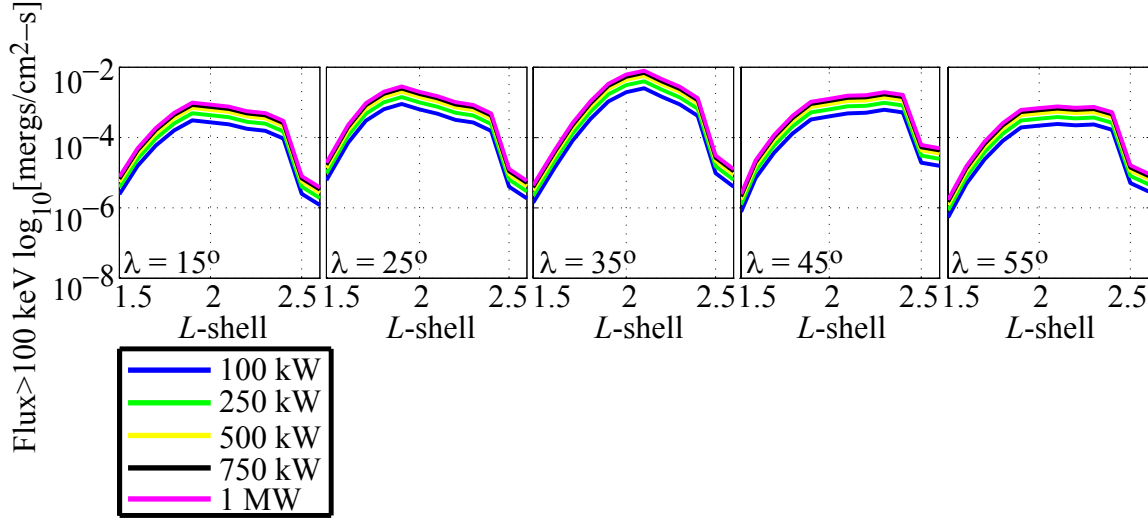


Figure 5.6: Energy flux >100 keV versus L -shell for hypothetical sources distributed in geomagnetic latitude. We select a single operating frequency of 20 kHz, and radiated power levels of 100 kW, 250 kW, 500 kW, 750 kW and 1 MW.

As mentioned at the of Chapter 3, we stress again that the results shown here are based on a two dimensional raytracing program and we therefore do not trace rays outside the meridional plane. The results shown in Figure 5.7 are based on extrapolating the results displayed earlier. Including the rays outside of the meridional plane may modify some of our results. Nevertheless, as long as wave frequencies of 10 to 40 kHz make only a single traverse of the magnetosphere, we are confident in our conclusions regarding the importance of source location.

5.3.1 Existing VLF Transmitters

Based on the above analysis, we can now quantify the effectiveness of the existing ground-based VLF sources at precipitating >100 keV electrons. Inspecting Table 5.1, we predict that NWC induces the strongest precipitation signature because of its excellent location (31.7°), the lowest operating frequency of all sources (19.8 kHz) and high radiated power of 1 MW. NLK, on the other hand, should induce the least energetic electron precipitation because it is located at a high latitude and operates with relatively low radiated power. Although it is somewhat difficult to specifically

rank the remaining three sources, we can still make some observations. NAU does not induce precipitation beyond $L \simeq 2.3$ because it operates at 40.75 kHz, the raypaths for which do not reach the equatorial plane for $L > 2.3$. NAU is at an excellent location (28.6°) for precipitating electrons, but radiates at only 100 kW. NAA has a more optimum frequency (24 kHz) and high radiated power, but is at a less optimum location, 54.6° . NPM is located at 21.4° , which is a better location than NAA. NPM also operates at a lower frequency and a relatively high radiated power of 424 kW. We predict that all three sources induce approximately equal levels of energetic electron precipitation.

In addition to energy flux versus L -shell shown above, we also present plots of the induced precipitation zones on the Earth's surface, with the signatures extrapolated in longitude as described above and in *Bortnik et al.* [2006b]. Figure 5.7 displays these results for the NAA, NLK, NAU, NPM and NWC ground-based VLF transmitters, using the characteristics listed in Table 5.1. Our predictions made above were essentially correct, although NPM does end up precipitating more >100 keV electrons than NAU. The NWC transmitter located in western Australia induces by far the strongest precipitation signature, due primarily to its optimum location (31.7°), low operating frequency and high radiated power. The NPM transmitter induces the second strongest precipitation signature because of its location, relatively low operating frequency of 21.4 kHz, and high radiated power. NAU has a slightly stronger precipitation peak than NAA because of its more favorable location, even though NAA radiates at higher power levels and at a lower frequency (24 kHz versus 40.75 kHz). NAU, however, illuminates a very narrow region of the magnetosphere (only up to $L \sim 2.2$), while NAA precipitates electrons up to $L \sim 2.4$. The NAU and NAA sources again highlight the dominant role of source location in precipitating >100 keV electrons. The NLK transmitter has very similar characteristics to NAA but operates at a lower radiated power and therefore induces the least energetic electron precipitation of all the transmitters considered.

Note, once again, that the plots in Figure 5.7 display spatial regions of >100 keV induced electron precipitation. If we consider all energies, the precipitation zones would extend farther in L -shell because resonant energy is lower at the lower

equatorial electron gyrofrequencies farther away from the Earth's surface. Finally, we should observe that the transmitters do not induce appreciable precipitation of >100 keV electrons beyond $L \sim 2.6$, consistent with the analysis from the comprehensive study by *Abel and Thorne* [1998a], which concluded that ground-based VLF sources have a significant effect on electron lifetimes at $L < 2.6$.

5.3.2 Sensitivity to Assumptions

The results presented thus far are based on a number of assumptions that, if changed, may modify our conclusions. Specifically, we have neglected higher order resonance modes, assumed a square-loss cone edge instead of a sinusoidal one, ignored ionospheric density irregularities that would randomize the initial wave normal angle, and considered a quiet-time magnetosphere with a plasmapause at $L = 5.5$. In Figure 5.8, we examine each of these assumptions in turn. We select a single operating frequency of 20 kHz and calculate >100 keV electron precipitation for sources located at 25° , 35° and 45° . All sources were operated at 1 MW of power, and except for Figure 5.8b, we considered only the $m=1$ counterstreaming resonance. For reference, panel (a) shows the results initially shown in Figure 5.4.

Figure 5.8b shows the variation of induced precipitation if several higher order resonances, from $-5 \leq m \leq 5$, are included. As the absolute value of the resonance mode increases, the electron resonance energy also increases. Furthermore, higher-order wave-particle interactions are less effective than the fundamental $m=1$ mode [*Bortnik*, 2004, p. 135]. As can be seen in Figure 5.8b, the L -shell range of the precipitation region increases up to $L \sim 3$, as opposed to $L \sim 2.6$ before including additional modes. At higher L -shells, the low gyrofrequency leads to resonance with <100 keV electrons if we only include $m=1$ (see Figure 5.1). Our results therefore do not accurately determine the absolute values of precipitation fluxes at these L -shells. However, we should highlight that total precipitation from $1.5 \leq L \leq 2.6$ is approximately the same in both cases and our approach appears to be valid in that region.

The third panel shows the effect of adopting the AE8 radiation belt model [*Vette*, 1991] with an assumed sinusoidal pitch angle distribution. For a given electron energy

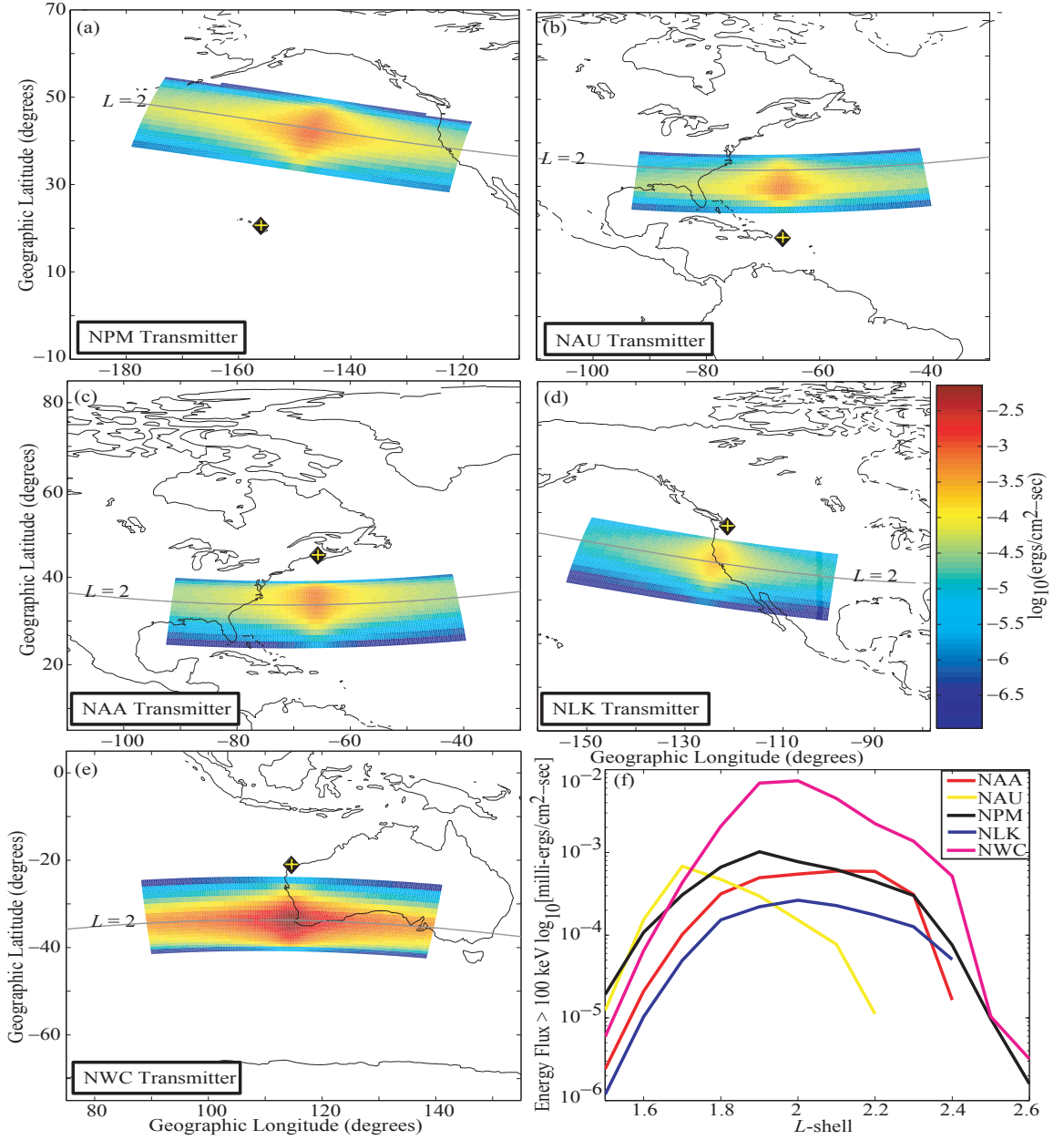


Figure 5.7: (a)-(e) Energetic electron precipitation zones on Earth for the five existing VLF transmitters considered in this study. A common color bar is shown on the right middle panel next to the NLK transmitter. (f) Energy flux >100 keV for the five existing VLF transmitters. NWC induces the strongest precipitation signature.

level >100 keV, the AE8 electron flux is about 1 to 2 orders of magnitude higher than the model we used earlier. Nevertheless, Figure 5.8c shows the AE8 radiation belt model results in a substantially weaker (2 to 4 orders of magnitude) precipitation signature at a similar L -shell range as before. This result highlights that induced electron precipitation is very sensitive to the assumed pitch-angle distribution. The precipitation signatures shown above are therefore more appropriate for disturbed geomagnetic conditions when the pitch-angle distribution may be filled with electrons at all pitch angles up to the loss cone. In this connection, however, we note that the only parameter affected by the shape of the near-loss-cone pitch-angle distribution is the absolute precipitation flux levels. All other parameter dependencies and comparisons (e.g., between transmitters at different locations) as discussed above are still valid, and relatively independent of the near-loss-cone pitch angle distribution.

The final two panels show the effect of including ionospheric density irregularities that results in randomized initial wave normal angles, and more active geomagnetic conditions with $K_{p(\text{max})}=4$ and a plasmapause at $L=3.8$ (instead of $K_{p(\text{max})}=0$ and a plasmapause at $L=5.5$). For the former case, each of the rays injected at the top of the ionosphere was assigned a random number for its initial wave normal angle, uniformly distributed between -30° and 30° about the local vertical direction. In both scenarios, the precipitation signatures are similar to that in panel (a), although a closer plasmapause results in precipitation only up to $L\sim 2.4$ (instead of $L\sim 2.6$ in (a)). Although individual raypaths and \mathbf{k} -vectors do change with these parameters, the differences are drowned out by the effect of injecting several hundred rays from 10° to 60° . The total spectrum of raypaths and \mathbf{k} -vector distribution is approximately the same in the end because the rays fill the inner magnetosphere with wave power up to $L\sim 2.5$ regardless of, e.g., initial wave normal angle of the individual rays.

We have now explained and clarified the dependence of precipitation on three key parameters—source location, operating frequency and radiated power. We have determined, for the first time, quantitative estimates for the most optimum values of these parameters by calculating the electron precipitation that would be induced by several hypothetical ground-based VLF sources distributed broadly in geomagnetic latitude and at a wide range of operating frequencies. Sources located at 35° to

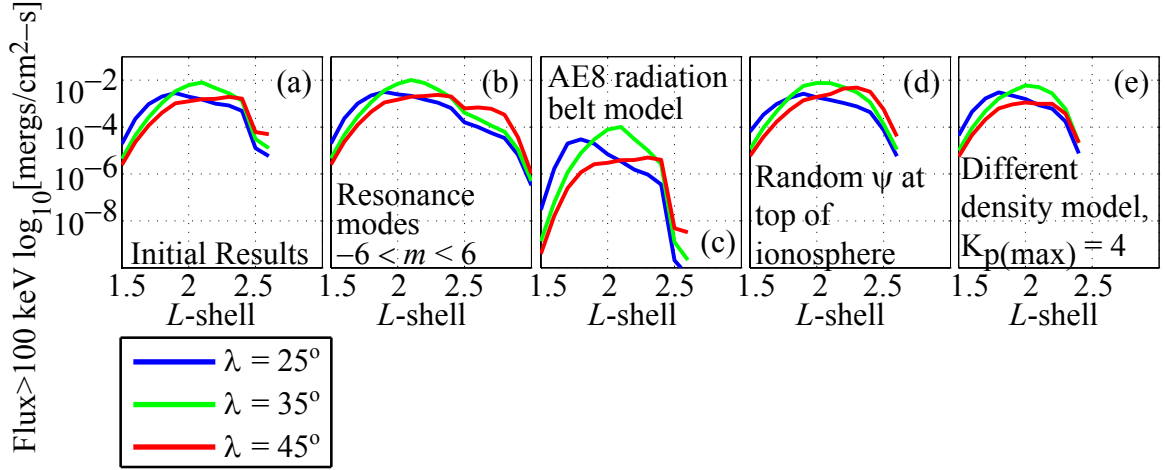


Figure 5.8: (a) A plot reproduced from Figure 5.4—a 20 kHz, 1 MW source at 25° , 35° and 45° . (b) Similar to (a), but including resonance modes $-5 \leq m \leq 5$. (c) The AE8 radiation belt model, with an assumed sinusoidal loss-cone was used to calculate the precipitation signature here. (d) Precipitation signature accounting for randomized initial wave normal angle. (e) Results for a plasmapause located at $L=3.8$.

45° induce almost an order of magnitude more >100 keV electron precipitation than sources located at 15° , 25° , or 55° . For a given location, operating frequencies of 10 to 20 kHz are more effective than 30 to 40 kHz, with 10 kHz waves producing the strongest precipitation signatures. All of our simulation results included the effects of stronger ionospheric absorption at lower latitudes and higher frequencies, and we accounted for the different wave power flux and \mathbf{k} -vector distributions that resulted from the various configurations. We also showed that, of the existing ground-based VLF sources, the NWC transmitter induces the strongest >100 keV precipitation.

Chapter 6

Summary and Suggestions for Future Work

6.1 Summary

This dissertation has quantitatively investigated the precipitation of energetic electrons in the inner Van Allen Radiation belt by waves injected from both ground-based and space-based VLF sources. Specifically, numerical raytracing, a Landau damping calculation, and a test-particle model of the wave-particle scattering efficiency were used to determine the induced precipitation.

Chapter 1 discussed the major goals of this study: (i) for ground-based VLF sources, it is necessary to determine the relative importance of source location, operating frequency and radiated power in inducing energetic electron precipitation, (ii) for space-based VLF sources, utilize realistic models of antenna radiation in a magnetosplasma to calculate the number of sources and operating frequencies needed to illuminate the inner magnetosphere with whistler-mode wave energy, (iii) model the wave-particle interaction and resultant energetic precipitation, and (iv) carefully examine the sensitivity of the induced precipitation on the direction of the wave \mathbf{k} -vector. This Chapter also introduced the near-Earth space environment and the Van Allen radiation belts, discussed the relevant past work in this field, and listed the contributions of this dissertation.

All of the simulation results presented and analyzed in this study are based on several assumptions and computational tools. In Chapter 2, the details of these underlying models were presented and explained. These include numerical raytracing with the Stanford VLF raytracing code [*Inan and Bell, 1977*], path-integrated Landau damping with the distribution function specified in *Bell et al. [2002]*, and calculation of the pitch-angle change as a result of resonant wave-particle interactions [*Bortnik et al., 2006b*]. Chapter 2 also described the models used for VLF antenna radiation for both ground-based and space-based sources, and attenuation due to collisional absorption in the D-region of the ionosphere.

Chapter 3 detailed the manner in which whistler-mode wave energy from a space based source is distributed in the inner magnetosphere. This Chapter expanded on the initial results presented in *Inan et al. [2003]* by utilizing the Stanford VLF raytracing code [*Inan and Bell, 1977*] coupled with Landau damping to determine the distribution of wave energy throughout the inner radiation belts based on injection location, wave frequency and injection wave normal angle. Both equatorial and off-equatorial injection points for wave frequencies ranging from well below to well above the local lower hybrid resonance frequency f_{LHR} and also for a broad range of injection wave normal angles were considered. After this initial analysis, the limitations that would be imposed by the *Wang and Bell [1970]* model for a short electric dipole radiating in a magnetoplasma were incorporated. These results demonstrated that a space-based source can illuminate L -shells both higher and lower than the source site by varying the frequency of the injected waves, with wave frequencies below (above) the local lower hybrid resonance, f_{LHR} , moving to higher (lower) L -shells. Only three sources placed at various locations in the inner magnetosphere are required to illuminate the region $1.4 \leq L \leq 2.7$, which comprises the bulk of the inner radiation belt.

Given that it is possible to project whistler-mode wave energy throughout the inner magnetosphere, Chapter 4 dealt with the induced electron precipitation. In this Chapter, we demonstrated that, compared to a single-pass interaction, highly oblique magnetospherically reflecting whistler-mode waves precipitate up to 16 times more 100 keV to 5 MeV electrons. An especially interesting result in this Chapter

concerns the effectiveness of the wave-particle interaction for waves propagating with wave normal angles ψ very close to the local resonance cone angle ψ_{res} . Previous work [*Inan and Bell*, 1991; *Albert*, 1999] has suggested that such waves, typical of what would be injected by a space-based VLF source, may not be effective at scattering energetic electrons. Chapter 4 showed that this concern is unfounded. In fact, waves injected at initial wave normal angles closer to the magnetic field, e.g. 45° , precipitate fewer >1 MeV electrons than waves injected close to the resonance cone.

Having addressed precipitation induced by space-based VLF sources in Chapters 3 and 4, in Chapter 5 we turned our attention to ground-based transmitters. These powerful sources operate continuously radiating signals that illuminate the Earth-ionosphere waveguide for naval communication, but the wave energy inevitably leaks into near-Earth space where the injected waves interact with and precipitate radiation belt electrons. This chapter extended previous work by combining the theoretical models described earlier: numerical raytracing including Landau damping, and a calculation of the precipitation resulting from the resonance wave-particle interaction. Five existing ground-based VLF sources as well as five hypothetical transmitters distributed broadly in geomagnetic latitude with a wide range of operating frequencies were considered. It was shown that source location affects induced precipitation more strongly than operating frequency or radiated power. Sources located at 35° to 45° induce the most >100 keV precipitation for the 10 to 40 kHz waves typical of ground-based VLF sources, while locations below $\lambda \simeq 15^\circ$ or above $\lambda \simeq 55^\circ$ are least effective at precipitating energetic electrons. In all cases, induced precipitation increases as the operating frequency decreases, with 10 kHz waves from a source at $\lambda \simeq 35^\circ$ the most effective at precipitating >100 keV electrons. Of the five existing ground-based transmitters simulated, NWC in Australia induces the strongest >100 keV electron precipitation signature, followed by the NPM, NAU, NAA and NLK transmitters.

6.2 Suggestions for Future Work

To fully assess the potential use of anthropogenic sources to bring about controlled precipitation, it is crucial to scrupulously examine the underlying assumptions and

simplifications used in this dissertation. For both ground-based and space-based VLF sources, the modification of certain initial assumptions may alter the conclusions presented here. Future research should focus on these aspects of the problem. We discuss these issues now.

6.2.1 Ionospheric Absorption

For ground-based VLF transmitters, it was assumed that from the base of the ionosphere upward, the wave energy propagates vertically through the ionosphere to the base of the magnetosphere (i.e., from 100 to 1000 km), and that it is attenuated according to a night-time absorption factor taken from [Helliwell, 1965, Fig. 3-35]. The first assumption was clearly studied in Chapter 5. Figure 5.8 show that even if vertical propagation is not assumed, the conclusions do not appreciably change. That is, source location is still relatively more important than operating frequency at inducing energetic electron precipitation.

However, the night-time absorption factor was not examined in great detail. As shown in [Helliwell, 1965, Fig. 3-29], the collisional losses are strongly dependent on the particular ionospheric profile in effect at the time. As described in Chapter 2, for our purpose we needed to account for the absorption losses in a generic manner to capture its magnitude in an average sense but more importantly its dependence on geomagnetic latitude and frequency. We thus used an interpolation of the results given in [Helliwell, 1965, Fig. 3-35], including the dependence on geomagnetic latitude. In this way, our results therefore incorporated the different absorption that would occur for different transmitter locations and operating frequencies. More specifically, our location-dependent precipitation signatures include the effects of, e.g., higher absorption at 20° versus 50° , and 20 kHz versus 10 kHz. It would be interesting to determine whether this approach correctly determines the relative absorption for these different parameter values. It may turn out that the ionospheric absorption for 20 kHz waves at 20° is not as strong as implied by [Helliwell, 1965, Fig. 3-35]. In this case, some of the conclusions regarding the optimum source locations may be modified.

We should stress, however, that the importance of source location over operating frequency and radiated power is only partially dependent upon the ionospheric absorption. The disposition of raypaths through the inner magnetosphere and the resonant electron energies along these raypaths are the more important drivers of the results presented in Chapter 5. Nevertheless, a more accurate ionospheric profile may indicate that a source at, e.g., 15° geomagnetic latitude induces stronger precipitation than the results shown in Chapter 5.

6.2.2 Warm Plasma Effects

To more accurately determine whether space-based sources can be realistically used to precipitate energetic electrons, the results of the raytracing calculation used must be studied. In this dissertation, we have exclusively assumed a cold magnetosphere. However, a finite electron and/or ion temperature may affect the propagation of wave energy, which in turn might modify the calculated precipitation signatures. Including a finite temperature in our calculations may modify the precipitation signatures shown in Chapter 4 by changing the propagation characteristics of the injected wave packets. Specifically, the magnetospheric reflection point may move to lower geomagnetic latitudes, and the wave \mathbf{k} -vector direction may be farther from the resonance cone angle. In the absence of a fully developed warm plasma raytracing program, we can make a crude estimate of the effect of temperature by calculating its effect on the refractive index.

In the raytracing methods often used in space physics, pioneered by *Haselgrove* [1954], the properties of the propagation medium enter the calculation through the refractive index, μ . Determination of μ is therefore critical to the numerical raytracing formulation. For a fixed frequency at a given location in the magnetosphere, the plasma density and various gyrofrequencies are constant, and the refractive index is often displayed as a polar plot of μ versus the wave normal angle ψ , where the polar axis is parallel to the ambient magnetic field \mathbf{B}_0 . These so-called refractive index surfaces $\mu(\psi)$ help in studying whistler mode ray propagation because the wave group velocity for a specified ψ is normal to the surface [*Helliwell*, 1965].

Incorporation of thermal effects into the refractive index surface calculation indicates that resonance cone effects are mitigated. Specifically, for frequencies above the f_{LHR} , there is no resonance cone and propagation is allowed at a greater range of wave normal angles [Hashimoto *et al.*, 1977]. This effect could potentially alter the results shown in Chapters 3 and 4.

Along these lines, it is also necessary to consider how the “smoothness” assumption affects wave propagation. Without a doubt, the magnetosphere is not entirely smooth and contains magnetic field-aligned plasma density irregularities [Bell and Ngo, 1989; Lee and Kuo, 1984]. Whistler-mode waves that interact with these irregularities can couple into lower-hybrid waves, radically changing their wave normal angle and therefore pitch-angle scattering efficiency. It is necessary to determine the occurrence rate and locations of these density irregularities, and how they will modify the raypaths and wave-particle scattering calculated in this dissertation.

Appendix A

Justification for Initial Wave-Normal Angle Restriction

The antenna factor described in *Wang and Bell* [1969] and *Kulkarni et al.* [2006] is given as:

$$F(k) = \frac{\sin^4 kl}{(kl)^4} \quad (\text{A.1})$$

As shown in (B4) of Appendix B of *Wang and Bell* [1969], the leading term of the radiation resistance for a dipole antenna in a magnetoplasma oriented along the x axis perpendicular to the ambient magnetic field is:

$$R_{\perp} \simeq 2 \ln(2/b\beta) A_o \int_0^{\infty} \frac{\sin^4(\lambda p)}{(\lambda p)^4} p^2 dp \quad (\text{A.2})$$

where b is the antenna radius, $p = n_x$, the refractive index along the x axis, and $\lambda p = hk_x/2$, where h is the antenna half length, and where:

$$A_o = Z_o (h\beta/2\pi)^2 / \sqrt{|\epsilon_s \epsilon_o|} \quad (\text{A.3})$$

If we now take the factor $(h\beta/2)^2$ from A_o and bring it into the integral, the integral can be written:

$$R_{\perp} \simeq B_o \int_0^{\infty} \frac{\sin^4 q}{q^2} dq \quad (\text{A.4})$$

where $B_o = 2\ln(2/b\beta)Z_o/(\pi^2\sqrt{|\epsilon_s\epsilon_o|})$ and $q = \lambda p$.

It can be shown that the integrand in (A.4) has maxima when $\tan q = 2q$. The dominant maximum occurs for $q = 1.17$, or equivalently, for $\lambda p \simeq 1$. Therefore the major part of the radiation resistance is contributed by waves for which $\lambda n_x \simeq 1$. To be more specific, if we let the -3 dB points define the range over which the integrand of (A.4) is significant, then we find the important values of λp to be:

$$0.6 \leq \lambda p \leq 1.8 \tag{A.5}$$

Bibliography

- Abel, B., and R. Thorne (1998a), Electron scattering loss in earth's inner magnetosphere 1. Dominant physical processes, *J. Geophys. Res.*, *103*, 2385–2396, doi:10.1029/97JA02919.
- Abel, B., and R. Thorne (1998b), Electron scattering loss in earth's inner magnetosphere 2. Sensitivity to model parameters, *J. Geophys. Res.*, *103*, 2397–2408, doi:10.1029/97JA02920.
- Albert, J. (1999), Analysis of quasi-linear diffusion coefficients, *J. Geophys. Res.*, *104*, 2429–2442, doi:10.1029/1998JA900113.
- Angerami, J., and J. Thomas (1964), Studies of planetary atmospheres, 1, The distribution of electrons and ions in the earth's exosphere, *J. Geophys. Res.*, *69*, 4537.
- Baker, D. N. (2000), The occurrence of operational anomalies in spacecraft and their relationship to space weather, *IEEE Trans. Plasma Sci.*, *28*, 2007.
- Bell, T. (1964), Time reversal of the geocyclotron mechanism, *J. Geophys. Res.*, *69*, 177–179.
- Bell, T. (1984), The nonlinear gyroresonance interaction between energetic electrons and coherent VLF waves propagating at an arbitrary angle with respect to the earth's magnetic field, *J. Geophys. Res.*, *89*, 905–918.
- Bell, T., and H. Ngo (1989), Electrostatic waves stimulated by coherent VLF signals propagating in and near the inner radiation belt, *J. Geophys. Res.*, *93*, 2599–2618.

- Bell, T., U. Inan, J. Bortnik, and J. Scudder (2002), The Landau damping of magnetospherically reflected whistlers within the plasmasphere, *Geophys. Res. Lett.*, *29*(15), 1733.
- Bittencourt, J. A. (2004), *Fundamentals of Plasma Physics*, Springer-Verlag New York.
- Bortnik, J. (2004), Precipitation of radiation belt electrons by lightning-generated magnetospherically reflecting whistler waves, Ph.D. thesis, Stanford University.
- Bortnik, J., U. Inan, and T. Bell (2003a), Energy distribution and lifetime of magnetospherically reflecting whistlers in the plasmasphere, *J. Geophys. Res.*, *108*, 1199, doi:10.1029/2002JA009316.
- Bortnik, J., U. Inan, and T. Bell (2003b), Frequency-time spectra of magnetospherically reflecting whistlers in the plasmasphere, *J. Geophys. Res.*, *108*, 1030, doi:10.1029/2002JA009387.
- Bortnik, J., U. Inan, and T. Bell (2006a), Temporal signatures of radiation belt electron precipitation induced by lightning-generated mr whistler waves: 1. Methodology, *J. Geophys. Res.*, *111*(A10), 2204, doi:10.1029/2005JA011182.
- Bortnik, J., U. Inan, and T. Bell (2006b), Temporal signatures of radiation belt electron precipitation induced by lightning-generated MR whistler waves: 2. Global signatures, *J. Geophys. Res.*, *111*(A10), 2205–, doi:10.1029/2005JA011398.
- Brinca, A. (1972), On the stability of obliquely propagating whistlers, *J. Geophys. Res.*, *77*, 3495–3507, doi:10.1029/JA077i019p03495.
- Cairo, L., and F. Lefeuvre (1986), Localization of sources of ELF/VLF hiss observed in the magnetosphere - Three-dimensional ray tracing, *J. Geophys. Res.*, *91*, 4352–4364, doi:10.1029/JA091iA04p04352.
- Carpenter, D. L. (1963), Whistler evidence of a ‘knee’ in the magnetospheric ionization density profile, *J. Geophys. Res.*, *68*, 1675.

- Carpenter, D. L., and R. R. Anderson (1992), An ISEE/whistler model of equatorial electron density in the magnetosphere, *J. Geophys. Res.*, *97*, 1097.
- Dungey, J. W. (1963), Loss of Van Allen electrons due to whistlers, *Planet. Space Sci.*, *11*, 591–595.
- Edgar, B. (1972), The structure of the magnetosphere as deduced from magnetospherically reflected whistlers, Ph.D. thesis, Stanford University.
- Edgar, B. (1976), The upper and lower frequency cutoffs of magnetospherically reflected whistlers, *J. Geophys. Res.*, *81*, 205.
- Getmantsev, C. G., N. A. Zuikov, D. S. Kotik, N. A. Mironenko, V. O. Mityakov, Y. A. Rapoport, V. Y. Sazanov, V. Y. Trakhtengerts, and V. Y. Eidman (1974), Combination frequencies in the interaction between high-power short-wave radiation and ionospheric plasma, *JETP*, *20*, 101–102.
- Gibby, A. R. (2008), Saturation effects in VLF triggered emissions, Ph.D. thesis, Stanford University.
- Gołkowski, M., U. Inan, A. Gibby, and M. Cohen (2008), Magnetospheric amplification and emission triggering by ELF/VLF waves injected by the 3.6 mw haarp ionospheric heater, *J. Geophys. Res.*, *113*, 10,201, doi:10.1029/2008JA013157.
- Gurnett, D. A., and U. S. Inan (1988), Review of plasma wave observations with the Dynamics Explorer 1 spacecraft, *Rev. Geophys.*, *26*, 285.
- Hairer, E., S. Norsett, , and G. Wanner (2000a), *Solving Ordinary Differential Equations II - Stiff and Differential-Algebraic Problems*, Springer.
- Hairer, E., S. Norsett, and G. Wanner (2000b), *Solving Ordinary Differential Equations I - Nonstiff Problems*, Springer.
- Haselgrove, J. (1954), Ray theory and a new method for ray tracing, in *Report of the Physical Society Conference on Physics of the Ionosphere*, pp. 355–364, Cambridge, England.

- Hashimoto, K., I. Kimura, and H. Kumagai (1977), Estimation of electron temperature by VLF waves propagating in directions near the resonance cone, *Planet. Space Sci.*, *25*, 871–877.
- Hecht, E. (2002), *Optics, 4th Edition*, Addison Wesley.
- Helliwell, R., and T. Bell (1960), A new mechanism for accelerating electrons in the outer ionosphere, *J. Geophys. Res.*, *65*, 1839–1842.
- Helliwell, R. A. (1965), *Whistlers and related ionospheric phenomena*, Stanford University Press.
- Helliwell, R. A., and J. P. Katsufakis (1974), VLF wave injection into the magnetosphere from Siple Station, Antarctica, *J. Geophys. Res.*, *79*, 2511.
- Inan, U., and T. Bell (1977), The plasmopause as a VLF wave guide, *J. Geophys. Res.*, *82*, 2819–2827.
- Inan, U., and T. Bell (1991), Pitch angle scattering of energetic particles by oblique whistler waves, *Geophys. Res. Lett.*, *18*, 49–52.
- Inan, U., T. Bell, and H. Chang (1982), Particle precipitation induced by short-duration VLF waves in the magnetosphere, *J. Geophys. Res.*, *87*, 6243–6264, doi:10.1029/JA087iA08p06243.
- Inan, U., H. Chang, and R. Helliwell (1984), Electron precipitation zones around major ground-based VLF signal sources, *J. Geophys. Res.*, *89*, 2891–2906.
- Inan, U., T. Bell, J. Bortnik, and J. Albert (2003), Controlled precipitation of radiation belt electrons, *J. Geophys. Res.*, *108*, 1186, doi:10.1029/2002JA009580.
- Inan, U. S. (1977), Non-linear gyroresonant interactions of energetic particles and coherent VLF waves in the magnetosphere, Ph.D. thesis, Stanford University.
- Jasna, D., U. Inan, and T. Bell (1990), Equatorial gyroresonance between electrons and magnetospherically reflected whistlers, *Geophys. Res. Lett.*, *17*, 1865–1868, doi:10.1029/GL017i011p01865.

- Kennel, C. F., and H. E. Petschek (1966), Limit on stably trapped particle fluxes, *J. Geophys. Res.*, *71*, 1.
- Kimura, I. (1966), Effect of ions on whistler-mode ray tracing, *Radio Science*, *1*(3), 263–283.
- Kulkarni, P., U. Inan, and T. Bell (2006), Whistler mode illumination of the plasmaspheric resonant cavity via in situ injection of ELF/VLF waves, *J. Geophys. Res.*, *111*(A10), 10,215, doi:10.1029/2006JA011654.
- Kulkarni, P., U. Inan, and T. Bell (2008a), Energetic electron precipitation induced by space-based VLF transmitters, *J. Geophys. Res.*, *113*(A12), 9203–+, doi:10.1029/2008JA013120.
- Kulkarni, P., U. Inan, T. Bell, and J. Bortnik (2008b), Precipitation signatures of ground-based VLF transmitters, *J. Geophys. Res.*, *113*(A12), 7214, doi:10.1029/2007JA012569.
- Landau, L. (1946), On the vibration of the electron plasma, *Soviet Journal of Physics*, *X*(1), 85–94.
- Lee, M., and S. Kuo (1984), Production of lower hybrid waves and field-aligned plasma density striations by whistlers, *J. Geophys. Res.*, *89*, 10,873–10,880, doi:10.1029/JA089iA12p10873.
- Lyons, L., R. Thorne, and C. Kennel (1972), Pitch-angle diffusion of radiation belt electrons within the plasmasphere, *J. Geophys. Res.*, *77*, 3455–3474, doi:10.1029/JA077i019p03455.
- Meredith, N., R. Horne, S. Glauert, and R. Anderson (2007), Slot region electron loss timescales due to plasmaspheric hiss and lightning-generated whistlers, *J. Geophys. Res.*, *112*(A11), 8214, doi:10.1029/2007JA012413.
- Ngo, H. D. (1989), Electrostatic waves stimulated by VLF whistler mode waves scattering from magnetic-field-aligned plasma density irregularities, Ph.D. thesis, Stanford University.

- Nickisch, L. J. (2008), Practical applications of haselgrove's equations for HF systems, *Radio Science Bulletin*, 325, 36–48.
- Ristic-Djurovic, J. L., T. F. Bell, and U. S. Inan (1998), Precipitation of radiation belt electrons by magnetospherically reflecting whistlers, *J. Geophys. Res.*, A5(103), 9249–9260.
- Rodriguez, J., U. Inan, and T. Bell (1994), Heating of the nighttime D region by very low frequency transmitters, *J. Geophys. Res.*, 99, 23,329, doi:10.1029/94JA02001.
- Rodriguez, J. V. (1994), Modification of the earth's ionosphere by very-low-frequency transmitters, Ph.D. thesis, Stanford University.
- Shklyar, D., and F. Jiříček (2000), Simulation of nonducted whistler spectrograms observed aboard the MAGION 4 and 5 satellites, *Journal of Atmospheric and Solar-Terrestrial Physics*, 62, 347–370.
- Shprits, Y., W. Li, and R. Thorne (2006), Controlling effect of the pitch angle scattering rates near the edge of the loss cone on electron lifetimes, *J. Geophys. Res.*, 111(A10), 12,206, doi:10.1029/2006JA011758.
- Smith, R. L., and J. J. Angerami (1968), Magnetospheric properties deduced from OGO 1 observations of ducted and nonducted whistlers, *J. Geophys. Res.*, 73, 1.
- Stix, T. H. (1992), *Waves in Plasmas*, Springer-Verlag New York.
- Stubbe, P. H., H. Kopka, and R. L. Dowden (1977), Generation of ELF and VLF waves by polar electrojet modulation: Experimental results, *J. Geophys. Res.*, 86, 9073–9078.
- Stubbe, P. H., H. Kopka, , M. T. Rietveld, and R. L. Dowden (1982), ELF and VLF generation by modulated heating of the current carrying ionosphere, *J. Atmos. Terr. Phys.*, 44, 1123–1135.
- Thorne, R., and R. Horne (1994), Landau damping of magnetospherically reflected whistlers, *J. Geophys. Res.*, 99, 17,249, doi:10.1029/94JA01006.

- Vette, J. (1991), The AE-8 trapped electron model environment, *NASA STI/Recon Technical Report N*, 92, 24,228.
- Walt, M. (1994), *Introduction to Geomagnetically Trapped Radiation*, Cambridge University Press.
- Wang, T., and T. Bell (1969), Radiation resistance of a short dipole immersed in a cold magnetoionic medium, *Radio Science*, 4(2), 167–177.
- Wang, T., and T. Bell (1970), On the VLF/ELF radiation resistance of an electric dipole in a cold magnetoplasma, *Radio Science*, 5, 605.
- Wang, T., and T. Bell (1972), VLF/ELF radiation patterns of arbitrarily oriented electric and magnetic dipoles in a cold lossless multicomponent magnetoplasma, *J. Geophys. Res.*, 77, 1174–1189, doi:10.1029/JA077i007p01174.